



HAL
open science

Mn-micronodules from the sediments of the Clarion-Clipperton zone (Pacific Ocean): Origin, elemental source, and Fe-Cu-Zn-isotope composition

Vesselin Dekov, Olivier Rouxel, Bleuenn Guéguen, Anna Wegorzewski, Alexis Khripounoff, Lénaïck Menot

► To cite this version:

Vesselin Dekov, Olivier Rouxel, Bleuenn Guéguen, Anna Wegorzewski, Alexis Khripounoff, et al.. Mn-micronodules from the sediments of the Clarion-Clipperton zone (Pacific Ocean): Origin, elemental source, and Fe-Cu-Zn-isotope composition. *Chemical Geology*, 2021, 580, pp.120388. 10.1016/j.chemgeo.2021.120388 . hal-03343674

HAL Id: hal-03343674

<https://hal.univ-brest.fr/hal-03343674>

Submitted on 2 Aug 2023

HAL is a multi-disciplinary open access archive for the deposit and dissemination of scientific research documents, whether they are published or not. The documents may come from teaching and research institutions in France or abroad, or from public or private research centers.

L'archive ouverte pluridisciplinaire **HAL**, est destinée au dépôt et à la diffusion de documents scientifiques de niveau recherche, publiés ou non, émanant des établissements d'enseignement et de recherche français ou étrangers, des laboratoires publics ou privés.



Distributed under a Creative Commons Attribution - NonCommercial 4.0 International License

1 Mn-micronodules from the sediments of the Clarion-Clipperton
2 zone (Pacific Ocean): Origin, elemental source, and Fe-Cu-Zn-
3 isotope composition

4
5 Vesselin M. Dekov^{a,b*}, Olivier Rouxel^b, Bleuenn Gueguen^{c,d}, Anna V.
6 Wegorzewski^e, Alexis Khripounoff^f, Lénaïck Menot^f

7
8 ^a Tokyo University of Marine Science and Technology, 4-5-7 Konan, Minato-ku, Tokyo 108-8477,
9 Japan

10 ^b Unité de Géosciences Marines, IFREMER, Z.I. Pointe du diable, BP 70 - 29280 Plouzané,
11 France

12 ^c CNRS, Univ Brest, UMR 6538 Laboratoire Géosciences Océan, F-29280 Plouzané, France

13 ^d CNRS, Univ Brest, UMS 3113, F-29280 Plouzané, France

14 ^e Federal Institute for Geoscience and Natural Resources (BGR), Stilleweg 2, D-30655
15 Hannover, Germany

16 ^f REM-EEP-LEP, IFREMER, 29280 Plouzané, France

17
18
19 A B S T R A C T

20
21 Mn- micronodules and nodules of the Clarion-Clipperton zone (Pacific Ocean) are
22 composed of 10 Å and 7 Å phylломanganates, and δ -MnO₂. The Mn-micronodules are built of
23 fine concentric growth layers of three types (1, 2a, and 2b) according to their Mn/Fe ratio and Ni,
24 Cu, and Co content. Applying previously developed geochemical discrimination approaches we
25 found that the Mn-micronodules were diagenetic precipitates that were a result of suboxic
26 diagenesis, whereas the paired Mn-nodules were diagenetic-hydrogenetic formations. The most
27 common growth layers (type 2) within the Mn-micronodules are suboxic-diagenetic, whereas the
28 rare growth layers (type 1) are mixed diagenetic-hydrogenetic and hydrogenetic precipitates. The

* Corresponding author. Tel.: +81 3-5463-0642; fax: +81 3-5463-0642; e-mail: vdekov0@kaiyodai.ac.jp

29 suboxic diagenetic formation of the Mn-micronodules seems to be a result of the fluctuation of
30 the oxic-suboxic front in the sediment since the Last Glacial Period (LGP). The migration of the
31 oxic-suboxic front close to the seawater/sediment boundary during the LGP has likely resulted in
32 suboxic reduction of Mn^{4+} and other elements in the sediment and their upward diffusion. Post-
33 LGP deepening of the oxic-suboxic front has seemingly led to re-oxidation of Mn^{2+} in the pore
34 waters and Mn-micronodule precipitation. The suboxic quantitative re-mobilization of seawater-
35 derived $Ce_{solid\ phase}$ in the sediment (positive Ce anomaly) and its subsequent sequestration by Mn-
36 micronodules resulted in positive Ce anomaly of the Mn-micronodules and Ce-deficient pore
37 water. This Ce deficiency was recorded in the diagenetic Mn-nodules (negative or no Ce
38 anomaly). The sediment pore waters were source of most elements in the Mn-micronodules and
39 to the bottom seawater.

40 The diagenetic processes were the major control on the Fe-Cu-Zn isotope composition of
41 the Mn- micronodules and nodules. Measured Fe-isotope composition of the Mn-micronodules
42 can equally be explained by hydrogenetic and diagenetic precipitation. Considering our
43 mineralogical and geochemical data we would suggest a rather diagenetic than hydrogenetic
44 control on the Fe-isotope composition of the Mn-micronodules: suboxic diagenetic reduction of
45 the sedimentary Fe in the sediment, fractionation of Fe-isotopes that produces an isotopically
46 light dissolved Fe pool, which leads to light Fe isotope composition of both the Mn-
47 micronodules and nodules (-0.63 – -0.27‰). The preferential scavenging of ^{63}Cu from seawater
48 on the hydrogenetic Mn-Fe-oxyhydroxides accounts for the Cu-isotope composition of the
49 hydrogenetic-diagenetic Mn-nodules (+0.21 – +0.35‰), which is lighter than that of seawater.
50 The identical Cu-isotope composition of the diagenetic Mn-micronodules is a result of oxidative
51 dissolution of the sedimentary Cu-containing minerals, release of isotopically heavy Cu_{aq}^{2+} in the
52 pore waters and record of this diagenetic Cu-isotope pool in the Mn-micronodules. The
53 hydrogenetic-diagenetic Mn-nodules have Zn-isotope composition (+0.75 – +0.87‰) heavier
54 than that of the seawater which is interpreted to be a result of equilibrium isotope partitioning
55 between dissolved and adsorbed Zn: preferential sorption of ^{66}Zn on Fe-Mn-oxyhydroxides
56 surfaces. Preferential adsorption of ^{66}Zn from the light Zn isotope pool of the pore waters on the
57 Mn-Fe-oxyhydroxides has resulted in heavy Zn-isotope composition of the Mn-micronodules and
58 diagenetic layers of the Mn-nodules.

59 The lack of robust assessment of the Mn-micronodule abundance in sediment volume unit
60 and the insufficient geochemical data for the Mn-micronodules prevents a meaningful estimation
61 of their resource potential.

62

63 *Keywords:* Fe-Cu-Zn-isotopes, geochemistry, Mn-micronodules, Mn-nodules, pore waters,
64 suboxic diagenesis

65

66

67 **1. Introduction**

68

69 Chester and Hughes (1967) estimated that about 85% of the manganese (Mn) in pelagic
70 sediments occurs in Mn-micronodules. Mn-micronodules are morphologically, structurally and
71 mineralogically similar to their big counterparts, Mn-nodules. Despite these similarities, there is a
72 striking discontinuity in the sizes of Mn-micronodules and Mn-nodules: the former hardly ever
73 exceed ~1 mm in diameter, whereas the later are almost always >10 mm. It was interpreted that
74 the Mn-micronodules are not proto-Mn-nodules (Heath, 1981).

75 Although the Mn-micronodules appear to be an important component in the global cycle of
76 one of the major elements on Earth, manganese, they have received far less scientific interest than
77 Mn-nodules. This has seemed to be logical in view of their economic potential estimated to be
78 lower than that of the Mn-nodules. However, with the globally increasing demand in strategic
79 elements like the rare earth elements (REE), In, Ge, W, etc. and revitalized interest in oceanic
80 metalliferous sediments (Kato et al., 2011) the economic potential of Mn-micronodules needs to
81 be revised. Although the Mn-micronodules are scattered within the upper part of the seafloor
82 sedimentary blanket, they form at much wider areas of the seafloor than the metalliferous
83 sediments and therefore, they may have greater economic value.

84 The main focus of the investigations of Mn-micronodules has been on their chemistry and
85 mineralogy (Kidd and Ármannson, 1979; Hishida and Uchio, 1981; Lallier-Verges and Clinard,
86 1983; Poppe et al., 1984; Stoffers et al., 1984; Mukhopadhyay et al., 1988; Sval'nov et al.,
87 1991a,b; Dekov et al., 2003; Ito et al., 2005; Menendez et al., 2017; Liao et al., 2019; Yasukawa
88 et al., 2019; Dubinin et al., 2020; Li et al., 2020; Xu et al., 2020; Yasukawa et al., 2020, 2021).
89 The data received was used in the interpretations of the origin of Mn-micronodules. The proposed

90 genetic models were refined with studies on the chemistry of coexisting Mn-micronodules and
91 Mn-nodules, and host sediments (Addy, 1978; 1979; Stoffers et al., 1981; Kunzendorf et al.,
92 1989; 1993; Pattan, 1993; Pattan et al., 1994; Dubinin and Sval'nov, 1995; 1996; Winter et al.,
93 1997; Dubinin and Sval'nov, 2000a,b; Dubinin and Sval'nov, 2003; Dubinin et al., 2008; 2013).
94 Although the early works hypothesized that, the Mn-micronodules have diagenetic origin
95 (Immel, 1974; Immel and Osmond, 1976) later studies attempted to relate their chemistry and
96 growth to the depositional environment (Ohashi, 1985; Sugisaki et al., 1987; Chauhan and Rao,
97 1999), biogenic activity (Banerjee and Iyer, 1991) and seafloor hydrothermal discharge (Sugitani,
98 1987; Dekov et al., 2003).

99 A review of all previous works on the seafloor Mn-micronodules reveals that our current
100 knowledge on them is incomplete and has some gaps:

101 (1) Previous geochemical investigations of the Mn-micronodules report mainly on their
102 major (Mn, Fe), some trace (Cu, Co, Ni) and rare earth elements concentrations and only few
103 works (Dekov et al., 2003; Dubinin et al., 2013; Yasukawa et al., 2020) provide data on wide
104 range of trace elements. Thus, a modern evaluation of the economic potential of the Mn-
105 micronodules needs information for the concentrations of a wide spectrum of elements in them.

106 (2) The studies on Mn-micronodules/Mn-nodules pairs were at random sample sites and did
107 not consider the differences in Mn-nodule facies. A correct assessment of the processes of trace
108 element concentration in the Mn-micronodules/Mn-nodules requires consideration of the nodule
109 facies.

110 (3) The hypotheses for diagenetic origin of the Mn-micronodules were rather inferred
111 logically (Mn-micronodules form in the sediment pore space filled with pore waters that are
112 diagenetic fluids) than based on combined studies of Mn-micronodules and corresponding pore
113 waters. This has resulted in speculative conceptions for the sources of elements to the Mn-
114 micronodules.

115 (4) The conventional geochemical approaches (like elemental concentrations and ratios)
116 cannot further extend our knowledge on the origin and evolution of the Mn-micronodules as
117 important components of the global Mn cycle. The stable isotope ratios of transition elements
118 (e.g., Fe, Cu, Zn) can provide new possibilities for getting insight into the processes of Mn-
119 micronodule (-nodule) formation (e.g., precipitation, adsorption, redox reactions) and trace metal
120 concentration (e.g., source of metals). We are not aware of any published Fe-Cu-Zn-isotope data

121 for Mn-micronodules and the available data for Fe-Cu-Zn-isotope composition of Mn-nodules
122 are scarce: 20 sub-samples from 5 Mn-nodules analyzed for Fe isotopes (Beard and Johnson,
123 1999; Levasseur et al., 2004; Marcus et al., 2015), surface layers of 31 Mn-nodules analyzed for
124 Cu isotopes (Albarède, 2004), and surface layers of 40 Mn-nodules analyzed for Zn isotopes
125 (Maréchal et al., 2000).

126 These limitations of our knowledge on the Mn-micronodules motivated us to undertake a
127 study of the mineralogical, chemical (major, trace, and rare earth elements) and Fe-Cu-Zn-isotope
128 composition of pairs Mn-micronodules/Mn-nodules from different facies at the Clarion-
129 Clipperton Mn-nodule field along with the chemistry of pore waters from the sediment that hosts
130 the micronodules and nodules. Here we report the results of this study.

131

132 **2. Geologic setting and Mn-nodule facies**

133

134 Samples for this study were collected from the French exploration contracts managed by
135 the International Seabed Authority in the Clarion-Clipperton zone (CCZ) (Fig. 1) during the
136 BIONOD cruise (April-May, 2012) onboard the R/V *L'Atalante*. The area of investigations is a
137 part of the province of abyssal hills (Morel and Le Suavé, 1986; Le Suavé, 1989). Although a
138 hilly area (Fig. 1) it was described as a sedimentary plateau in a general sense (Morel and Le
139 Suavé, 1986; Le Suavé, 1989). Red pelagic clays with minor biogenic component (tests of
140 foraminifera and radiolarians) are the principle sediment type in the area. Their vertical profile
141 shows signs of gravity mass movements interpreted to be a result of submarine erosion and
142 tectonic readjustments (Morel and Le Suavé, 1986; Le Suavé, 1989). Details on the variations of
143 the seafloor morphology, sediment thickness, sediment erosion, and their tectonic and hydrologic
144 controls can be found elsewhere (Morel and Le Suavé, 1986). Primary productivity in the surface
145 waters above the studied seafloor is estimated to be moderate (Veillette et al., 2007). Bottom-
146 water temperature is $\sim 1^{\circ}\text{C}$ and near-bottom currents have velocity of 3.5-4 cm/s (Veillette et al.,
147 2007).

148 Previous studies in the area (Veillette et al., 2007) defined four Mn-nodule facies (0, A, B
149 and C) that differ in shape, size, surface morphology and the degree to which Mn-nodules are
150 exposed above the sediment-water interface (Fig. 1). Facies 0 does not contain any Mn-nodules at
151 the sediment surface. Facies A contains small (10-20 mm) rounded Mn-nodules with granular

152 surface and has a high density of Mn-nodules coverage. Facies B contains Mn-nodules of
153 medium size (20-80 mm) and pieces of broken Mn-nodules, which often show patterns of
154 secondary growth healing the broken surfaces. The density of Mn-nodule coverage of facies B is
155 high. The nodules' upper surfaces are smooth whereas their lower surfaces are granular and an
156 equatorial belt is often present. Facies C contains big nodules, >80 mm in diameter. Their upper
157 surface is smooth whereas their lower surface is botryoidal and granular. The equatorial belt is
158 well pronounced. As it marks the limit between the buried part of the Mn-nodule in the sediment
159 and the part in contact with seawater, it seems that a large part of these Mn-nodules is buried in
160 the sediment (more than a half of the Mn-nodule). The nodule density coverage is high.

161

162 **3. Samples and methods of investigation**

163

164 *3.1. Sampling and sample preparation*

165

166 Mn-nodules and underlying sediment were sampled with USNEL box-corer (50 x 50 cm) at
167 15 sites located within the areas of distribution of the nodule facies 0 (6 box-cores), B (6 box-
168 cores) and C (3 box-cores) (Fig. 1; Table 1). Two deployments of the box-corer in the facies A,
169 located in a small area surrounded by pillow lava flows (Fig. 1), failed.

170 Mn-nodules were collected by hand, washed with distilled water, transferred into plastic
171 bags and stored in a fridge at ~4°C. Mn-micronodule extraction from the sediment began
172 immediately after recovery of the box-cores. The uppermost two sediment layers, 0-5 cm and 5-
173 10 cm, were wet-sieved in order to collect the >250 µm fraction that was inferred to contain the
174 major part of the Mn-micronodules (Immel and Osmond, 1976). After drying in an oven with
175 laminar air flow at 30°C for 24 hours the Mn-micronodule concentrates were further purified by
176 hand-picking of the detrital grains and biogenic remnants by steel needle under stereo-
177 microscope (WILD M8).

178 Dried Mn-micronodules and paired Mn-nodules from the sediment surface were ground
179 manually in an agate mortar up to fine powders, which were used in all further analyses.

180 Aiming at figuring out the sources of elements to the Mn-micronodules and Mn-nodules we
181 sampled and analysed the pore waters from the sediment hosting the Mn-micronodules and
182 underlying the Mn-nodules. Plexiglas push cores (10 cm diameter, 50 cm length) with holes (2

183 mm diameter) every centimeter along the core were inserted into the sediment in the box-corer
184 immediately after recovery. Pore waters were extracted from the sediment taken in the Plexiglas
185 push core using Rhizons® flex with nylon wire (Rhizosphere Research products) in cold (4°C)
186 laboratory environment following the method described by Seeberg-Elverfeldt et al. (2005). The
187 Rhizons® were inserted into the sediment through the holes of the Plexiglas push core every
188 centimeter in the upper 20 centimeters of the core, and then every 2 centimeters for the remaining
189 core. We waited for two hours until the syringes collected enough pore water (5 - 10 mL) and
190 then transferred the pore waters in 15 mL Nalgene vials pre-cleaned with 10% HCl. Collected
191 pore waters were stored in refrigerator (~4°C) before further analyses.

192

193 *3.2. Mineralogical, morphological, and internal structure studies*

194

195 The bulk mineralogical composition of 28 finely powdered sub-samples including Mn-
196 micronodules and Mn-nodules was determined by X-ray diffraction (XRD) analysis (Panalytical
197 X'Pert Pro X-ray diffractometer with monochromatic Co K_{α} radiation) of random mounts in Si
198 low-background sample holder: X-ray scans from 1 to 85° 2 θ , with 0.03° 2 θ step, 15 s/step
199 measuring time, automatic divergence slit, and Ni- K_{β} filter at the BGR and IFREMER.

200 Due to the possible occurrence of two different 10 Å manganese phases, such as 10 Å
201 vernadite (phylломanganate) and todorokite (tectomanganate), a drying procedure was necessary
202 before the XRD analysis. Both the 10 Å vernadite and todorokite have a layer-to-layer distance of
203 ~10 Å, which is due to hydrated cations (e.g., Mg) within the interlayers (Bodeř et al., 2007). In
204 addition to the octahedra layers, the todorokite has also vertical octahedra walls (3 to 10
205 octahedra), which stabilize the sheet structure against collapsing and form a so called “tunnel
206 structure” (Bodeř et al., 2007). After heating the samples at 105°C for 24h, the 10 Å peak of the
207 phylломanganates will decrease and therefore, the 7 Å peak will increase (7 Å vernadite), or the
208 10 Å peak will collapse completely. In contrast, the 10 Å peak of todorokite will remain
209 unchanged upon heating at 105°C (e.g., Manceau et al., 2014; Wegorzewski et al., 2020).
210 Therefore, we performed XRD analyses of six Mn-micronodule samples twice: after sample
211 drying at 30°C, and after sample heating at 105°C for 24h (e.g., Uspenskaya et al., 1987;
212 Wegorzewski et al., 2015).

213 For a better mineralogical characterization, we analysed ten Mn-micronodule samples from
214 different Mn-nodule facies and two Mn-nodule standards (Nod-P-1 and Nod-A-1) by Fourier-
215 Transformed Infrared Spectroscopy (FTIR). The mid- (MIR) and far- (FIR) infrared spectra were
216 collected on pressed pellets made of 1 mg sample mixed with 200 mg KBr. The analyses were
217 carried out on a ThermoNicolet Nexus FTIR spectrometer (MIR beam splitter KBr, detector
218 DTGS TEC; FIR beam splitter solid substrate, detector DTGS PE) at the BGR. The resolution
219 was adjusted to 2 cm⁻¹.

220 Morphology of the Mn-micronodules was studied using FEI Quanta 200 scanning electron
221 microscope (SEM) (V=10 kV, I=100 μA, electron beam diameter of 2 μm) at IFREMER.
222 Secondary electron images (SEI) and energy dispersive X-ray spectra (EDS) were obtained on
223 selected Mn-micronodules, mounted on aluminum stubs using carbon tape and coated with Au.

224 The internal structure of the Mn-micronodules was investigated on carbon-coated polished
225 section of Mn-micronodules (impregnated with araldite in a block; sample NODKGS63 0-5 cm)
226 by FEI Quanta 600 FEG SEM at BGR. Back-scattered electron images (BEI) were obtained
227 through scanning of the specimen with a focused electron beam (diameter 1-5 μm, maximum
228 magnification 250000 times) produced by a field emission gun (W-crystal) using a 20 kV
229 acceleration under high vacuum conditions (9-10 mbar).

230

231 *3.3. Dissolved oxygen concentration profiles in the sediment*

232

233 Dissolved oxygen concentrations were measured across the collected sediment (box-corer)
234 using a Clark-type oxygen microprobe provided with an included reference and an internal
235 cathode. The micro-sensor had a diameter of ≤100 μm at its extremity. The elapsed time prior to
236 the response was 90% in less than 10 seconds. Signal collected by the probe (oxygen tension)
237 was recorded after signal amplification.

238 In each box-core we performed oxygen concentration profiles at both (1) sediment surface
239 free of Mn-nodules, and (2) sediment surface under a Mn-nodule.

240

241 *3.4. Elemental concentrations measurements of Mn-micronodules and Mn-nodules*

242

243 Concentrations of Mn, Fe, Si, Al, Ca, Mg, Na, K, Ti, P, S, Li, Be, B, Sc, V, Cr, Co, Ni, Cu,
244 Zn, Se, As, Rb, Sr, Y, Zr, Nb, Mo, Cd, Sn, Sb, Te, Ba, Hf, Ta, W, Tl, Pb, Bi, Th, U, Au, Pt and
245 REE in the Mn-micronodules and Mn-nodules (bulk samples) were measured by Inductively
246 Coupled Plasma-Mass Spectrometry (ICP-MS) (ThermoElectron Element XR) at the Pôle de
247 Spectrométrie Océan (PSO, IFREMER, Brest, France) after digestion of bulk powdered samples
248 according to the following procedure. About 5 mg of each sample (finely powdered) were
249 dissolved with 0.8 mL double-distilled concentrated HNO₃, 0.8 mL 6 M HCl and 0.2 mL
250 concentrated HF in 2 mL Teflon vials. After evaporation of the solutions to dryness on hot
251 (90°C) plate, the residues were re-dissolved with 0.2 mL double-distilled concentrated HNO₃ and
252 stored in 2 mL Teflon vials after adding of 1.8 mL 18.2 MΩ H₂O. The ICP-MS instrument was
253 calibrated using a set of Mn-nodule standards matching the Fe-Mn-oxyhydroxide matrices: Nod-
254 P-1 [United States Geological Survey (USGS) standard for Pacific Mn-nodule], and Nod-A-1
255 (USGS standard for Atlantic Mn-nodule). The analytical error (2σ) calculated on replicate
256 analyses of the standards was below 5% for most elements.

257 Chemical composition of the individual layer growth structures within the Mn-
258 micronodules was investigated on a carbon-coated polished block section (sample NODKGS63
259 0-5 cm) by Electron Probe Micro-Analyzer (EPMA) (JEOL JXA-8530F) at BGR. The diameter
260 of the EPMA electron beam was adjusted between 5 and 20 μm, depending on the dimension of
261 the growth structures and type of the material. The accelerating voltage was set at 15 kV and a
262 beam current of 40 nA was used. The counting times for the analyzed elements were: 10 s for
263 Mn, Fe, Ni, Cu, Na, Mg, Al, Si, K, Ca, Ti, P, and S, 40 s for V, 50 s for Co, 100 s for Ba, and
264 Mo. Rhodochrosite (Mn), haematite (Fe), cobaltite (Co), synthetic Ni₂Si (Ni), cuprite (Cu), albite
265 (Na), kaersutite (Mg, Al, Si), biotite (K), apatite (Ca, P), rutile (Ti), barite (S, Ba), molybdenite
266 (Mo), and vanadium metal (V) were used as standards (BGR standards). According to the high
267 water content of the different Mn-(oxy)hydroxides (up to 25 % for phyllomanganates; Jones and
268 Milne (1956), Chukhrov et al. (1979)) and the high porosity of the samples, total analytical sums
269 of >60% were accepted (e.g., Wegorzewski and Kuhn, 2014).

270

271 *3.5. Elemental concentrations measurements of pore waters*

272

273 Concentrations of Na, K, Ca, Mg, S, Si, B, Sr, Fe, Mn, Al, P, Li, Rb, Ba, Mo, V, Zn, Cu,
274 Ni, Co, Cr, Cd, U, Ti, Ge, La, Ce, and Nd in the pore waters of core NODKGS65 were measured
275 by ICP-MS (ThermoElectron Element XR) at the Pôle de Spectrométrie Océan (PSO, Ifremer,
276 Brest, France) in 2 mL aliquots of 100-fold diluted (with 18.2 MΩ H₂O) pore water samples. The
277 ICP-MS instrument was calibrated using a set of in-house (SW-XR-2) and internationally-
278 certified (NASS-5 and IAPSO) seawater standards matching the pore waters matrices. The
279 analytical error (2σ) calculated on replicate analyses of the standards was below 3% for most
280 elements. The procedural blanks were below the detection limits of the instrument for all
281 measured elements.

282

283 3.6. Fe-Cu-Zn-isotope analysis of Mn-micronodules and Mn-nodules

284

285 For Fe-Cu-Zn-isotope analyses of the Mn-micronodules and Mn-nodules, we put 1 mL
286 from each of the stored after total digestion sample solutions in 2 mL Teflon vials and evaporated
287 them to dryness on a hot plate (90°C). The residues were re-dissolved with 1 mL 10 M HCl.
288 Sample solutions were ready for column load after addition of 10 μL H₂O₂ in each sample.

289 Fe, Cu and Zn were separated from the matrix components (element purification) by anion-
290 exchange chromatography using AG MP-1 resin (2.0 mL wet volume in Teflon columns). Blanks
291 and standards (Nod-P-1) were included in the sample sets and subjected to the same anion-
292 exchange chromatography procedure. Our protocol contained six major steps: (1) columns with
293 AG MP-1 resin were washed with 10 mL 3 M HNO₃, 10 mL 18.2 MΩ H₂O, 5 mL 1.2 M HCl and
294 2 mL 10 M HCl; (2) samples (in 1 mL 10 M HCl with 10 μL H₂O₂) were loaded on the columns
295 and the matrix fraction was eluted with 6.5 mL 10 M HCl; (3) Cu fraction was recovered in 23
296 mL Teflon vials with 16 mL 5 M HCl; (4) Fe fraction was recovered in 15 mL Teflon vials with
297 14 mL 1.2 M HCl; (5) Zn fraction was recovered in 15 mL Teflon vials with 14 mL 0.0012 M
298 HCl; (6) columns were washed with 10 mL 18.2 MΩ H₂O. All elutions were evaporated to
299 dryness at 90°C, re-dissolved in 2 mL ~0.28 M HNO₃ and transferred into 2 mL vials.

300 Isotope ratios (⁵⁶Fe/⁵⁴Fe, ⁵⁷Fe/⁵⁴Fe, ⁵⁷Fe/⁵⁶Fe, ⁶⁵Cu/⁶³Cu, ⁶⁶Zn/⁶⁴Zn and ⁶⁸Zn/⁶⁶Zn) were
301 measured with a *Neptune* multi-collector inductively coupled plasma mass spectrometer (MC-
302 ICP-MS) at the Pôle de Spectrométrie Océan (PSO, Ifremer, Brest, France). Isotope ratios were

303 estimated relative to the same ratios measured for an isotope standard (IRMM-14 for Fe, NIST-
304 SRM 976 for Cu, and NIST-SRM 3168a for Zn) and reported in delta notation:

305
$$\delta^i E_{sample} = (R^{ij}_{sample}/R^{ij}_{standard} - 1) \times 1000,$$

306 where i and j are the specific isotopes used in ratio R of element E in the sample of interest and
307 standard reference material. Following the conventional practice, we use isotope i in the δ values
308 discussed in the paper and note the specific ratios R^{ij} we have used. All $\delta^{66/64}\text{Zn}_{sample}$ values
309 reported relative to our internal isotope standard NIST 3168a were recalculated relative to JMC-
310 Lyon isotope standard because this reference standard is commonly used in the literature for
311 reporting Zn isotope composition of natural samples (Archer et al., 2017). We determined
312 $\delta^{66/64}\text{Zn}$ value of NIST 3168a against the Zn-ETH isotope standard (Archer et al., 2017) and
313 obtained $\delta^{66/64}\text{Zn}$ value of $-1.207 \pm 0.028\text{‰}$, which corresponds to -0.94‰ relative to JMC-Lyon
314 isotope standard (using the consensus value of $\delta^{66/64}\text{Zn}$ of Zn-ETH against JMC-Lyon of 0.27‰).
315 Hence, $\delta^{66/64}\text{Zn}$ of SRM 3168a is 0.94‰ lower than JMC-Lyon.

316 Instrumental fractionation of Cu and Zn in the mass spectrometer during analysis was
317 corrected with internal isotopic standards Zn NIST SRM 3168a and Cu NIST SRM 976,
318 respectively, doped in Cu sample solution and Zn sample solution according to a Cu/Zn ratio of
319 1:2 coupled to a standard-sample-bracketing procedure (Marechal et al., 1999). Samples were
320 introduced in the plasma through a double quartz cyclonic spray chamber coupled to a $50 \mu\text{L}/\text{min}$
321 PFA nebulizer and isotopic ratios were measured in low resolution mode. Iron isotope ratios were
322 corrected using a Ni isotopic standard NIST SRM 986 doped in samples solution at a
323 concentration ratio Fe/Ni of 1:1, and a standard-sample-bracketing procedure was also employed
324 (Rouxel et al., 2005). Samples were introduced in the plasma through an Apex Q (Elemental
325 Scientific) desolvation introduction system coupled to a $50 \mu\text{L}/\text{min}$ PFA nebulizer. Iron isotopic
326 ratios were measured in medium resolution mode to resolve argide interferences.

327 The performance of the mass spectrometer for Fe, Cu and Zn isotope ratios measurements
328 was assessed through replicate measurements of isotopic standards (Fe IRMM-14, Cu NIST-
329 SRM 976, and Zn JMC and NIST-SRM 3168a). Precision on the samples is reported as a two-
330 standard deviation (2sd) calculated on replicate measurements of the isotopic standards. Replicate
331 analyses of digest replicates ($n=5$) of USGS geological reference material Nod-P-1 yielded
332 average values of $-0.58 \pm 0.04\text{‰}$ (2sd) for $\delta^{56/54}\text{Fe}_{\text{IRMM-14}}$; $0.33 \pm 0.03\text{‰}$ (2sd) for $\delta^{65/63}\text{Cu}_{\text{SRM976}}$;
333 and $1.72 \pm 0.06\text{‰}$ (2sd) for $\delta^{66/64}\text{Zn}_{\text{SRM3168a}}$. These isotopic values are consistent with the data

334 reported in the literature: for Fe (Dideriksen et al., 2006; Williams et al., 2014), and for Cu and
335 Zn (Chapman et al., 2006; Bigalke et al., 2010a; Little et al., 2017).

336

337 **4. Results**

338

339 *4.1. Mn-nodule distribution, and Mn-micronodule morphology and internal structure*

340

341 The deepest Mn-nodule facies, 0 (Table 1), does not contain Mn-nodules at the surface
342 (Fig. 2A). Small (<10 mm), rounded Mn-nodules (Fig. 2A) with finely granular surfaces were
343 scattered within the sediment. As stated above (see 3.1) we could not sample Mn-nodules of
344 facies A with box-corer, but we collected some with an epi-benthic sledge. Facies A is densely
345 covered (Fig. 2B) of small (10-20 mm), rounded, black nodules with granular surfaces (Fig. 2B).
346 The shallowest Mn-nodule facies, B (Fig. 2C), contains the highest abundance of nodules on a
347 surface unit: 17.4 kg/m² (Table 1). Mn-nodules of this facies are of medium size (20-80 mm),
348 flat, ellipsoidal (Fig. 2C) with smooth upper surface and botryoidal lower surface. Mn-nodule
349 facies C (Fig. 2D) is located at middle depths and contains 15.5 kg/m² nodules in average (Table
350 1). These nodules are big (>80 mm), ellipsoidal, flat (Fig. 2D) with smooth upper surface and
351 botryoidal lower surface.

352 Mn-micronodules are either elongated (Fig. 3A) or isometric (Fig. 3B). They are black,
353 with botryoidal surfaces (Fig. 3A,B). We could not find any relation of their morphology with the
354 depth of occurrence in the sediment.

355 Mn-micronodules appear to have concentrically zoned internal structure composed of
356 concentric fine dense layers (Fig. 3C-F) that form botryoidal and columnar growth structures
357 (Fig. 3C,D).

358

359 *4.2. Mineralogy of Mn-micronodules and Mn-nodules*

360

361 *4.2.1. X-ray diffraction analysis*

362 The XRD patterns of all analysed samples showed two diffraction humps (broad and of low
363 intensity) at ~9.5 Å (001) and at ~7 Å (001) with *hk* bands around ~2.45 Å (10) and ~1.42 Å (01;
364 Fig. 4; Appendixes 1-3). The first hump can be assigned to two different Mn-minerals: 10 Å

365 distorted phyllomanganate (vernadite) and 10 Å tectomanganate (todorokite) (Bodeï et al., 2007;
366 Wegorzewski et al., 2015). After heating the samples at 105°C for 24h, the hump at ~9.5 Å
367 disappeared completely and the 7 Å peak increased and became more distinct. This is common
368 for the phyllomanganates. Furthermore, no splitting of the peak at ~2.45 Å (to 2.45 and 2.39 Å),
369 which is typical for todorokite (Manceau et al., 2014; Wegorzewski et al., 2020) was observed
370 (Fig. 4). This suggests that the studied Mn- micronodules and nodules are composed of 10 Å
371 phyllomanganates, but not of tectomanganates like todorokite or even of “defected” todorokite
372 (Bodeï et al., 2007; Wegorzewski et al., 2015; 2020). Furthermore, a turbostratic 7 Å vernadite
373 phase can be recognized, already before the heating. The occurrence of a third phyllomanganate
374 such as vernadite (δ -MnO₂) cannot be excluded. The δ -MnO₂ (vernadite) shows only two *hk*
375 bands at the XRD pattern (~2.45 and 1.42 Å) and they are similar to those of the 10 and 7 Å
376 phyllomanganates (Fig. 4). Vernadite seems to be intergrown with an X-ray amorphous Fe-phase
377 and therefore without a stacking order in *c** direction, resulting in the absence of the 00*l*
378 reflections (Burns and Burns, 1977). The layer symmetry of the phyllomanganates that compose
379 the studied Mn- micronodules and nodules is hexagonal because the calculated ratio of the d-
380 spacings of the two *hk* bands is ~1.73 (close to $\sqrt{3}$) and the band at ~1.42 Å is almost symmetrical
381 (e.g., Drits et al., 1997; Bodeï et al., 2007; Drits et al., 2007). Presence of significant amounts of
382 asbolane is unlikely, because the 002 reflection of the phyllomanganates is of lower intensity
383 than the 00*l* reflection (Fig. 4).

384 In addition to the major Mn-(Fe)-minerals, minor amounts of detrital quartz and feldspars
385 were detected in the studied Mn- micronodules and nodules (Fig. 4; Table 2).

386

387 4.2.2. Infrared spectroscopy

388 The FTIR spectra of the Mn-micronodules and Mn-nodule standards (Fig. 5; Appendix 4)
389 show two to three bands, which are characteristic for Mn-phases (Wegorzewski et al., 2020). The
390 bands in the region between 800 and 400 cm⁻¹ arise from Mn-O lattice vibrations (Kang et al.,
391 2007). The hydrogenetic Mn-nodule standard (Nod-A-1) shows a hump around 433 cm⁻¹ and a
392 distinct band at 464 cm⁻¹. The mixed hydrogenetic-diagenetic nodule standard (Nod-P-1) displays
393 bands at 433 (weak), 464 (strong) and 502 cm⁻¹ (medium), respectively. The FTIR spectra of the
394 Mn-micronodules are similar to the FTIR spectrum of Nod-P-1: bands at 426-434 cm⁻¹, 462-468
395 cm⁻¹, and 501-512 cm⁻¹ (Fig. 5; Appendix 4). These three bands correspond to the IR

396 characteristics of layered Mn-oxides (Potter and Rossman, 1979; Golden et al., 1986; Kang et al.,
397 2007; Wegorzewski et al., 2020). No IR bands typical for a tectomanganate like todorokite could
398 be distinguished. According to the previous IR studies (Julien et al., 2004; Atkins et al., 2014;
399 Wegorzewski et al., 2020) a band at $\sim 748\text{-}760\text{ cm}^{-1}$ occurs in the IR spectra if todorokite is the
400 main Mn-mineral in the studied samples. The lack of this band in the FTIR spectra of the studied
401 Mn-micronodules testifies that todorokite is not present.

402

403 *4.3. Geochemistry of Mn-micronodules and Mn-nodules*

404

405 At the site NODKGS49 we recovered sediment with Mn-micronodules only, but did not
406 find any Mn-nodules on the sediment surface (facies 0). Site NODKGS44 (facies 0) is close to
407 site NODKGS49 (Fig. 1) and we found rare Mn-nodules on the sediment surface. Therefore, we
408 may consider as a pair representative for facies 0 the Mn-nodule and Mn-micronodules collected
409 at sites NODKGS44 and NODKGS49, respectively.

410 The Mn-micronodules are richer in Mn, Cu, Ni, Zn, and Sn (two to five times), Cr, Sb, K,
411 Mg, and Rb than the Mn-nodules (Table 3). Mn/Fe ratios of the Mn-micronodules are two to
412 three times higher than that of the Mn-nodules. The Mn-micronodules of facies 0 are the richest
413 in Si, whereas the micronodules of facies C are the poorest in Si. Mn-micronodules of facies 0
414 contain more Ca than the paired Mn-nodules. This trend is opposite for the Mn-micronodule/Mn-
415 nodule pairs of facies B, whereas the Mn-micronodules and Mn-nodules of facies C have similar
416 Ca concentrations. Titanium, Sr, and Pb are more abundant in the Mn-micronodules than in the
417 Mn-nodules of facies 0, but less in the micronodules than in the nodules of facies B and C.
418 Molybdenum concentrations are higher in the micronodules than those in the nodules of both
419 facies 0 and C, and are similar in both micronodules and nodules of facies B. Tungsten and Bi are
420 more abundant in the micronodules than in the nodules of facies 0 and C, and more abundant in
421 the nodules than in micronodules of facies B. Manganese, Cu, Co, Ni, Cd, Sb, As, Tl, U, Na, and
422 REE concentrations in the micronodules generally increase upward the sediment cores towards
423 the sediment/seawater interface. Potassium increases upward the sediment in the Mn-
424 micronodules from facies 0 and B, but decreases upward in the Mn-micronodules of facies C
425 (Table 3).

426 The studied Mn-nodules are richer in Al, Sc, Nb, Ta, Li, Be, B, V, Co, As, Cd, Ba, and U
427 than the Mn-micronodules (Table 3). The concentrations of Fe, S, Na, Pt, Zr, and REE in them
428 are about two times (P, Te, Tl, Hf, and Th up to two-three times; Y two to five times) higher than
429 those in the Mn-micronodules (Tables 3, 4). Content of Se is the highest in the Mn-nodules of
430 facies B and the lowest in the nodules of facies 0 (Table 3).

431 Mn-micronodules from the facies 0 have positive Ce anomaly whereas the Mn-nodules
432 from the same facies have weak negative Ce anomaly (Table 4; Fig. 6A, B). In facies B and C
433 both the micronodules and nodules have positive Ce anomaly, but it is higher in the micronodules
434 than in the nodules (Table 4; Fig. 6C-F). The positive Ce anomaly of the Mn-micronodules from
435 all the facies decreases upwards the sediment (Table 4).

436 Mn- micronodules and nodules from all facies have weak positive Eu anomaly (Table 4;
437 Fig. 6A-F). It is larger in the micronodules than in the nodules (Table 4). In the micronodules
438 from facies 0 and B the Eu anomaly slightly decreases upwards, whereas in the micronodules
439 from facies C it slightly increases (Table 4).

440 Mn- micronodules and nodules from all facies show a slight depletion in the light REE
441 relative to the heavy REE ($La_{NASC}/Lu_{NASC} < 1.00$; Table 4). The Mn-nodules are more depleted in
442 light REE than the micronodules (Table 4).

443 North American Shale Composite (NASC)-normalized REE distribution patterns of the
444 investigated Mn-nodules (Fig. 6A, C, E) are similar to that of the Pacific Mn-nodule standard
445 (Nod-P-1, Fig. 6G). The NASC-normalized REE distribution patterns of the Mn-micronodules
446 (Fig. 6B, D, F) also show some similarity to that of the Pacific Mn-nodule standard (Fig. 6G), but
447 exhibit more pronounced positive both Ce and Yb anomalies. Their positive Ce anomaly is
448 similar to that of the Atlantic Mn-nodule standard (Nod-A-1, Fig. 6H).

449

450 *4.4. Geochemistry of individual growth structures of Mn-micronodules*

451

452 EPMA analyses of the individual growth structures of the Mn-micronodules show high
453 Mn/Fe ratios (2.6 - 699) and Ni+Cu content (1.11 - 5.45 wt.%), while Co contents range from
454 below the detection limits to 0.5 wt.% (Table 5). Nickel and Cu are highly enriched in the growth
455 structures with high Mn/Fe ratio (>6) whereas Co is enriched in the growth structures with lower
456 Mn/Fe ratio (<6). Conspicuous are the very high Mo concentrations of up to 1196 mg/kg in

457 growth structures with low Mn/Fe ratios and up to 1877 mg/kg in growth structures with high
458 Mn/Fe ratios (Table 5).

459 In general, three different layer growth structures can be distinguished according to their
460 reflectivity and chemistry. Layer type 1 has low reflectivity and low analysis totals (66 – 73
461 wt.%), probably a result of the porosity of these growth structures. It has low Mn/Fe ratios (2.6 –
462 6), low Ni+Cu content (1.11 – 1.88 wt.%) and Co contents varying from 0.14 to 0.5 wt.%. These
463 growth structures occur rarely, mostly as coatings around the Mn-micronodules (Fig. 3E,F).

464 The studied Mn-micronodules consist mostly of layer growth structures with high Mn/Fe
465 (>>6), high Ni+Cu content, and low Co concentrations (Layer type 2; Table 5). These layer
466 growth structures can be divided into two sub-types according to their reflectivity.

467 Layer type 2a is dense and has high reflectivity (Fig. 3C-F). Layer growth structures of this
468 type have Mn/Fe ratios varying from 34 to 699, Ni+Cu content between 1.44 and 5.45 wt.%, low
469 Co content (<0.07 wt.%) and Mo concentrations up to 1704 mg/kg (Table 5).

470 Layer type 2b has high porosity and low reflectivity (Fig. 3C-E). These layer growth
471 structures have Mn/Fe ratios varying from 8 to 95 and Ni+Cu content slightly lower than that of
472 the layer type 2a (1.93 - 4.17 wt.%). Cobalt content of this layer type is up to 0.5 wt.% whereas
473 Mo content is up to 1877 mg/kg (Table 5).

474

475 *4.5. Geochemistry of pore waters*

476

477 Vertical distributions of the elemental concentrations in the pore waters along the sediment
478 core NODKGS65 (Table 6) show three distinct trends (Fig. 7).

479 (1) Manganese and Fe show relatively stable vertical distribution with similar
480 concentrations along the core with an exception of Mn content increase in the uppermost
481 sediment layer (0-1 cm) (Fig. 7). Phosphorous and Zn also show a similar vertical trend, but have
482 a slight increase in the uppermost (0-5 cm) sediment layer (Fig. 7).

483 (2) Upward decrease in the content of Si, S, Mg, Ca, and Cr (Fig. 7). Two different patterns
484 of vertical decrease are observed for the different elements: (a) a steady upward decrease along
485 the entire upper 40 cm of the sediment (Si), and (b) an increase in the content from ~40 cm to 20-
486 10 cm sediment depth and decrease toward the seafloor (seawater/sediment interface) (S, Mg, Ca,
487 and Cr; Fig. 7).

488 (3) Upward increase in the content of Na, K, Rb, Li, Mo, Cd, B, Ni, V, Cu, Ba, Co, U, and
489 Sr (Fig. 7). Although the patterns of increase of the concentrations of these elements differ in
490 details the general trend of their vertical distribution is upward increase.

491 We do not have data for the vertical distribution of dissolved O₂ concentration along the
492 sediment core NODKGS65. Therefore, in our interpretations of the vertical distribution of
493 elements dissolved in the pore waters of core NODKGS65 we will use the dissolved O₂ profiles
494 along the sediment core NODKGS63, which is close to NODKGS65 (Fig. 1). Dissolved O₂
495 distribution along the sediment core NODKGS63 and close to a Mn-nodule shows abrupt
496 downward decrease from 177 μmol/L in the bottom seawater to ~60 μmol/L at 1 cm depth and
497 then gradual decrease to ~31.5 μmol/L at 8 cm depth in the sediment (Fig. 7). Dissolved O₂
498 profile beneath the same Mn-nodule (from the same core) shows similar distribution pattern:
499 sharp decrease from ~120 μmol/L just below the Mn-nodule to ~52 μmol/L at 0.5 cm depth
500 followed by a smooth downward decrease to ~30 μmol/L at 9 cm depth (Fig. 7). Similar vertical
501 distribution of dissolved O₂ in the pore waters of sediments is observed east from the studied
502 area, but still within the CCZ (Mewes et al., 2014, 2016; Kuhn et al., 2017a; Volz et al., 2018):
503 [O₂] ~150-160 μmol/L in the bottom seawater, its abrupt decrease to ~50 μmol/L within the
504 upper 5-6 cm of the sediment and a smooth decrease to suboxic values ([O₂] < 5 μmol/L; Hein
505 and Koschinsky, 2014). The oxic-suboxic front (oxygen penetration depth) was found at 1.8-3.0
506 m (Mewes et al., 2014).

507

508 4.6. Fe-Cu-Zn-isotope composition of Mn-micronodules and Mn-nodules

509

510 Mn-micronodules have Fe-isotope composition ($\delta^{56}\text{Fe} = -0.43 - -0.27\text{‰}$) slightly heavier
511 than that of the paired Mn-nodules ($\delta^{56}\text{Fe} = -0.63 - -0.39\text{‰}$) (Table 7; Fig. 8A). Fe-isotope
512 composition of the studied Mn- micronodules and nodules falls within the $\delta^{56}\text{Fe}$ range of the Mn-
513 nodules [from -1.27 to -0.07‰; Beard and Johnson (1999), Levasseur et al. (2004), Marcus et al.
514 (2015)] and Fe-Mn-crusts [from -1.12 to +1.54‰; Zhu et al. (2000), Chu et al. (2003), Levasseur
515 et al. (2004), Horner et al. (2015)] measured so far, and is lighter than that of the terrestrial
516 igneous rocks [0.09‰; Beard and Johnson (2004)] (Fig. 9A). $\delta^{56}\text{Fe}$ of the Mn-micronodules from
517 facies 0 gets lower upward the sediment cores (towards the seawater-sediment interface), whereas

518 that of the micronodules from facies B and C does not change (within the error) across the
519 sediment (Table 7).

520 Mn-micronodules ($\delta^{65}\text{Cu} = +0.20 - +0.35\text{‰}$) and paired Mn-nodules ($\delta^{65}\text{Cu} = +0.21 -$
521 $+0.35\text{‰}$) have similar (within the error) Cu-isotope composition (Table 7; Fig. 8B), which falls
522 within those of the Mn-nodules [from $+0.05$ to $+0.60\text{‰}$; Albarède (2004)] and Fe-Mn-crusts
523 [from $+0.12$ to $+0.58\text{‰}$; Little et al. (2014b)] investigated previously, and is heavier than that of
524 the terrestrial igneous rocks [0‰ (Albarède, 2004); 0.06 - 0.07‰ for bulk silicate Earth (Moynier
525 et al., 2017)] (Fig. 9B). A slight decrease in $\delta^{65}\text{Cu}$ of Mn-micronodules is observed upward the
526 sediment cores (Table 7).

527 The range of Zn-isotope composition of the Mn-micronodules ($\delta^{66}\text{Zn}_{\text{JMC}} = +0.61 -$
528 $+0.90\text{‰}$) is slightly wider than that of the Mn-nodules ($\delta^{66}\text{Zn}_{\text{JMC}} = +0.75 - +0.87\text{‰}$) although the
529 Zn-isotope composition of the paired micronodules-nodules is quite similar (Table 7; Fig. 8C).
530 They both are within the range of the Zn-isotope composition of the Mn-nodules [from $+0.53$ to
531 $+1.16\text{‰}$; Maréchal et al. (2000)] and at the lighter end of the Zn-isotope composition of the Fe-
532 Mn-crusts [from $+0.80$ to $+1.23\text{‰}$; Little et al. (2014b)] studied so far, and are heavier than that
533 of the terrestrial igneous rocks [$0.2 - 0.3\text{‰}$ (Albarède, 2004; Chen et al., 2013); 0.15‰ for bulk
534 silicate Earth (Moynier et al., 2017)] (Fig. 9C). $\delta^{66}\text{Zn}$ of the Mn-micronodules does not show a
535 visible change (within the error) upward the sediment cores (Table 7).

536

537 **5. Discussion**

538

539 *5.1. Mineralogy of Mn-micronodules*

540

541 Previous works on the mineralogy of the Mn-micronodules (Kidd and Ármannson, 1979;
542 Lallier-Verges and Clinard, 1983; Poppe et al., 1984; Stoffers et al., 1984; Dekov et al., 2003; Ito
543 et al., 2005; Liao et al., 2019; Li et al., 2020) reported that the main minerals that compose the
544 Mn-micronodules are todorokite and δ - MnO_2 . Birnessite and buserite were reported rarely.
545 Mineralogical determinations in most of these works were based on conventional powder XRD
546 only, which casts some doubt on the precision of these determinations. Therefore, we put a little
547 effort on the precise mineralogy of the studied Mn-micronodules.

548 Our XRD and IR spectroscopy analyses showed clearly that the studied Mn-micronodules
549 and Mn-nodules are dominantly composed of phylломanganates (10 Å and 7 Å vernadites) and
550 vernadite (δ -MnO₂). The vernadite and an X-ray amorphous FeOOH were inferred on the basis of
551 the EPMA analyses of the layer growth structures. Vernadite intergrown epitaxially with X-ray
552 amorphous FeOOH is typical for the layer growth structures with low Mn/Fe ratios
553 (Wegorzewski and Kuhn, 2014; Wegorzewski et al., 2015). The low intensity and broadness of
554 the 10 Å and 7 Å peaks at the XRD patterns indicated high distortion of the Mn-octahedral layers
555 as well as very low stacking order of the phylломanganates (Bodeř et al., 2007).

556 Presence of todorokite in the studied Mn- micronodules and nodules is not supported by
557 our XRD and IR studies. The chemical composition of the Mn-micronodules supports the XRD-
558 IR based conclusion that there is no todorokite. In general, the todorokite-rich Mn-nodules
559 incorporate much lower amounts of Ni and higher amounts of Cu than the phylломanganate-rich
560 Mn-nodules (Atkins et al., 2014; Heller et al., 2018; Wegorzewski et al., 2020). This suggests
561 that the studied Mn- micronodules and nodules (Tables 3, 5) are composed of phylломanganates.
562 Furthermore, the Mg concentrations of the Mn- micronodules and nodules (Tables 3, 5) are too
563 low for being todorokite-rich. In principle, the Mn-nodules may contain minor amounts of
564 “defected” todorokite (Bodeř et al., 2007) rather than todorokite (Wegorzewski et al., 2015;
565 2020). According to the recent studies (Wegorzewski et al., 2020) todorokite appears to be a
566 typical transformation product of 10 Å phylломanganates after being buried in the sediment
567 column (down to 5 – 10 m) at prevailing suboxic-conditions for a long period of time.

568

569 *5.2. Origin of Mn-micronodules*

570

571 *5.2.1. Trace elements constraints*

572 The Mn/Fe ratio and trace element content of the seafloor Fe-Mn-oxyhydroxide deposits
573 have been employed to relate the deposits to their mode of formation (Bonatti et al., 1972;
574 Halbach et al., 1988; Wegorzewski and Kuhn, 2014; Josso et al., 2017). The triangular
575 discrimination diagram of Bonatti et al. (1972) that considers the contents of Fe, Mn and the
576 essential trace elements Cu, Ni and Co in the Fe-Mn-deposits has been widely used. This simple
577 and easily understandable geochemical approach motivated many scientists to improve and make
578 it more precise. Thus, Halbach et al. (1988) proposed a similar diagram recently improved by

579 Wegorzewski and Kuhn (2014), whereas Josso et al. (2017) involved additionally in this
580 conception both the high field strength (HFSE) and rare earth elements.

581 Employing the diagrams of Wegorzewski and Kuhn (2014) and Josso et al. (2017) (Fig.
582 10A, B) we can see that the studied Mn-micronodules are diagenetic precipitates (Fig. 10A) that
583 are a result of suboxic diagenesis (Fig. 10B). This conclusion seems to be in contradiction with
584 the current redox state of the pore waters in the sediments from where the Mn-micronodules were
585 collected (0-5, and 5-10 cm) (Fig. 7). Although the dissolved O₂ vertical distribution across the
586 studied sediment shows that below 1 cm depth [O₂] (~60-30 μmol/L) is 3-6 times lower than that
587 of the bottom seawater (177 μmol/L) (Fig. 7) the dissolved O₂ concentrations are still well above
588 the suboxic value ([O₂] < 5 μmol/L; Hein and Koschinsky, 2014) [see Tostevin and Poulton
589 (2019) for suboxic sediment characteristics]. Dissolved Mn²⁺ concentrations in the studied pore
590 waters (0.55 μg/kg = 0.01 μmol/L; Table 6) are similar to those in the upper oxic zone in the
591 sediments east of the area of our studies (<0.1 μmol/L; Mewes et al., 2014) and much lower than
592 those in the suboxic zone in the same sediments (0.1 - 50 μmol/L; Mewes et al., 2014). This
593 means that the pore waters in the sediments from which the studied Mn-micronodules were
594 collected are currently oxic although depleted in O₂ in respect to the bottom seawater (Fig. 7).
595 The suboxic diagenetic origin of the Mn-micronodules may be explained with temporal
596 fluctuation of the oxic-suboxic front in the sediment. Volz et al. (2020) found that the
597 deoxygenation in the NE Pacific during the LGP resulted in compression of the oxic zone in the
598 sediments and precipitation of upward diffusing pore water Mn²⁺ in the upper 5 cm of the
599 sediment. The increasing [O₂] in the bottom seawater after the LGP has led to a deepening of the
600 oxic-suboxic front in the sediment (Volz et al., 2020). We may speculate that in the past
601 (presumably, during the LGP) the oxic-suboxic front in the studied sediments was close to the
602 seawater/sediment boundary. This might have resulted in suboxic reduction of both solid-phase
603 Mn⁴⁺ (and release of the trace elements adsorbed on it) and solid phases of the trace elements
604 (e.g., Ni, Cu, Mo, etc.) from the sediment, and the upward diffusion of the reduced species (e.g.,
605 Mn²⁺). Recent deepening of the oxic-suboxic front might have led to re-oxidation of Mn²⁺ back
606 to Mn⁴⁺ in the pore waters of the upper sediment layer (0-10 cm) and Mn-micronodule
607 precipitation.

608 The studied Mn-nodules are diagenetic-hydrogenetic formations according to the diagram
609 of Wegorzewski and Kuhn (2014) (Fig. 10A) whereas the diagram of Josso et al. (2017)

610 classifies them as diagenetic (Fig. 10B). The Mn-nodule standard Nod-A-1 (Atlantic Mn-nodule)
611 is hydrogenetic according to both the Wegorzewski and Kuhn (2014) (Fig. 10A) and Bonatti et
612 al. (1972) (not presented here) diagrams, but hydrogenetic-diagenetic according to the diagram of
613 Josso et al. (2017) (Fig. 10B). The later little deviation makes us assuming that the hydrogenetic
614 and diagenetic fields in the diagram of Josso et al. (2017) (Fig. 10B) need slight refinement. We
615 replaced the original name of the Diagenetic (oxic diagenesis) field (Josso et al., 2017) with
616 Diagenetic only (Fig. 10B) considering that the term oxic diagenesis is not correct (Wegorzewski
617 and Kuhn, 2014; Kuhn et al., 2017b). We have also replaced the metal-rich-hydrothermal trend
618 (Josso et al., 2017) with the more precise transition metal-rich hydrothermal (Fig. 10B). Thus, we
619 consider that the studied Mn-nodules are rather diagenetic-hydrogenetic than pure diagenetic
620 formations. Mn-nodule standard Nod-P-1 (Pacific Mn-nodule) plots close to our Mn-nodule
621 samples (Fig. 10A, B), which seems reasonable in view of the fact that Nod-P-1 Mn-nodules
622 were collected from the same Clarion-Clipperton zone (Flanagan and Gottfried, 1980) and close
623 to the area of collection of the studied Mn-nodules (Fig. 1). Therefore, we would classify the
624 Nod-P-1 as diagenetic-hydrogenetic Mn-nodules standard.

625 Both genetic parts of the Mn-nodules, hydrogenetic (upper) and diagenetic (lower), are
626 exposed in an oxic environment: dissolved oxygen concentrations of 177 $\mu\text{mol/L}$ and 118
627 $\mu\text{mol/L}$, respectively (Fig. 7). The diagenetic part of the Mn-nodules is enveloped in a dissolved
628 oxygen halo (~0.5 cm thick) within which $[\text{O}_2]$ sharply decreases from 118 to 52 $\mu\text{mol/L}$ (Fig. 7).
629 It seems likely that the dissolved elements in the sediment pore waters are essentially oxidized in
630 this oxygen halo and accreted to the Mn-nodules.

631 Chemistry of the individual layer growth structures (see 4.4 and Table 5) confirms the
632 genetic conclusions based on the bulk chemistry of the Mn-micronodules. Previous studies
633 (Wegorzewski and Kuhn, 2014) inferred that the layer type 2 growth structures within Mn-
634 nodules were suboxic-diagenetic precipitates. Our data (sub-section 4.4, Table 5, Fig. 10A)
635 clearly confirms that the layer type 2 (both sub-types 2a and 2b) growth structures are diagenetic
636 precipitates, which are a result of suboxic diagenesis. Although, the layer type 1 shows Mn/Fe
637 ratio up to 6 (Table 5) it might be considered as hydrogenetic growth structure according to the
638 previous work (Wegorzewski and Kuhn, 2014). The heterogeneity and porosity (on a fine scale)
639 of the material that composes these layers seem to be responsible for the slightly higher Mn/Fe
640 ratios and overall lower totals than those typical for the hydrogenetic precipitates (Wegorzewski

641 and Kuhn, 2014). Chemistry of the layer type 1 (sub-section 4.4, Table 5, Fig. 10A) growth
642 structures suggests that they are mixed diagenetic-hydrogenetic and pure hydrogenetic
643 precipitates. However, these growth structures are rare.

644

645 5.2.2. REE constraints

646 A recent study on the seafloor Fe-Mn-deposits proposed two diagrams for discrimination
647 among the genetic deposit types (Bau et al., 2014). The diagrams are based on the geochemical
648 relationships controlling the REE and Y. According to this discrimination approach the
649 hydrogenetic Fe-Mn-deposits are characterized by positive Ce anomaly ($Ce/Ce^* > 1$) and high Nd
650 concentrations (> 100 mg/kg). Thus, the USGS standard for Atlantic Mn-nodule (Nod-A-1)
651 appears to be a hydrogenetic deposit (Bau et al., 2014). Our REE data (Table 4; Fig. 6H) as well
652 as the ternary diagram approach (see sub-section 5.2.1) confirm that the Mn-nodule standard
653 Nod-A-1 is hydrogenetic. The USGS standard for Pacific Mn-nodule (Nod-P-1) seems to be
654 diagenetic-hydrogenetic (weak positive Ce anomaly, Nd ~ 100 mg/kg; Bau et al., 2014) and our
655 data are in good agreement with that (Table 4; Fig. 6G). Following the REE criteria of Bau et al.
656 (2014) our Mn-nodules are diagenetic-hydrogenetic deposits (weak positive or no Ce anomaly,
657 Nd > 100 mg/kg; Table 4, Figs 4A, C, E), which is supported by the ternary diagram approach (see
658 5.2.1).

659 Following our geochemical interpretations, the Mn-micronodules are diagenetic
660 precipitates, which are a result of suboxic diagenesis (see 5.2.1). According to the classification
661 of Bau et al. (2014) the diagenetic Mn-nodules should have Nd concentrations between 10 and
662 100 mg/kg, and negative (or no) Ce anomaly. The studied Mn-micronodules do have Nd = 10 –
663 100 mg/kg (Table 4), but they show positive Ce anomaly (Table 4; Fig. 6B, D, F), which is in
664 contradiction with the criteria of Bau et al. (2014). The positive Ce anomaly in the REE
665 distribution pattern of the Mn-micronodules can be explained following the interpretation of the
666 negative Ce anomaly in the diagenetic Mn-nodules by Bau et al. (2014). Mn-oxide particles
667 scattered in the sediment are primary precipitates in open seawater characterized by positive Ce
668 anomaly (Bau and Koschinsky, 2009). Bau et al. (2014) suppose that the suboxic diagenesis has
669 reduced and quantitatively re-mobilized Mn^{2+} and REE^{3+} , but not entire Ce^{4+} from the sediment
670 solid phases into pore waters. This has resulted in Mn-rich pore waters with deficiency of Ce.
671 This Ce deficit could not have been compensated by later preferential scavenging of Ce from the

672 pore waters during the diagenetic Mn-nodule growth and therefore, these nodules have negative
673 Ce anomaly (Bau et al., 2014). If we assume that during the suboxic diagenesis Ce^{4+} (seawater-
674 derived) in the sediment is reduced, quantitatively re-mobilized and then scavenged by the Mn-
675 micronodules from pore waters the diagenetically forming Mn-micronodules will acquire positive
676 Ce anomaly. We may speculate that because a major part of Ce^{3+} dissolved in pore waters has
677 been effectively sequestered by the Mn-micronodules dispersed within the sediment the
678 remaining pore fluid would have had Ce deficit, which will then be recorded in the big slowly
679 growing diagenetic Mn-nodules. The negative Ce anomaly detected in the pore waters (Table 6;
680 calculated relative to La and Nd instead of La and Pr because of lack of Pr concentration data)
681 may be interpreted from this point of view.

682 In other words, the model of Bau et al. (2014) is correct with the little detail we added here
683 about the intermediate role of the Mn-micronodules: suboxic quantitative re-mobilization of
684 seawater-derived Ce in the sediment and its sequestration by Mn-micronodules that leaves behind
685 pore water with Ce deficit, which feeds the diagenetic Mn-nodules.

686

687 *5.3. Source of elements to the Mn-micronodules*

688

689 The three patterns of vertical distribution of the elemental concentrations in the sediment
690 pore waters, (1) stable with no substantial fluctuations (Mn, Fe and probably P and Zn), (2)
691 upward decrease (Si, S, Mg, Ca, and Cr) and (3) upward increase (Na, K, Rb, Li, Mo, Cd, B, Ni,
692 V, Cu, Ba, Co, U, and Sr) (Fig. 7), are likely a result of differences in the redox remobilization
693 (dissolution) and immobilization (reprecipitation, scavenging) of the elements. The
694 remobilization and immobilization of elements in the pore waters depend on a number of
695 environmental controls: e.g., Eh, pH, T, ion activities, etc. These controls, excluding dissolved O_2
696 concentration (a measure for the Eh), were not investigated in the course of this study because
697 our focus was not on the pore waters, but on the Mn-micronodules. Therefore, the interpretation
698 of the pore water chemistry (the reasons for different behaviour of the elements in it) is beyond
699 the scope of this work. We can, in general, infer that the mild oxic conditions in the pore waters
700 ($[O_2] < 60 \mu\text{mol/L}$ below 1 cm depth; Fig. 7) may be responsible for the remobilization of some
701 elements (Na, K, Rb, Li, Mo, Cd, B, Ni, V, Cu, Ba, Co, U, and Sr) from the sediment and their
702 upward flux towards the seawater/sediment boundary.

703 We will comment on the pore waters in the studied sediment as possible source of elements
704 to both the bottom seawater and Mn-micronodules.

705 We have not studied the chemistry of the bottom seawater at the area of investigation and
706 therefore, we will use the chemical composition of the North Pacific deep seawater (see the
707 references in the figure caption to Figure 7) in our approach. Comparing the chemistry of the
708 North Pacific deep seawater with that of the studied pore waters (Fig. 7) we can suppose that
709 there is a diffusion flux of Mn, Fe, Si, Ca, Na, K, Rb, Li, Mo, Cd, Ni, V, Cu, Ba, Co, P, Zn, Cr,
710 and Sr dissolved in the pore waters towards the bottom seawater. I.e., the pore waters of the
711 studied sediments are a source of these elements to seawater. Concentrations of S and Mg in the
712 pore waters are close to those in the deep seawater (Fig. 7) which suggests that most probably
713 there is no flux of these elements either from the sediment to the seawater or from the seawater to
714 the sediment. Concentrations of U and B in the bottom seawater are higher than those in the pore
715 waters which means that the bottom seawater may be a source of these elements to the pore
716 waters.

717 Concentrations of Mn, Si, S, Mg, Na, Li, Mo, Cd, B, Ni, Cu, Ba, U, P, Zn, and Cr in the
718 Mn-micronodules co-vary with those in the pore waters (Fig. 7). This suggests that the pore
719 waters are likely source of these elements in the Mn-micronodules. It is challenging to explain
720 the reverse correlation of the concentrations of Fe, V, Co, Ca, Sr, K, and Rb in the Mn-
721 micronodules with those in the pore waters. It seems reasonable to assume that the concentrations
722 of Fe, V, Co, Sr, K, and Rb in the Mn-micronodules is a function of the micronodule age: the
723 older Mn-micronodules (deeper in the sediment) have had more time to scavenge higher amount
724 of elements than the younger Mn-micronodules (at the sediment surface) notwithstanding the
725 increased concentrations of these elements in the source pore waters towards the sediment
726 surface.

727

728 *5.4. Fe-Cu-Zn-isotope composition of Mn-micronodules*

729

730 Studied Mn-micronodules are suboxic diagenetic precipitations formed within the sediment
731 whereas their paired Mn-nodules are hydrogenetic-diagenetic formations formed at the sediment-
732 seawater boundary (see 5.2). A detailed study of the Mn-nodules from the same Clarion-
733 Clipperton zone showed they were composed of alternating diagenetic and hydrogenetic layers

734 (Wegorzewski and Kuhn, 2014). Hence, our bulk Mn-nodule samples likely average the
735 diagenetic and hydrogenetic influence on the nodule Fe-isotope composition.

736 Although the Fe-isotope composition of seawater ranges from -1.35 to +0.80‰ (Lacan et
737 al., 2008; Conway and John, 2014a; Chever et al., 2015; Fitzsimmons et al., 2016; Abadie et al.,
738 2017) the bottom seawater, which is directly responsible for the hydrogenetic precipitation of Fe
739 has $\delta^{56}\text{Fe} \sim 0.5\text{‰}$ (Horner et al., 2015; Fitzsimmons et al., 2016; Abadie et al., 2017). Can
740 hydrogenetic precipitation of Fe-oxyhydroxides from deep seawater ($\delta^{56}\text{Fe} \sim 0.5\text{‰}$) account for
741 the observed negative $\delta^{56}\text{Fe}$ of the Mn-micronodules and nodules (Fig. 8A; Table 7) if we
742 consider the identified Fe isotope fractionation during hydrogenetic precipitation of Fe? The
743 estimated Fe isotopic fractionation factor between pure hydrogenetic Fe-oxyhydroxide
744 precipitates (Fe-Mn crusts) and seawater is $\Delta^{56/54}\text{Fe}_{\text{FeMn-SW}} = \delta^{56/54}\text{Fe}_{\text{FeMn}} - \delta^{56/54}\text{Fe}_{\text{SW}} = -0.77\text{‰}$
745 (Horner et al., 2015). If we consider that the deep seawater responsible for hydrogenetic
746 precipitation of Fe-oxyhydroxides on the seafloor has mean $\delta^{56}\text{Fe}_{\text{SW}} = 0.5\text{‰}$ (Horner et al., 2015;
747 Fitzsimmons et al., 2016; Abadie et al., 2017) then, the hydrogenetic Fe-oxyhydroxide
748 precipitates on the seafloor will have $\delta^{56}\text{Fe} = -0.27\text{‰}$. This $\delta^{56}\text{Fe}$ is close to the Fe-isotope
749 composition of the studied Mn-micronodules and nodules (Table 7) and implies that the
750 hydrogenetic processes may have played a substantial role in their formation.

751 However, our mineralogical and geochemical studies suggest that the studied Mn-
752 micronodules have suboxic diagenetic genesis whereas the Mn-nodules are hydrogenetic-
753 diagenetic formations. Can the diagenetic processes in the sediment be major control on the Fe-
754 isotope composition of both the micronodules and nodules? It was found that the oxic clastic
755 sediments have $\delta^{56}\text{Fe} = 0.09\text{‰}$ (Beard and Johnson, 2004). The reduction of the sedimentary Fe
756 (presumably with $\delta^{56}\text{Fe} = 0.09\text{‰}$) fractionates Fe-isotopes and produces an isotopically light
757 dissolved Fe flux ($\delta^{56}\text{Fe} = -3.91\text{‰}$ to $+0.00\text{‰}$) that may further be transferred to the seawater
758 column (Johnson et al., 2002; Severmann et al., 2002; Welch et al., 2003; Severmann et al., 2010;
759 John et al., 2012; Klar et al., 2017). The precipitation of the Mn- micronodules and nodules from
760 the dissolved negative Fe isotope pool ($\delta^{56}\text{Fe} = -3.91\text{‰}$ to $+0.00\text{‰}$) in the sediment during
761 diagenetic processes or during hydrogenetic precipitation will result in negative $\delta^{56}\text{Fe}$ values of
762 both the Mn- micronodules and nodules (Fig. 8A; Table 7). This suggests that the diagenetic
763 processes may have important control on the Fe-isotope composition of the studied Mn-
764 micronodules and nodules. The slightly lighter Fe-isotope composition of the Mn-nodules (lying

765 on the sediment) than that of the paired Mn-micronodules (within the sediment) (Fig. 8A; Table
766 7) may also be explained with diagenetic processes: the pore waters near the sediment-seawater
767 boundary have Fe-isotope composition lighter than that of the deeper pore waters (Severmann et
768 al., 2010; Klar et al., 2017). The decrease of $\delta^{56}\text{Fe}$ of the Mn-micronodules from facies 0 upward
769 the sediment cores (towards the seawater-sediment interface) (Fig. 8A; Table 7) supports this
770 interpretation.

771 Overall, the Fe-isotope composition of the Mn- micronodules and nodules does not give an
772 unambiguous answer about their origin. It can equally be a result of either hydrogenetic or
773 diagenetic nature.

774 $\delta^{65}\text{Cu}$ of the studied Mn- micronodules and nodules, as well as that of the Mn-nodules and
775 Fe-Mn-crusts studied so far (Fig. 9B) is lower than that of the dissolved Cu in the deep (below
776 800 m) ocean [$+0.66 \pm 0.07\text{‰}$; Vance et al. (2008), Takano et al. (2014), Thompson and Ellwood
777 (2014), Moynier et al. (2017), Little et al. (2018)]. Lighter Cu-isotope composition of
778 hydrogenetic Fe-Mn-crusts [$\delta^{65}\text{Cu} = +0.12 - +0.58\text{‰}$; Little et al. (2014b)] and hydrogenetic-
779 diagenetic Mn-nodules [$\delta^{65}\text{Cu} = +0.05 - +0.60\text{‰}$; Albarède (2004)] than that of seawater is
780 consistent with preferential scavenging of ^{63}Cu and gradual accumulation of ^{65}Cu in seawater
781 (Albarède, 2004; Little et al., 2014a; Takano et al., 2014; Ijichi et al., 2018). Preferential
782 scavenging of ^{63}Cu from seawater [$\delta^{65}\text{Cu} = +0.66\text{‰}$; Vance et al. (2008)] on the Mn- and Fe-
783 oxyhydroxides explains the Cu-isotope composition of the studied hydrogenetic-diagenetic Mn-
784 nodules ($\delta^{65}\text{Cu} = +0.21 - +0.35\text{‰}$; Table 7). However, which are the processes leading to the
785 identical Cu-isotope composition of the truly diagenetic Mn-micronodules ($\delta^{65}\text{Cu} = +0.20 -$
786 $+0.35\text{‰}$; Table 7)? Obviously, the Mn-micronodules and the diagenetic layers in the Mn-nodules
787 have received their Cu from the dissolved Cu pool in the pore waters. Unfortunately, we are not
788 aware of any data for the Cu-isotope composition of the pore waters in marine sediments.
789 Therefore, our interpretations will be preliminary and speculative. The chemical composition of
790 the pore waters is mostly controlled by the interaction between the sediment particles and water:
791 dissolution/precipitation, adsorption/desorption, etc. Thus, the Cu-isotope composition of the
792 pore waters will broadly depend on the isotope composition of the sediment particles. Sediment
793 particles of the sediments are of two major types: detrital (lithogenic) and biogenic (organic
794 matter-related). Average lithogenic Cu isotope composition is $+0.08\text{‰}$ (Moynier et al., 2017),
795 whereas the organic matter-related (bioauthigenic) Cu in the sediments has $\delta^{65}\text{Cu} = +0.28\text{‰}$

796 (Little et al., 2017). If we assume that no Cu-isotope fractionation occurs upon dissolution or
797 desorption of any of these two sediment components, no binary mixing of dissolved both
798 lithogenic Cu (+0.08‰) and bioauthigenic Cu (+0.28‰) (in any proportions) can explain the Cu-
799 isotope composition of the micronodules (+0.20 – +0.35‰) keeping in mind that scavenging of
800 Cu_{aq} on the Mn-Fe-oxyhydroxides will drive the source $\delta^{65}\text{Cu}$ to lower values (preferentially
801 retaining lighter ^{63}Cu). Thus, the Cu_{aq} released from the sediment particles to the pore waters
802 needs to be heavier than Cu in the source particles. In fact, it was found that abiotic oxidation of
803 Cu^+ -containing minerals releases isotopically heavier $\text{Cu}_{\text{aq}}^{2+}$ than the source mineral (e.g., Mathur
804 et al., 2005). This will provide the heavy Cu ($\delta^{65}\text{Cu} > +0.28‰$) necessary for the Cu-isotope
805 composition (+0.20 – +0.35‰) of the diagenetic Mn-micronodules. The slight decrease of $\delta^{65}\text{Cu}$
806 of the Mn-micronodules upward the sediment cores (Table 7) seems to be a result of the
807 progressive depletion of the heavy diagenetic upward flux in ^{63}Cu . This would mean that the
808 benthic Cu flux from the sediment to bottom seawater must be heavy. Indeed, Takano et al.
809 (2014) reported values of the Cu-isotope composition of the benthic input ($\delta^{65}\text{Cu} = +0.58‰$)
810 close to that of the deep seawater ($\delta^{65}\text{Cu} = +0.66‰$).

811 It is known that the speciation of Cu dissolved in seawater is organically controlled (Coale
812 and Bruland, 1988; Moffett and Dupont, 2007). The major part of Cu dissolved in the pore waters
813 of costal marine sediments is as organic complexes and a very small fraction of it is as inorganic
814 species (Skrabal et al., 2000). The organic complexation of Cu was found to be associated with
815 Cu isotope fractionation: Cu-binding ligands preferentially complex the heavy Cu isotope
816 (Pokrovsky et al, 2008; Bigalke et al., 2010b; Navarrete et al., 2011; Ryan et al., 2014; Sherman,
817 2013; Sherman et al., 2015; Sherman and Little, 2020). We are not aware of any investigation of
818 Cu isotope fractionation in the pore waters of abyssal plain sediments, but in view of the previous
819 studies we may suppose that Cu organic complexation plays an essential role in the Cu isotope
820 fractionation in the pore waters and eventually, in the Cu isotope composition of the Mn-
821 micronodules.

822 It was found (Little et al., 2014b) that the Zn-isotope composition of the Fe-Mn-crusts
823 [hydrogenetic deposits; $\delta^{66}\text{Zn}_{\text{JMC}} = +0.80 - +1.23‰$ (Little et al., 2014b)] and Mn-nodules
824 [hydrogenetic and hydrogenetic-diagenetic deposits; $\delta^{66}\text{Zn}_{\text{JMC}} = +0.53 - +1.16‰$ (Maréchal et
825 al., 2000)] is heavier than that of the seawater [$\delta^{66}\text{Zn}_{\text{JMC}} = +0.46 - +0.51‰$; Little et al. (2014b),
826 Lemaitre et al. (2020)]. Zn-isotope composition of the studied Mn-micronodules ($\delta^{66}\text{Zn}_{\text{JMC}} =$

827 +0.61 – +0.90‰; Table 7) and Mn-nodules ($\delta^{66}\text{Zn}_{\text{JMC}} = +0.75 – +0.87‰$; Table 7) is also heavier
828 than that of the seawater. Little et al. (2014b) explain the heavier Zn-isotope composition of the
829 hydrogenetic Fe-Mn-deposits relative to that of seawater with equilibrium isotope partitioning
830 between dissolved and adsorbed Zn when Zn_{aq} is either free or inorganically-specified. In such a
831 case the heavy ^{66}Zn adsorbs more readily than the light ^{64}Zn due to preferential sorption of heavy
832 Zn isotopes on Fe-Mn-oxyhydroxides surfaces (e.g., Bryan et al., 2015). This mechanism
833 explains the Zn-isotope composition of the studied hydrogenetic-diagenetic Mn-nodules.

834 Diagenetic Mn-micronodules receive their Zn content from the pore waters. Therefore, the
835 Zn-isotope composition of the Mn-micronodules seems to be controlled by the processes of Zn
836 isotope fractionation in the pore water (in the sediment). Conway and John (2014b) found that the
837 continental margin sediments are a source of isotopically light Zn ($\delta^{66}\text{Zn}_{\text{JMC}} = -0.5 – -0.8‰$) to
838 the ocean. The light Zn isotope flux is supposed to be released from degrading phytoplankton
839 material [with light Zn-isotope composition; e.g., Kobberich et al. (2019)] within the sediments.
840 Although the studied Mn- micronodules and nodules are within and on top, respectively, of
841 abyssal plain sediments we can suppose that in a similar way (e.g., Conway and John, 2014b) the
842 decay of the buried organic matter in the sediment releases light Zn and creates a light Zn isotope
843 pool ($\delta^{66}\text{Zn}_{\text{JMC}} < 0‰$) in the pore waters. Substantial Zn isotope fractionation is necessary in the
844 pore water (with presumably $\delta^{66}\text{Zn}_{\text{JMC}} < 0‰$) in order to reach the Zn-isotope composition of the
845 Mn-micronodules ($\delta^{66}\text{Zn}_{\text{JMC}} = +0.61 – +0.90‰$). We may speculate again that if the dissolved
846 Zn_{aq} in the pore waters is either free or inorganically-specified then, the heavy ^{66}Zn will be
847 adsorbed preferentially on the Mn-Fe-oxyhydroxides than the light ^{64}Zn (e.g., Bryan et al., 2015).
848 This will result in heavy Zn-isotope composition of the Mn-micronodules and diagenetic layers
849 of the Mn-nodules.

850 Major part of the Zn dissolved in seawater (up to 98%) is also (like Cu) complexed to
851 organic ligands (Wells et al., 1998; Bruland, 1999; John et al., 2007). The organic complexation
852 of Zn also results in Zn isotope fractionation: heavy Zn isotope enrichment of the organic
853 complexes (Jouvin et al., 2009; Markovic et al., 2017). We do not know of any study on the Zn
854 isotope fractionation in marine sediment pore waters, but are challenged to speculate that the
855 organic complexation of Zn might play an important role in the Zn isotope fractionation in
856 sediment pore waters and Zn isotope composition of the Mn-micronodules.

857 Fe-Cu-Zn-isotope composition of the Mn-nodule standard Nod-P-1 (Pacific Mn-nodule)
858 (Table 7) agrees well with that measured previously [$\delta^{56}\text{Fe} = -0.51 \pm 0.09\text{‰}$ (Marcus et al.,
859 2015); $\delta^{65}\text{Cu} = 0.35 - 0.46 (\pm 0.05 - 0.08)\text{‰}$ (Jochum et al., 2005; Chapman et al., 2006; Pontér
860 et al., 2021); $\delta^{66}\text{Zn} = 0.63 - 0.87 (\pm 0.02 - 0.09)\text{‰}$ (Chapman et al., 2006; Bigalke et al., 2010a;
861 Gagnevin et al., 2012; Chen et al., 2016; Druce et al., 2020)] and falls within the range of the
862 isotope composition of the studied Mn-nodules (Fig. 9A, B, C) confirming the same
863 hydrogenetic-diagenetic nature of the studied and standard nodules. However, its Fe- and Zn-
864 isotope compositions are lighter than that of the Mn-nodule standard Nod-A-1 (Atlantic Mn-
865 nodule) [$\delta^{56}\text{Fe} = -0.42 - -0.37 (\pm 0.06 - 0.08)\text{‰}$ (Dideriksen et al., 2006; Ellwood et al., 2015;
866 Marcus et al., 2015); $\delta^{66}\text{Zn} = 0.96 - 1.01 (\pm 0.01 - 0.03)\text{‰}$ (Chen et al., 2016; Druce et al.,
867 2020)] whereas its Cu-isotope composition does not differ (within the uncertainty) from that of
868 the Nod-A-1 standard [$\delta^{65}\text{Cu} = 0.42 \pm 0.07\text{‰}$ (Pontér et al., 2021)]. These differences and
869 similarity in the Fe-Cu-Zn-isotope composition of the hydrogenetic-diagenetic (Nod-P-1) and
870 hydrogenetic (Nod-A-1) Mn-nodules are challenging to be investigated, but not straightforward
871 to be explained and fall beyond the scope of this work.

872

873 *5.5. Can Mn-micronodules be potential resource for valuable elements?*

874

875 Mn-micronodules are ubiquitous in marine sediments from almost all seafloor settings:
876 from mid-ocean ridges to abyssal deeps excluding the continental margins. Combining their wide
877 global occurrence with narrow stratigraphic distribution [they are mostly concentrated in the
878 uppermost ~1 m of the sediment cover (Sval'nov et al., 1991a; Pattan, 1993; Chauhan and Rao,
879 1999; Dubinin and Sval'nov, 2000b)] and easy extraction (magnetic or electro-magnetic) from
880 the loose sediment makes them possible attractive resource for valuable chemical elements.

881 In order to estimate the potential of Mn-micronodules as a resource for valuable elements
882 we made a compilation of all chemistry data we are aware of (Table 8). We have not included in
883 this data set some of the old data with unclear analytical approach (we could not estimate the
884 quality of the data) as well as the data received with both electron microprobe and laser ablation
885 ICP-MS (these two approaches give the chemical composition at single points and are not
886 representative for the Mn-micronodules as a whole). The compilation (Table 8) shows that the
887 chemical data for Mn-micronodules are scarce. Most of the works report the concentrations of

888 Mn, Fe, some transition metals (Cu, Ni, Co) and REE only. Very few works give the
889 concentrations of wide spectrum of elements. With such a poor data base it is not possible to give
890 a meaningful estimation of the resource potential of the Mn-micronodules in global aspect
891 [locally, Yasukawa et al. (2020) estimated it for the area of the Minamitorishima Island, Pacific
892 Ocean]. In order to get a rough idea about the economic potential of the Mn-micronodules we
893 have compared their chemistry with that of their big and fairly well studied counterparts, Mn-
894 nodules (Table 8).

895 Although the concentrations of different elements are variable in the Mn-micronodules
896 from different settings we can see that they, in general, are poorer in most elements than the Mn-
897 nodules (e.g., twice poorer in REE) (Table 8). Manganese, Ni, Cu, Zn, and Mo appear to be the
898 main elements of potential economic interest that are in the Mn-micronodules in concentrations
899 higher than those in the Mn-nodules. In a future more precise estimation of the economic
900 potential of the Mn-micronodules (more studies are necessary) these elements have to receive
901 particular attention.

902

903 **6. Summary**

904

905 Mn-micronodules in the sediments of the Clarion-Clipperton zone in the Pacific Ocean are
906 composed of 10 Å and 7 Å phyllo-manganates, and vernadite (δ -MnO₂). Their internal structure
907 shows fine concentric growth layers, which have varying chemistry and reflectivity. According to
908 that three different layer growth structures were distinguished: (1) layer type 1 with low Mn/Fe
909 ratio (2.6 – 6), low Ni+Cu content (1.11 – 1.88 wt.%), high Co content (0.14 - 0.5 wt.%), and low
910 reflectivity; (2) layer type 2a with high Mn/Fe ratio (34 - 699), high Ni+Cu content (1.44 - 5.45
911 wt.%), low Co content (<0.07 wt.%), and high reflectivity; (3) layer type 2b with medium Mn/Fe
912 ratio (8 - 95), medium to high Ni+Cu content (1.93 - 4.17 wt.%), high Co content (up to 0.5
913 wt.%), and low reflectivity.

914 Interpreting the chemistry of the studied Mn-micronodules and Mn-nodules (Fe, Mn, Ni,
915 Cu, HFSE and REE concentrations) we inferred that: (1) the Mn-micronodules are diagenetic
916 precipitates, which are a result of suboxic diagenesis; and (2) the Mn-nodules are diagenetic-
917 hydrogenetic formations. Fine scale investigations revealed that the most common growth
918 structures (layer type 2) within the Mn-micronodules are suboxic-diagenetic, whereas the rare

919 growth structures (layer type 1) are mixed diagenetic-hydrogenetic and hydrogenetic precipitates.
920 However, the current redox state of the pore waters in the sediments where the Mn-micronodules
921 have formed is oxic (although approaching suboxic values). Thus, the suboxic diagenetic origin
922 of the Mn-micronodules may be explained with temporal fluctuation of the oxic-suboxic front in
923 the sediment. We assume that during the LGP the oxic-suboxic front in the sediments had been
924 close to the seawater/sediment boundary. This might have resulted in suboxic reduction of solid-
925 phase Mn⁴⁺ and other elements in the sediment and the upward diffusion of the reduced species.
926 Recent deepening of the oxic-suboxic front might have led to re-oxidation of Mn²⁺ in the pore
927 waters of the upper sediment layer and Mn-micronodule precipitation.

928 The positive Ce anomaly and Nd content (10 - 100 mg/kg) of the Mn-micronodules
929 contradict the REE criteria for diagenetic Mn-oxide deposition according to the previous
930 research. We explain these features with suboxic quantitative re-mobilization of seawater-derived
931 Ce in the sediment and its sequestration by Mn-micronodules that results in Ce-deficient pore
932 water. This Ce deficiency is recorded in the diagenetic Mn-nodules.

933 The pore waters of the studied sediments are the most probable source of Mn, Si, S, Mg,
934 Na, Li, Mo, Cd, B, Ni, Cu, Ba, U, P, Zn, and Cr in the Mn-micronodules. They are also a source
935 of Mn, Fe, Si, Ca, Na, K, Rb, Li, Mo, Cd, Ni, V, Cu, Ba, Co, P, Zn, Cr, and Sr to the bottom
936 seawater. The bottom seawater in turn is a source of U and B to the pore waters.

937 Investigation of the Fe-Cu-Zn isotope composition of the Mn-micronodules and Mn-
938 nodules provided additional information on the geochemical processes occurring in the sediment
939 and leading to micronodule and nodule precipitation. The measured Fe-isotope composition of
940 the Mn- micronodules and nodules can be explained by either hydrogenetic or diagenetic
941 precipitation of the Fe-oxyhydroxide component. However, relying on the inferred suboxic
942 diagenetic origin of the Mn-micronodules (based on our mineralogical and geochemical studies)
943 we would suggest rather a major diagenetic than hydrogenetic control on their Fe-isotope
944 composition following: (1) reduction of the sedimentary Fe ($\delta^{56}\text{Fe} = 0.09\text{‰}$), (2) fractionation of
945 Fe-isotopes leading to an isotopically light ($\delta^{56}\text{Fe} = -3.91\text{‰}$ to $+0.00\text{‰}$) dissolved Fe pool in the
946 sediment (and flux to the seawater column), followed by (3) Fe-oxyhydroxide precipitation with
947 preferential uptake of ⁵⁶Fe leading to (still) light Fe isotope composition of both the Mn-
948 micronodules and diagenetic layers of the Mn-nodules ($\delta^{56}\text{Fe} = -0.63$ to -0.27‰). Lighter Fe

949 isotopes of the Mn-nodules (-0.63‰ - -0.39‰) than that of the Mn-micronodules (-0.43‰ - -
950 0.27‰) supports the influence of the diagenetic processes on the fractionation of Fe isotopes.

951 Preferential scavenging of the light ^{63}Cu from seawater ($\delta^{65}\text{Cu} = +0.66\text{‰}$) on the Mn- and
952 Fe-oxyhydroxides accounts for the Cu-isotope composition of the studied hydrogenetic-
953 diagenetic Mn-nodules ($\delta^{65}\text{Cu} = +0.21 - +0.35\text{‰}$) lighter than that of seawater ($\delta^{65}\text{Cu} = 0.7 -$
954 0.9‰). The diagenetic Mn-micronodules have Cu-isotope composition ($\delta^{65}\text{Cu} = +0.20 -$
955 $+0.35\text{‰}$) identical to that of the hydrogenetic-diagenetic Mn-nodules. The oxidative dissolution
956 of the sedimentary components ($\delta^{65}\text{Cu} = +0.08 - +0.28\text{‰}$) releases isotopically heavy $\text{Cu}_{\text{aq}}^{2+}$
957 ($\delta^{65}\text{Cu} > +0.28\text{‰}$) in the pore waters. This diagenetic Cu-isotope pool is subsequently recorded
958 in the diagenetic Mn-micronodules (considering preferential scavenging of the light ^{63}Cu) and
959 appears to be similar to that of the hydrogenetic Cu-isotope pool (bottom seawater).

960 The heavier Zn-isotope composition of the studied hydrogenetic-diagenetic Mn-nodules
961 ($\delta^{66}\text{Zn}_{\text{JMC}} = +0.75 - +0.87\text{‰}$) relative to that of the seawater ($\delta^{66}\text{Zn}_{\text{JMC}} = +0.46 - +0.51\text{‰}$) is
962 interpreted to be a result of equilibrium isotope partitioning between dissolved and adsorbed Zn
963 when Zn_{aq} is either free or inorganically-specified. In such a case, the heavy ^{66}Zn adsorbs more
964 readily than the light ^{64}Zn due to preferential sorption of heavy Zn isotopes on Fe-Mn-
965 oxyhydroxides surfaces. Preferential adsorption of ^{66}Zn from the light Zn isotope pool ($\delta^{66}\text{Zn}_{\text{JMC}}$
966 $< 0\text{‰}$) of the pore waters (Zn_{aq} is either free or inorganically-specified) on the Mn-Fe-
967 oxyhydroxides has resulted in heavy Zn-isotope composition of the Mn-micronodules ($\delta^{66}\text{Zn}_{\text{JMC}}$
968 $= +0.61 - +0.90\text{‰}$) and diagenetic layers of the Mn-nodules.

969 In general, the chemical data for Mn-micronodules are scarce and it is not possible to give a
970 meaningful estimation of their resource potential with such a limited database. The Mn-
971 micronodules are poorer in most elements than the Mn-nodules and only Mn, Ni, Cu, Zn, and Mo
972 are in concentrations higher than those in the Mn-nodules.

973

974 **Acknowledgements**

975

976 The captain and crew of the R/V *L'Atalante* are thanked for their efforts to support the sampling and onboard
977 sample treatment. Sincere thanks go to: M. Ranneberg for supporting the XRD analyses, M. Hein for the IR
978 determinations, and D. Henry (all from BGR) for preparation of the polished block section. This research was
979 supported by a LabexMER Axis 3 (Geobiological interactions in extreme environments; Institut Universitaire
980 Européen de la Mer, Université de Bretagne Occidentale) grant (project NODESIS) to V. M. Dekov.

- 981
982
983 **References**
984
985 Abadie, C., Lacan, F., Radic, A., Pradoux, C., Poitrasson, F., 2017. Iron isotopes reveal distinct dissolved iron
986 sources and pathways in the intermediate versus deep Southern Ocean. *PNAS* 114, 858-863.
987 Addy, S.K., 1978. Distribution of Fe, Mn, Cu, Ni and Co in coexisting manganese nodules and micronodules. *Mar.*
988 *Geol.* 28, M9-M17.
989 Addy, S.K., 1979. Rare earth element patterns in manganese nodules and micronodules from northwest Atlantic.
990 *Geochim. Cosmochim. Acta* 43, 1105-1115.
991 Albarède, F., 2004. The stable isotope geochemistry of copper and zinc. *Rev. Mineral. Geochem.* 55, 409-427.
992 Alibo, D.S., Nozaki, Y., 1999. Rare earth elements in seawater: particle association, shale-normalization, and Ce
993 oxidation. *Geochim. Cosmochim. Acta* 63, 363-372.
994 Archer, C., Andersen, M.B., Cloquet, C., Conway, T.M., Dong, S., Ellwood, M., Moore, R., Nelson, J., Rehkämper,
995 M., Rouxel, O., Samanta, M., Shin, K.-C., Sohrin, Y., Takano, S., Wasylenki, L., 2017. Inter-calibration of a
996 proposed new primary reference standard AA-ETH Zn for zinc isotopic analysis. *J. Anal. At. Spectrom.* 32,
997 415-419.
998 Atkins, A.L., Shaw, S., Peacock, C.L., 2014. Nucleation and growth of todorokite from birnessite: Implications for
999 trace-metal cycling in marine sediments. *Geochim. Cosmochim. Acta* 144, 109-125.
1000 Axelsson, M.D., Rodushkin, I., Ingri, J., Öhlander, B., 2002. Multielemental analysis of Mn-Fe nodules by ICP-MS:
1001 optimisation of analytical method. *Analyst* 127, 76-82.
1002 Banerjee, R., Iyer, S.D., 1991. Biogenic influence on the growth of ferromanganese micronodules in the Central
1003 Indian Basin. *Marine Geology* 97, 413-421.
1004 Bau, M., Koschinsky, A., 2009. Oxidative scavenging of cerium on hydrous Fe oxide: evidence from the
1005 distribution of rare earth elements and yttrium between Fe oxides and Mn oxides in hydrogenetic
1006 ferromanganese crusts. *Geochem. J.* 43, 37-47.
1007 Bau, M., Schmidt, K., Koschinsky, A., Hein, J., Kuhn, T., Usui, A., 2014. Discriminating between different genetic
1008 types of marine ferro-manganese crusts and nodules based on rare earth elements and yttrium. *Chemical*
1009 *Geology* 381, 1-9.
1010 Beard, B.L., Johnson, C.M., 1999. High precision iron isotope measurements of terrestrial and lunar materials.
1011 *Geochimica et Cosmochimica Acta* 63, 1653-1660.
1012 Beard, B.L., Johnson, C.M., 2004. Fe isotope variations in the modern and ancient Earth and other planetary bodies.
1013 *Rev. Mineral. Geochem.* 55, 319-357.
1014 Beard, B.L., Johnson, C.M., Von Damm, K.L., Poulson, R.L., 2003. Iron isotope constraints on Fe cycling and mass
1015 balance in the oxygenated Earth oceans. *Geology* 31, 629-632.
1016 Bigalke, M., Weyer, S., Kobza, J., Wilcke, W., 2010a. Stable Cu and Zn isotope ratios as tracers of sources and
1017 transport of Cu and Zn in contaminated soil. *Geochimica et Cosmochimica Acta* 74, 6801-6813.

- 1018 Bigalke, M., Weyer, S., Wilcke, W., 2010b. Copper isotope fractionation during complexation with insolubilized
1019 humic acid. *Environ. Sci. Technol.* 44, 5496-5502.
- 1020 Bodeř, S., Manceau, A., Geoffroy, N., Baronnet, A., Buatier, M., 2007. Formation of todorokite from vernadite in
1021 Ni-rich hemipelagic sediments. *Geochimica et Cosmochimica Acta* 71, 5698-5716.
- 1022 Bonatti, E., Kraemer, T., Rydell, H., 1972. Classification and genesis of submarine iron manganese deposits. In:
1023 Horn, D.R. (Ed.), *Ferromanganese Deposits on the Ocean Floor*. Lamont-Doherty Geological Observatory of
1024 Columbia University, Palisades, N.Y., pp. 147-166.
- 1025 Bruland, K.W., 1980. Oceanographic distributions of cadmium, zinc, nickel and copper in the North Pacific. *Earth*
1026 *Planet. Sci. Lett.* 47, 176-198.
- 1027 Bruland, K.W., 1999. Complexation of zinc by natural organic ligands in the central North Pacific. *Limnol.*
1028 *Oceanogr.* 34, 269-285.
- 1029 Bryan, A.L., Dong, S., Wilkes, E.B., Wasylenki, L.E., 2015. Zinc isotope fractionation during adsorption onto Mn
1030 oxyhydroxide at low and high ionic strength. *Geochimica et Cosmochimica Acta* 157, 182-197.
- 1031 Chan, L.H., Edmond, J.M., Stallard, R.F., Broecker, W.S., Chung, Y.C., Weiss, R.F., Ku, T.L., 1976. Radium and
1032 barium at GEOSECS stations in the Atlantic and Pacific. *Earth Planet. Sci. Lett.* 32, 258-267.
- 1033 Chapman, J.B., Mason, T.F.D., Weiss, D.J., Coles, B.J., Wilkinson, J.J., 2006. Chemical separation and isotopic
1034 variations of Cu and Zn from five geological reference materials. *Geostandards and Geoanalytical Research*
1035 30, 5-16.
- 1036 Chauhan, O.S., Rao, Ch.M., 1999. Influence of sedimentation on enrichment of manganese and growth of
1037 ferromanganese micronodules, Bengal Fan, India. *Marine Geology* 161, 39-47.
- 1038 Chen, H., Savage, P.S., Teng, F.-Z., Helz, R.T., Moynier, F., 2013. Zinc isotope fractionation during magmatic
1039 differentiation and the isotopic composition of the bulk Earth. *Earth Planet. Sci. Lett.* 369-370, 34-42.
- 1040 Chen, J.H., Edwards, R.L., Wasserburg, G.J., 1986. ^{238}U , ^{234}U and ^{232}Th in seawater. *Earth Planet. Sci. Lett.* 80, 241-
1041 251.
- 1042 Chen, S., Liu, Y., Hu, J., Zhang, Z., Hou, Z., Huang, F., Yu, H., 2016. Zinc isotopic compositions of NIST SRM
1043 683 and whole-rock reference materials. *Geostandards and Geoanalytical Research* 40, 417-432.
- 1044 Chester, R., Hughes, M.J., 1967. A chemical technique for the separation of ferro-manganese minerals, carbonate
1045 minerals and adsorbed trace elements from pelagic sediments. *Chemical Geology* 2, 249-262.
- 1046 Chever, F., Rouxel, O.J., Croot, P.L., Ponzevera, E., Wuttig, K., Auro, M., 2015. Total dissolvable and dissolved
1047 iron isotopes in the water column of the Peru upwelling regime. *Geochim. Cosmochim. Acta* 162, 66-82.
- 1048 Chu, N.-C., Johnson, C.M., Beard, B.L., German, C.R., Nesbitt, R.W., Usui, A., 2003. Secular Fe isotope variations
1049 in the central Pacific Ocean. *Geochim. Cosmochim. Acta* 67, A66.
- 1050 Coale, K.H., Bruland, K.W., 1988. Copper complexation in the northeast Pacific. *Limnol. Oceanogr.* 33, 1084-1101.
- 1051 Collier, R.W., 1984. Particulate and dissolved vanadium in the North Pacific Ocean. *Nature* 309, 441-444.
- 1052 Conway, T.M., John, S.G., 2014a. Quantification of dissolved iron sources to the North Atlantic Ocean. *Nature* 511,
1053 212-215.
- 1054 Conway, T.M., John, S.G., 2014b. The biogeochemical cycling of zinc and zinc isotopes in the North Atlantic
1055 Ocean. *Global Biogeochem. Cycles* 28, 1111-1128.

- 1056 Dauphas, N., John, S.G., Rouxel, O., 2017. Iron isotope systematic. *Reviews in Mineralogy and Geochemistry* 82,
1057 276-371.
- 1058 Dekov, V.M., Marchig, V., Rajta, I., Uzonyi, I., 2003. Fe-Mn micronodules born in the metalliferous sediments of
1059 two spreading centers: East Pacific Rise and Mid-Atlantic Ridge. *Marine Geology* 199, 101-121.
- 1060 de Villiers, S., 1998. Excess dissolved Ca in the deep ocean: a hydrothermal hypothesis. *Earth Planet. Sci. Lett.* 164,
1061 627-641.
- 1062 de Villiers, S., 1999. Seawater strontium and Sr/Ca variability in the Atlantic and Pacific Oceans. *Earth Planet. Sci.*
1063 *Lett.* 171, 623-634.
- 1064 Dideriksen, K., Baker, J.A., Stipp, S.L.S., 2006. Iron isotopes in natural carbonate minerals determined by MC-ICP-
1065 MS with a Fe-58-Fe-54 double spike. *Geochimica et Cosmochimica Acta* 70, 118-132.
- 1066 Druce, M., Stirling, C.H., Rolison, J.M., 2020. High-precision zinc isotopic measurement of certified reference
1067 materials relevant to the environmental, earth, planetary and biomedical sciences. *Geostandards and*
1068 *Geoanalytical Research* 44, 711-732.
- 1069 Dubinin, A.V., Sval'nov, V.N., 1995. Micronodules from Guatemala Basin: Geochemistry of rare earth elements.
1070 *Lithology and Mineral Resources* 5, 473-479. (in Russian).
- 1071 Dubinin, A.V., Sval'nov, V.N., 1996. Differentiated mobility of iron oxyhydroxides during the processes of
1072 formation of micro- and macronodules (Guatemala Basin, Pacific Ocean). *Doklady Academy of Sciences*
1073 348, 100-103. (in Russian).
- 1074 Dubinin, A.V., Sval'nov, V.N., 2000a. Geochemistry of rare earth elements in micro- and macronodules from the
1075 Pacific bioproductive zone. *Lithology and Mineral Resources* 35, 1, 19-31.
- 1076 Dubinin, A.V., Sval'nov, V.N., 2000b. Geochemistry of rare earth elements in ferromanganese micro- and
1077 macronodules from the Pacific nonproductive zone. *Lithology and Mineral Resources* 35, 6, 520-537.
- 1078 Dubinin, A.V., Sval'nov, V.N., 2003. Geochemistry of the manganese ore process in the ocean: Evidence from rare
1079 earth elements. *Lithology and Mineral Resources* 38, 2, 91-100.
- 1080 Dubinin, A.V., Sval'nov, V.N., Uspenskaya, T.Yu., 2008. Geochemistry of the authigenic ferromanganese ore
1081 formation in sediments of the Northeast Pacific Basin. *Lithology and Mineral Resources* 43, 2, 99-110.
- 1082 Dubinin, A.V., Sval'nov, V.N., Berezhnaya, E.D., Rimsкая-Korsakova, M.N., Demidova, T.P., 2013.
1083 Geochemistry of trace and minor elements in sediments and manganese micronodules from the Angola
1084 Basin. *Lithology and Mineral Resources* 48, 3, 175-197.
- 1085 Dubinin, A.V., Rimsкая-Korsakova, M.N., Demidova, T.P., 2020. Anomalies of rare elements in manganese
1086 micronodules from *Ethmodiscus* oozes in the Brazil Basin of the Atlantic Ocean. *Bulletin of Kamchatka*
1087 *regional association "Educational - scientific center"*, *Earth sciences* 48, 64-84. (in Russian).
- 1088 Ellwood, M.J., Hutchins, D.A., Lohan, M.C., Milne, A., Nasemann, P., Nodder, S.D., Sander, S.G., Strzepek, R.,
1089 Wilhelm, S.W., Boyd, P.W., 2015. Iron stable isotopes track pelagic iron cycling during a subtropical
1090 phytoplankton bloom. *PNAS* 112, E15-E20.
- 1091 Fitzsimmons, J.N., Conway, T.M., Lee, J.-M., Kayser, R., Thyng, K.M., John, S.G., Boyle, E.A., 2016. Dissolved
1092 iron and iron isotopes in the southeastern Pacific Ocean. *Global Biogeochem. Cycles* 30, 1372-1395.

1093 Flanagan, F.J., Gottfried, D., 1980. USGS Rock Standards, III: Manganese-Nodule Reference Samples USGS-Nod-
1094 A-1 and USGS-Nod-P-1. Geological Survey Professional Paper 1155, 46 p.

1095 Gagnevin, D., Boyce, A.J., Barrie, C.D., Menuge, J.F., Blakeman, R.J., 2012. Zn, Fe and S isotope fractionation in a
1096 large hydrothermal system. *Geochimica et Cosmochimica Acta* 88, 183-198.

1097 Golden, D.C., Dixon, J.B., Chen, C.C., 1986. Ion exchange, thermal transformations, and oxidizing properties of
1098 birnessite Clays *Clay Miner.* 34, 511-520.

1099 Halbach, P., Friedrich, G., Von Stackelberg, U. (Eds), 1988. The Manganese Nodule Belt of the Pacific Ocean.
1100 Geological Environment, Nodule Formation, and Mining Aspects. Ferdinand Enke Verlag, Stuttgart, 254 pp.

1101 Heath, G.R., 1981. Ferromanganese nodules of the deep sea. *Econ. Geol.* 75th Anniv. Vol., 736-765.

1102 Hein, J.R., Koschinsky, A., 2014. Deep-ocean ferromanganese crusts and nodules. In: Holland, H.D., Turekian,
1103 K.K. (Eds), *Treatise on Geochemistry*, 2nd edition, Elsevier, Amsterdam, 13, 273-291.

1104 Hishida, H., Uchio, T., 1981. Sedimentological and geochemical studies of manganese micronodules and the
1105 associated sediments in some piston cores in the North Pacific Ocean. *Jour. Fac. Eng., Univ. Tokyo, ser. B*,
1106 36, 463-522.

1107 Horner, T.J., Williams, H.M., Hein, J.R., Saito, M.A., Burton, K.W., Halliday, A.N., Nielsen, S.G., 2015.
1108 Persistence of deeply sourced iron in the Pacific Ocean. *PNAS* 112, 1292-1297.

1109 Ijichi, Y., Ohno, T., Sakata, S., 2018. Copper isotopic fractionation during adsorption on manganese oxide: Effects
1110 of pH and desorption. *Geochemical Journal* 52, e1-e6.

1111 Immel, R.L., 1974. Origin of micromanganese nodules determined from uranium-234/uranium-238 ratios. *Antarctic*
1112 *journal of the United States* 9, 259-260.

1113 Immel, R., Osmond, J.K., 1976. Micromanganese nodules in deep-sea sediments: Uranium-isotopic evidence for
1114 post-depositional origin. *Chemical Geology* 18, 263-272.

1115 Ito, T., Komuro, K., Hatsuya, K., Nishi, H., 2005. Chemical compositions of ferromanganese micronodules in
1116 sediments at Site 1216, ODP Leg 199, Paleogene equatorial transect. In: Wilson, P.A., Lyle, M. and Firth,
1117 J.V. (Eds.), *Proc. ODP, Sci. Results*, 199, 1-20.

1118 Jeandel, C., Minster, J.F., 1987. Chromium behavior in the ocean: global versus regional processes. *Global*
1119 *Biogeochem. Cycles* 1, 131-154.

1120 Jochum, K.P., Nohl, U., Herwig, K., Lammel, E., Stoll, B., Hofmann, A.W., 2005. GeoReM: A new geochemical
1121 database for reference materials and isotopic standards. *Geostand. Geoanalyt. Res.* 29, 333-338.

1122 John, S.G., Geis, R., Saito, M., Boyle, E.A., 2007. Zn isotope fractionation during high-affinity zinc transport by the
1123 marine diatom *Thalassiosira oceanica*. *Limnol. Oceanogr.* 52, 2710-2714.

1124 John, S.G., Mendez, J., Moffett, J., Adkins, J., 2012. The flux of iron and iron isotopes from San Pedro Basin
1125 sediments. *Geochim. Cosmochim. Acta* 93, 14-29.

1126 Johnson, C.M., Skulan, J.L., Beard, B.L., Sun, H., Neelson, K.H., Braterman, P.S., 2002. Isotopic fractionation
1127 between Fe(III) and Fe(II) in aqueous solutions. *Earth Planet. Sci. Lett.* 195, 141-153.

1128 Josso, P., Pelleter, E., Pourret, O., Fouquet, Y., Etoubleau, J., Cheron, S., Bollinger, C., 2017. A new discrimination
1129 scheme for oceanic ferromanganese deposits using high field strength and rare earth elements. *Ore Geology*
1130 *Reviews* 87, 3-15.

- 1131 Jouvin, D., Louvat, P., Juillot, F., Maréchal, C.N., Benedetti, M.F., 2009. Zinc isotopic fractionation: why organic
1132 matters. *Environ. Sci. Technol.* 43, 5747-5754.
- 1133 Julien, C.M., Massot, M., Poinsignon, C., 2004. Lattice vibrations of manganese oxides: Part I. Periodic structures.
1134 *Spectrochim. Acta A: Mol. Biomol. Spectrosc.* 60, 689-700.
- 1135 Kang, L., Zhang, M., Liu, Z.H., Ooi, K., 2007. IR spectra of manganese oxides with either layered or tunnel
1136 structures. *Spectrochim. Acta A: Mol. Biomol. Spectrosc.* 67, 864-869.
- 1137 Kato, Y., Fujinaga, K., Nakamura, K., Takaya, Y., Kitamura, K., Ohta, J., Toda, R., Nakashima, T., Iwamori, H.,
1138 2011. Deep-sea mud in the Pacific Ocean as a potential resource for rare-earth elements. *Nat. Geosci.* 4, 535-
1139 539.
- 1140 Kidd, R.B., Ármannson, H., 1979. Manganese and iron micronodules from a volcanic seamount in the Tyrrhenian
1141 Sea. *Jl geol. Soc. Lond.* 136, 71-76.
- 1142 Klar, J.K., Homoky, W.B., Statham, P.J., Birchill, A.J., Harris, E.L., Woodward, E.M.S., Silburn, B., Cooper, M.J.,
1143 James, R.H., Connelly, D.P., Chever, F., Lichtschlag, A., Graves, C., 2017. Stability of dissolved and soluble
1144 Fe(II) in shelf sediment pore waters and release to an oxic water column. *Biogeochemistry* 135, 49-67.
- 1145 Köbberich, M., Vance, D., 2019. Zn isotope fractionation during uptake into marine phytoplankton: Implications for
1146 oceanic zinc isotopes. *Chem. Geol.* 523, 154-161.
- 1147 Kuhn, T., Versteegh, G.J.M., Villinger, H., Dohrmann, I., Heller, C., Koschinsky, A., Kaul, N., Ritter, S.,
1148 Wegorzewski, A.V., Kasten, S., 2017a. Widespread seawater circulation in 18-22 Ma oceanic crust: Impact
1149 on heat flow and sediment geochemistry. *Geology* 45, 799-802.
- 1150 Kuhn, T., Wegorzewski, A., Rühlemann, C., Vink, A., 2017b. Composition, formation, and occurrence of
1151 polymetallic nodules. In: Sharma, R. (Ed.), *Deep-Sea Mining: Resource Potential, Technical and
1152 Environmental Considerations*, Springer International Publishing AG, 23-63.
- 1153 Kunzendorf, H., Gwozdz, R., Glasby, G.P., Stoffers, P., Renner, R.M., 1989. The distribution of rare earth elements
1154 in manganese micronodules and sediments from the equatorial and southwest Pacific. *Applied Geochemistry*
1155 4, 183-193.
- 1156 Kunzendorf, H., Glasby, G.P., Stoffers, P., Plüger, W.L., 1993. The distribution of rare earth and minor elements in
1157 manganese nodules, micronodules and sediments along an east-west transect in the southern Pacific. *Lithos*
1158 30, 45-56.
- 1159 Lacan, F., Radic, A., Jeandel, C., Poitrasson, F., Sarthou, G., Pradoux, C., Freydier, R., 2008. Measurement of the
1160 isotopic composition of dissolved iron in the open ocean. *Geophys. Res. Lett.* 35, L24610.
- 1161 Lallier-Verges, E., Clinard, C., 1983. Ultra-thin section study of the mineralogy and geochemistry of Mn
1162 micronodules from the South Pacific. *Marine Geology* 52, 267-280.
- 1163 Landing, W.M., Bruland, K.W., 1980. Manganese in the North Pacific. *Earth Planet. Sci. Lett.* 49, 45-56.
- 1164 Lemaitre, N., de Souza, G.F., Archer, C., Wang, R-M., Planquette, H., Sarthou, G., Vance, D., 2020. Pervasive
1165 sources of isotopically light zinc in the North Atlantic Ocean. *Earth and Planetary Science Letters* 539,
1166 116216.
- 1167 Le Suavé, R., 1989. Campagne NIXO 47: Etude detaillée de deux sites de ramassage de nodules polymétalliques.
1168 Colloque Tour du Monde du Jean Charcot. Paris, 2-3 Mars 1989, pp. 249-256.

- 1169 Levasseur, S., Frank, M., Hein, J.R., Halliday, A.N., 2004. The global variation in the iron isotope composition of
1170 marine hydrogenetic ferromanganese deposits: implications for seawater chemistry? *Earth and Planetary*
1171 *Science Letters* 224, 91-105.
- 1172 Li, D., Fu, Y., Liu, Q., Reinfelder, J.R., Hollings, P., Sun, X., Tan, C., Dong, Y., Ma, W., 2020. High-resolution LA-
1173 ICP-MS mapping of deep-sea polymetallic micronodules and its implications on element mobility.
1174 *Gondwana Research* 81, 461-474.
- 1175 Liao, J., Sun, X., Wu, Z., Sa, R., Guan, Y., Lu, Y., Li, D., Liu, Y., Deng, Y., Pan, Y., 2019. Fe-Mn (oxyhydr)oxides
1176 as an indicator of REY enrichment in deep-sea sediments from the central North Pacific. *Ore Geology*
1177 *Reviews* 112, 103044.
- 1178 Little, S.H., Sherman, D.M., Vance, D., Hein, J.R., 2014a. Molecular controls on Cu and Zn isotopic fractionation in
1179 Fe-Mn crusts. *Earth and Planetary Science Letters* 396, 213-222.
- 1180 Little, S.H., Vance, D., Walker-Brown, C., Landing, W.M., 2014b. The oceanic mass balance of copper and zinc
1181 isotopes, investigated by analysis of their inputs, and outputs to ferromanganese oxide sediments. *Geochim.*
1182 *Cosmochim. Acta* 125, 673-693.
- 1183 Little, S.H., Vance, D., McManus, J., Severmann, S., Lyons, T.W., 2017. Copper isotope signatures in modern
1184 marine sediments. *Geochim. Cosmochim. Acta* 212, 253-273.
- 1185 Little, S.H., Archer, C., Milne, A., Schlosser, C., Achterberg, E.P., Lohan, M.C., Vance, D., 2018. Paired dissolved
1186 and particulate phase Cu isotope distributions in the South Atlantic. *Chem. Geol.* 502, 29-43.
- 1187 Marcus, M.A., Edwards, K.J., Gueguen, B., Fakra, S.C., Horn, G., Jelinski, N.A., Rouxel, O., Sorensen, J., Toner,
1188 B.M., 2015. Iron mineral structure, reactivity, and isotopic composition in a South Pacific Gyre
1189 ferromanganese nodule over 4 Ma. *Geochimica et Cosmochimica Acta* 171, 61-79.
- 1190 Marechal, C.N., Telouk, P., Albarede, F., 1999. Precise analysis of copper and zinc isotopic compositions by
1191 plasma-source mass spectrometry. *Chemical Geology* 156, 251-273.
- 1192 Maréchal, C., Nicolas, E., Douchet, C., Albarède, F., 2000. Abundance of zinc isotopes as a marine biogeochemical
1193 tracer. *Geochem. Geophys. Geosyst.* 1, 1015-15.
- 1194 Markovic, T., Manzoor, S., Humphreys-Williams, E., Kirk, G., Vilar, R., Weiss, D., 2017. Experimental
1195 determination of zinc isotope fractionation in complexes with the phytosiderophore 2'-deoxymugenic acid
1196 (DMA) and its structural analogues, and implications for plant uptake mechanisms. *Environmental Science*
1197 *and Technology* 51, 98-107.
- 1198 Martin, J.H., Gordon, R.M., Fitzwater, S., Broenkow, W.W., 1989. VERTEX: phytoplankton/iron studies in the
1199 Gulf of Alaska. *Deep-Sea Res.* 36, 649-680.
- 1200 Mathur, R., Ruiz, J., Titley, S., Liermann, L., Buss, H., Brantley, S., 2005. Cu isotopic fractionation in the supergene
1201 environment with and without bacteria. *Geochim. Cosmochim. Acta* 69, 5233-5246.
- 1202 McLennan, S.M., 1989. Rare earth elements in sedimentary rocks: Influence of provenance and sedimentary
1203 processes. In: B.R. Lipin and G.A. McKay (Eds), *Geochemistry and Mineralogy of Rare Earth Elements*,
1204 *Rev. Miner.* 21, 169-200.
- 1205 Menendez, A., James, R.H., Roberts, S., Peel, K., Connelly, D., 2017. Controls on the distribution of rare earth
1206 elements in deep-sea sediments in the North Atlantic Ocean. *Ore Geol. Rev.* 87, 100-113.

1207 Mewes, K., Mogollón, J.M., Picard, A., Rühlemann, C., Kuhn, T., Nöthen, K., Kasten, S., 2014. Impact of
1208 depositional and biogeochemical processes on small scale variations in nodule abundance in the
1209 Clarion-Clipperton Fracture Zone. *Deep-Sea Research I* 91, 125-141.

1210 Mewes, K., Mogollón, J.M., Picard, A., Rühlemann, C., Eisenhauer, A., Kuhn, T., Ziebis, W., Kasten, S., 2016.
1211 Diffusive transfer of oxygen from seamount basaltic crust into overlying sediments: An example from the
1212 Clarion-Clipperton Fracture Zone. *Earth and Planetary Science Letters* 433, 215-225.

1213 Millero, F., 1974. Seawater as a multicomponent electrolyte solution. In: Goldberg, E. (Ed.), *The Sea*, 5, Wiley, pp.
1214 3-80.

1215 Moffett, J.W., Dupont, C., 2007. Cu complexation by organic ligands in the sub-Arctic NW Pacific and Bering Sea.
1216 *Deep-Sea Res., Part 1* 54, 586-595.

1217 Morel, Y., Le Suavé, R., 1986. Variabilité de l'environnement morphologique et sédimentaire dans un secteur
1218 intraplaque du Pacifique Nord (zone Clarion-Clipperton). *Bull. Soc. Géol. France II*, 361-372.

1219 Moynier, F., Vance, D., Fujii, T., Savage, P., 2017. The isotope geochemistry of zinc and copper. *Rev. Mineral.
1220 Geochem.* 82, 543-600.

1221 Mukhopadhyay, S., Dasgupta, S., Roy, S., 1988. Distribution and character of micronodules in pelagic sediments
1222 from Central Indian Basin, Indian ocean and their implications. *Marine Mining* 7, 351- 358.

1223 Navarrete, J.U., Borrok, D.M., Viveros, M., Ellzey, J.T., 2011. Copper isotope fractionation during surface
1224 adsorption and intracellular incorporation by bacteria. *Geochim. Cosmochim. Acta* 75, 784-799.

1225 Ohashi, M., 1985. Depositional environments and chemical compositions of manganese micronodules. *J. Geol. Soc.
1226 Japan* 91, 787-803.

1227 Pattan, J.N., 1993. Manganese micronodules: A possible indicator of sedimentary environments. *Marine Geology*
1228 113, 331-344.

1229 Pattan, J.N., Colley, S., Higgs, N.C., 1994. Behavior of rare earth elements in coexisting manganese macronodules,
1230 micronodules, and sediments from the Central Indian Basin. *Marine Georesources and Geotechnology* 12,
1231 283-295.

1232 Pokrovsky, O.S., Viers, J., Emnova, E.E., Kompantseva, E.I., Freydier, R., 2008. Copper isotope fractionation
1233 during its interaction with soil and aquatic microorganisms and metal oxy(hydr)oxides: possible structural
1234 control. *Geochim. Cosmochim. Acta* 72, 1742-1757.

1235 Pontér, S., Sutliff-Johansson, S., Engström, E., Widerlund, A., Mäki, A., Rodushkina, K., Paulukat, C., Rodushkin,
1236 I., 2021. Evaluation of a multi-isotope approach as a complement to concentration data within environmental
1237 forensics. *Minerals* 11, 37.

1238 Poppe, L.J., Commeau, R.F., Commeau, J.A., Manheim, F.T., Aruscavage, P.J., 1984. Ferromanganese
1239 micronodules from the surficial sediments of Georges Bank. *Journal of Marine Research* 42, 463-472.

1240 Potter, R.M., Rossman, G.R., 1979. The tetravalent manganese oxides: identification, hydration, and structural
1241 relationships by infrared spectroscopy. *Am. Mineral.* 64, I199-I1218.

1242 Rouxel, O.J., Bekker, A., Edwards, K.J., 2005. Iron Isotope Constraints on the Archean and Paleoproterozoic Ocean
1243 Redox State. *Science* 307, 1088-1091.

- 1244 Ryan, B.M., Kirby, J.K., Degryse, F., Scheiderich, K., McLaughlin, M.J., 2014. Copper isotope fractionation during
1245 equilibration with natural and synthetic ligands. *Environ. Sci. Technol.* 48, 8620-8626.
- 1246 Seeberg-Elverfeldt, J., Schlüter, M., Feseker, T., Kölling, M., 2005. Rhizon sampling of porewaters near the
1247 sediment-water interface of aquatic systems. *Limnology and Oceanography: Methods* 3, 361-371.
- 1248 Severmann, S., Larsen, O., Palmer, M.R., Nüster, J., 2002. The isotopic signature of Fe-mineralization during early
1249 diagenesis. *Geochim. Cosmochim. Acta* 66, A698.
- 1250 Severmann, S., Johnson, C.M., Beard, B.L., German, C.R., Edmonds, H.N., Chiba, H., Green, D.R.H., 2004. The
1251 effect of plume processes on the Fe isotope composition of hydrothermally derived Fe in the deep ocean as
1252 inferred from the Rainbow vent site, Mid-Atlantic Ridge, 36°14'N. *Earth Planet. Sci. Lett.* 225, 63-76.
- 1253 Severmann, S., McManus, J., Berelson, W.M., Hammond, D.E., 2010. The continental shelf benthic iron flux and its
1254 isotope composition. *Geochim. Cosmochim. Acta* 74, 3984-4004.
- 1255 Sherman, D.M., 2013. Equilibrium isotopic fractionation of copper during oxidation/reduction, aqueous
1256 complexation and ore-forming processes: predictions from hybrid density functional theory. *Geochim.*
1257 *Cosmochim. Acta* 118, 85-97.
- 1258 Sherman, D.M., Little, S.H., 2020. Isotopic disequilibrium of Cu in marine ferromanganese crusts: Evidence from
1259 ab initio predictions of Cu isotope fractionation on sorption to birnessite. *Earth and Planetary Science Letters*
1260 549, 116540.
- 1261 Skrabal, S.A., Donat, J.R., Burdige, D.J., 2000. Pore water distributions of dissolved copper and copper-complexing
1262 ligands in estuarine and coastal marine sediments. *Geochim. Cosmochim. Acta* 64, 1843-1857.
- 1263 Sohrin, Y., Isshiki, K., Kuwamoto, T., 1987. Tungsten in North Pacific waters. *Mar. Chem.* 22, 95-103.
- 1264 Spencer, D.W., Robertson, D.E., Turekian, K.K., Folsom, T.R., 1970. Trace element calibrations and profiles at the
1265 Geosecs test station in the Northeast Pacific Ocean. *J. Geophys. Res.* 75, 7688.
- 1266 Stoffers, P., Glasby, G.P., Thijssen, T., Srivastava, P., Meguen, M., 1981. The geochemistry of coexisting
1267 manganese nodules, micromnodules, sediments and pore waters from five areas in the equatorial and southwest
1268 Pacific. *Chem. Erde* 40, 273-297.
- 1269 Stoffers, P., Glasby, G.P., Frenzel, G., 1984. Comparison of the characteristics of manganese micromnodules from the
1270 equatorial and south-west Pacific. *Tschermaks Mineralogische und Petrographische Mitteilungen* 33, 1-23.
- 1271 Stoffyn-Egli, P., MacKenzie, F.T., 1984. Mass balance of dissolved lithium in the oceans. *Geochim. Cosmochim.*
1272 *Acta* 48, 859-872.
- 1273 Sugisaki, R., Ohashi, M., Sugitani, K., Suzuki, K., 1987. Compositional variations in manganese micromnodules: A
1274 possible indicator of sedimentary environments. *The Journal of Geology* 95, 433-454.
- 1275 Sugitani, K., 1987. A geochemical study of hydrothermal manganese micromnodules from marine sediments and
1276 sedimentary rocks on land. *J. Geol. Soc. Japan* 93, 555-574.
- 1277 Sval'nov, V.N., Lyapin, A.B., Novikova, Z.T., 1991a. Manganese micromnodules. Report 1. General characteristics
1278 and distribution in pelagic sediments. *Lithology and Mineral Resources* 3, 3-20. (in Russian).
- 1279 Sval'nov, V.N., Lyapin, A.B., Novikova, Z.T., 1991b. Manganese micromnodules. Report 2. Composition and origin.
1280 *Lithology and Mineral Resources* 4, 32-50. (in Russian).

1281 Takano, S., Tanimizu, M., Hirata, T., Sohrin, Y., 2014. Isotopic constraints on biogeochemical cycling of copper in
1282 the ocean. *Nat. Commun.* 5, 5663.

1283 Thompson, C.M., Ellwood, M.J., 2014. Dissolved copper isotope biogeochemistry in the Tasman Sea, SW Pacific
1284 Ocean. *Mar. Chem.* 165, 1-9.

1285 Tostevin, R., Poulton, S., 2019. Suboxic sediments. In: Gargaud, M., Irvine, W.M., Amils, R., Cleaves, H.J., Pinti,
1286 D., Cernicharo Quintanilla, J., Viso, M., (Eds), *Encyclopedia of Astrobiology*. Springer, Berlin, Heidelberg, 4
1287 p.

1288 Uppstrom, L.R., 1974. The boron/chlorinity ratio of deep-sea water from the Pacific Ocean. *Deep-Sea Res.* 21, 161-
1289 162.

1290 Vance, D., Archer, C., Bermin, J., Perkins, J., Statham, P.J., Lohan, M.C., Ellwood, M.J., Mills, R.A., 2008. The
1291 copper isotope geochemistry of rivers and the oceans. *Earth and Planetary Science Letters* 274, 204-213.

1292 Veillette, J., Juniper, S.K., Gooday, A.J., Sarrazin, J., 2007. Influence of surface texture and microhabitat
1293 heterogeneity in structuring nodule faunal communities. *Deep-Sea Research I* 54, 1936-1943.

1294 Volz, J.B., Mogollón, J.M., Geibert, W., Arbizu, P.M., Koschinsky, A., Kasten, S., 2018. Natural spatial variability
1295 of depositional conditions, biogeochemical processes and element fluxes in sediments of the eastern Clarion-
1296 Clipperton Zone, Pacific Ocean. *Deep-Sea Research Part I* 140, 159-172.

1297 Volz, J.B., Liu, B., Köster, M., Henkel, S., Koschinsky, A., Kasten, S., 2020. Post-depositional manganese
1298 mobilization during the last glacial period in sediments of the eastern Clarion-Clipperton Zone, Pacific Ocean.
1299 *Earth and Planetary Science Letters* 532, 116012.

1300 Wegorzewski, A.V., Kuhn, T., 2014. The influence of suboxic diagenesis on the formation of manganese nodules in
1301 the Clarion Clipperton nodule belt of the Pacific Ocean. *Marine Geology* 357, 123-138.

1302 Wegorzewski, A.V., Kuhn, T., Dohrmann, R., Wirth, R., Grangeon, S., 2015. Mineralogical characterization of
1303 individual growth structures of Mn-nodules with different Ni+Cu content from the central Pacific Ocean.
1304 *American Mineralogist* 100, 2497-2508.

1305 Wegorzewski, A.V., Grangeon, S., Webb, S.M., Heller, C., Kuhn, T., 2020. Mineralogical transformations in
1306 polymetallic nodules and the change of Ni, Cu and Co crystal-chemistry upon burial in sediments.
1307 *Geochimica et Cosmochimica Acta* 282, 19-37.

1308 Welch, S.A., Beard, B.L., Johnson, C.M., Braterman, P.S., 2003. Kinetic and equilibrium Fe isotope fractionation
1309 between aqueous Fe(II) and Fe(III). *Geochim. Cosmochim. Acta* 67, 4231-4250.

1310 Wells, M.L., Kozelka, P.B., Bruland, K.W., 1998. The complexation of “dissolved” Cu, Zn, Cd and Pb by soluble
1311 and colloidal organic matter in Narragansett Bay, RI. *Mar. Chem.* 62, 203-217.

1312 Williams, H.M., Bizimis, M., 2014. Iron isotope tracing of mantle heterogeneity within the source regions of oceanic
1313 basalts. *Earth and Planetary Science Letters* 404, 396-407.

1314 Winter, B.L., Johnson, C.M., Clark, D.L., 1997. Geochemical constraints on the formation of Late Cenozoic
1315 ferromanganese micronodules from the central Arctic Ocean. *Marine Geology* 138, 149-169.

1316 Xu, H., Peng, X., Ta, K., Song, T., Du, M., Li, J., Chen, S., Qu, Z., 2020. Structure and composition of micro-
1317 manganese nodules in deep-sea carbonate from the Zhaoshu Plateau, north of the South China Sea. *Minerals*
1318 10, 1016.

1319 Yasukawa, K., Ohta, J., Miyazaki, T., Vaglarov, B.S., Chang, Q., Ueki, K., Toyama, C., Kimura, J.-I., Tanaka, E.,
1320 Nakamura, K., Fujinaga, K., Iijima, K., Iwamori, H., Kato, Y., 2019. Statistic and isotopic characterization of
1321 deep-sea sediments in the Western North Pacific Ocean: Implications for genesis of the sediment extremely
1322 enriched in rare earth elements. *Geochemistry, Geophysics, Geosystems* 20, 10.1029/2019GC008214.

1323 Yasukawa, K., Kino, S., Azami, K., Tanaka, E., Mimura, K., Ohta, J., Fujinaga, K., Nakamura, K., Kato, Y., 2020.
1324 Geochemical features of Fe-Mn micronodules in deep-sea sediments of the western North Pacific Ocean:
1325 Potential for co-product metal extraction from REY-rich mud. *Ore Geology Reviews* 127, 103805.

1326 Yasukawa, K., Kino, S., Ohta, J., Azami, K., Tanaka, E., Mimura, K., Fujinaga, K., Nakamura, K., Kato, Y., 2021.
1327 Stratigraphic variations of Fe-Mn micronodules and implications for the formation of extremely REY-rich
1328 mud in the western North Pacific Ocean. *Minerals* 11, 270.

1329 Zhu, X.K., O’Nions, R.K., Guo, Y., Reynolds, B.C., 2000. Secular variation of iron isotopes in north Atlantic Deep
1330 Water. *Science* 287, 2000-2002.

1331

Figure captions

- 1332
1333
1334 **Fig. 1.** Bathymetric map of the studied area with distribution of the Mn-nodule facies and location of the studied
1335 sediment cores. Inset map shows the location of the studied area (red rectangle) in the Pacific Ocean.
1336
1337 **Fig. 2.** Photographs of the Mn-nodule facies at the seafloor (taken by *DSV Nautila*) and corresponding Mn-nodules
1338 (insets). (A) facies 0 and a Mn-nodule from facies 0 (spherical; sample NODKGS51 0-5cm); (B) facies A and a Mn-
1339 nodule from facies A (spherical; sample EBS07); (C) facies B and a Mn-nodule from facies B (flat, upper surface;
1340 sample NODKGS53 0-7 cm); (D) facies C and a Mn-nodule from facies C (flat, ellipsoidal, upper surface; sample
1341 NODKGS63 0-5cm).
1342
1343 **Fig. 3.** SEM photomicrographs of: (A) elongated botryoidal Mn-micronodules (SEI; sample NODKGS58 0-5cm);
1344 (B) isometric Mn-micronodule (SEI; sample NODKGS58 0-5cm); (C, D, E, F) cross sections of Mn-micronodules
1345 showing their internal structure and layer types (BEI; sample NODKGS63 0-5 cm).
1346
1347 **Fig. 4.** XRD patterns of two selected Mn-micronodule samples after drying at 30°C (black patterns) and after heating
1348 at 105°C for 24h (red patterns). [a.u.] = arbitrary units; Fsp = feldspar; Qz = quartz.
1349
1350 **Fig. 5.** IR spectra of five selected Mn-micronodule samples compared with the IR spectra of a phylломanganate-rich
1351 Mn-nodule and a todorokite-rich Mn-nodule from Wegorzewski et al. (2020). The black arrows mark the IR bands
1352 that are characteristic for Mn-oxides: phylломanganate ($400 - 515 \text{ cm}^{-1}$) and todorokite ($\sim 760 \text{ cm}^{-1}$). Quartz (Qz) and
1353 other minor impurities ($1200 - 900 \text{ cm}^{-1}$) were detected.
1354
1355 **Fig. 6.** NASC-normalized (McLennan, 1989) REE distribution patterns of Mn-nodules and Mn-micronodules from
1356 facies 0 (A and B, respectively), B (C and D, respectively) and C (E and F, respectively), and of Pacific (Nod-P-1)
1357 and Atlantic (Nod-A-1) Mn-nodule standards (G and H, respectively) and North Pacific Deep Water [$\times 15000000$;
1358 Alibo and Nozaki (1999)] (G).
1359
1360 **Fig. 7.** Vertical distributions of the elemental concentrations in the pore waters along the sediment cores
1361 NODKGS63 (O_2 ; black closed circles = profile close to a Mn-nodule, red closed squares = profile beneath the Mn-
1362 nodule) and NODKGS65 (the other elements; black closed circles). Blue stars, elemental concentrations in the North
1363 Pacific deep seawater: O_2 , our data; Mn from Landing and Bruland (1980); Fe, and Co from Martin et al. (1989); S,
1364 Mg, Na, and K from Millero (1974); Ca from de Villiers (1998); Rb from Spencer et al. (1970); Li from Stoffyn-Egli
1365 and MacKenzie (1984); Mo from Sohrin et al. (1987); Cd, Ni, Cu, and Zn from Bruland (1980); B from Uppstrom
1366 (1974); V from Collier (1984); Ba from Chan et al. (1976); U from Chen et al. (1986); Cr from Jeandel and Minster
1367 (1987); Sr from de Villiers (1999). Concentrations of the same elements in the Mn-micronodules collected from the

1368 same core (NODKGS65) are shown on the same plots with red vertical bars covering the sediment layers from which
1369 the Mn-micronodules were extracted (0-5 cm and 5-10 cm). Concentration scales are given in red on top of each plot.

1370
1371 **Fig. 8.** Fe-Cu-Zn isotope composition of Mn-micronodules and Mn-nodules from this study. (A) Fe-isotope
1372 composition; (B) Cu-isotope composition; (C) Zn-isotope composition. Colored dots represent the isotope
1373 composition of the Mn-nodules laying at the sediment surface, and colored vertical bars show the isotope
1374 composition of the Mn-micronodules for the depth range where they were collected (i.e., 0-5 cm depth and 5-10 cm
1375 depth, except for NODKGS53, 0-7 cm depth).

1376
1377 **Fig. 9.** Fe-Cu-Zn-isotope composition (range) of seafloor Fe-Mn-oxyhydroxide deposits. (A) Fe-isotope composition
1378 of Fe-Mn-crusts (Zhu et al., 2000; Chu et al., 2003; Levasseur et al., 2004; Horner et al., 2015) and Mn-nodules
1379 (Beard and Johnson, 1999; Levasseur et al., 2004; Marcus et al., 2015); (B) Cu-isotope composition of Fe-Mn-crusts
1380 (Little et al., 2014b) and Mn-nodules (Albarède, 2004); (C) Zn-isotope composition of Fe-Mn-crusts (Little et al.,
1381 2014b) and Mn-nodules (Maréchal et al., 2000). Isotope composition of terrestrial igneous rocks: $\delta^{56}\text{Fe}$ (Beard and
1382 Johnson, 2004), $\delta^{65}\text{Cu}$ (Albarède, 2004), and $\delta^{66}\text{Zn}$ (Albarède, 2004). For data of this study see Table 7. Red crosses
1383 = isotope composition of Mn-nodule standard Nod-P-1.

1384
1385 **Fig. 10.** Ternary discriminative diagrams for genetic classification of the seafloor Fe–Mn-oxyhydroxide deposits and
1386 positions of the studied Mn-micronodules and Mn-nodules: (A) Fe-Mn-(Ni+Cu)*10 diagram according to
1387 Wegorzewski and Kuhn (2014) (based on Halbach et al., 1988) showing the geochemical relationships between the
1388 diagenetic (A), diagenetic-hydrogenetic (AB) and hydrogenetic (B) nodule types; (B) diagram of Josso et al. (2017)
1389 with some refinement.

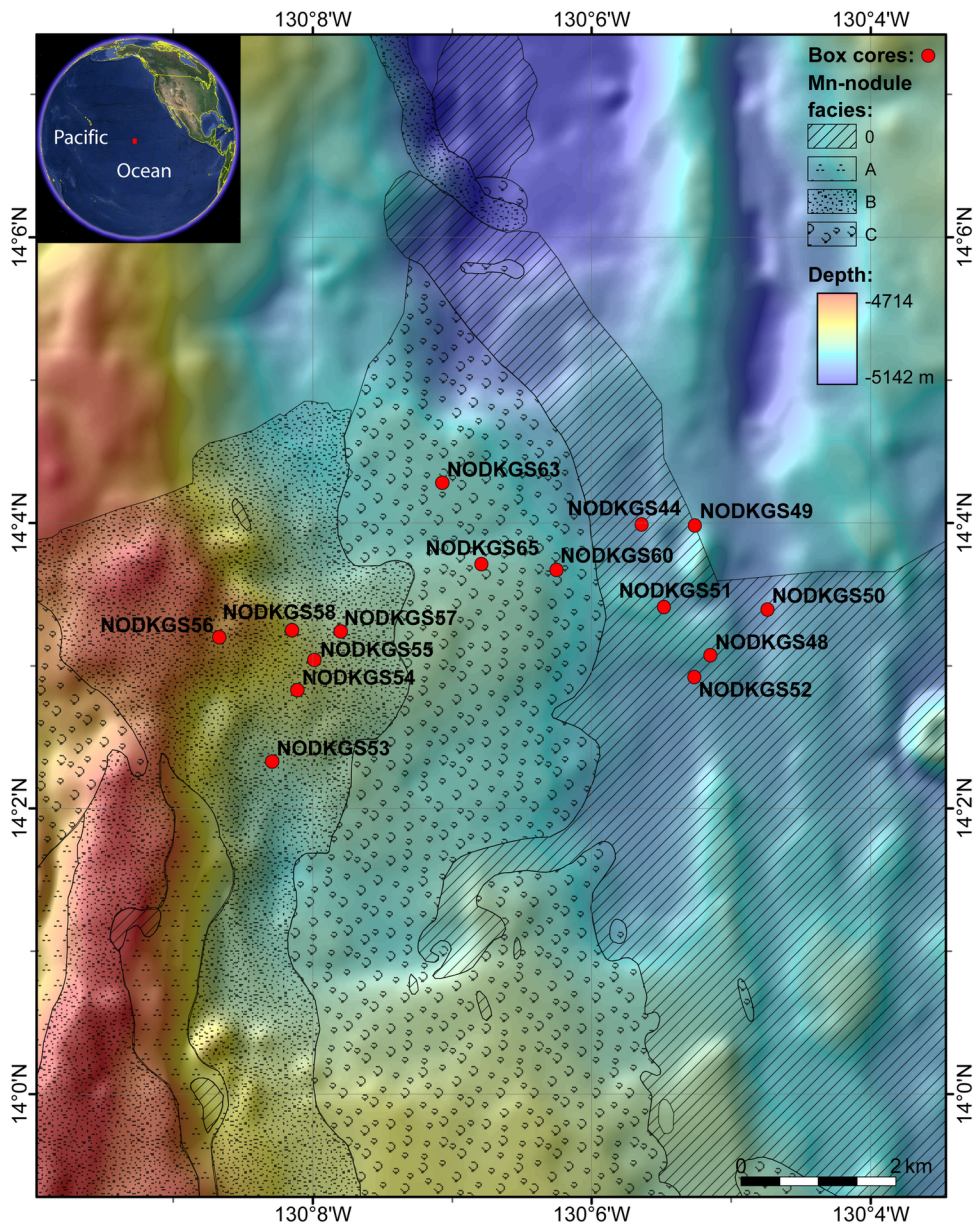
1390
1391

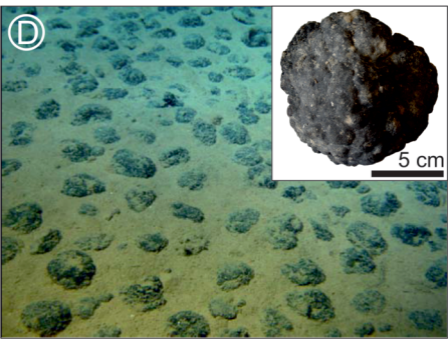
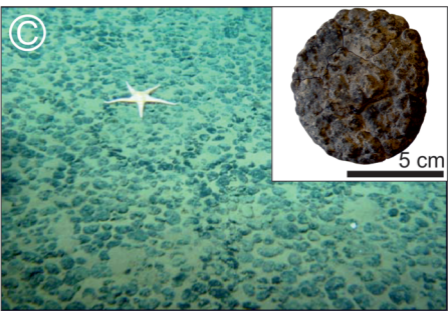
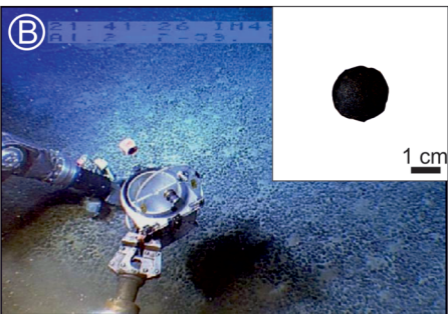
1392 Appendixes

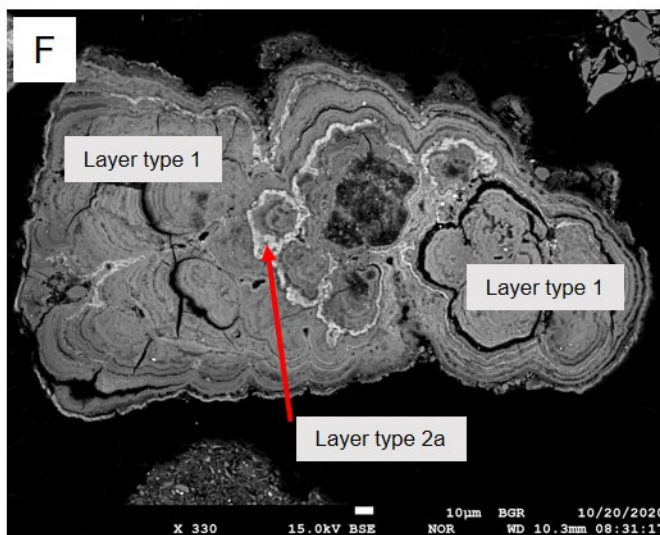
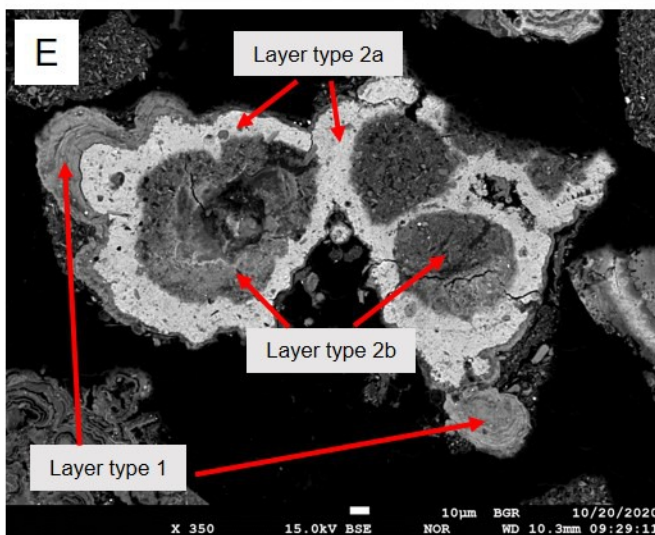
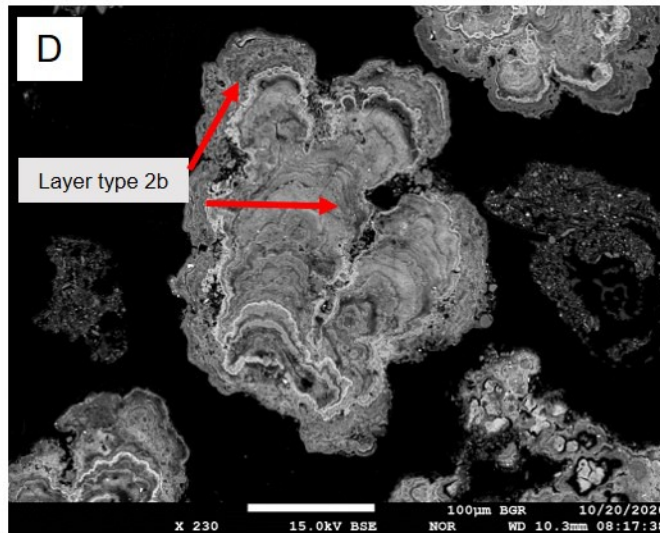
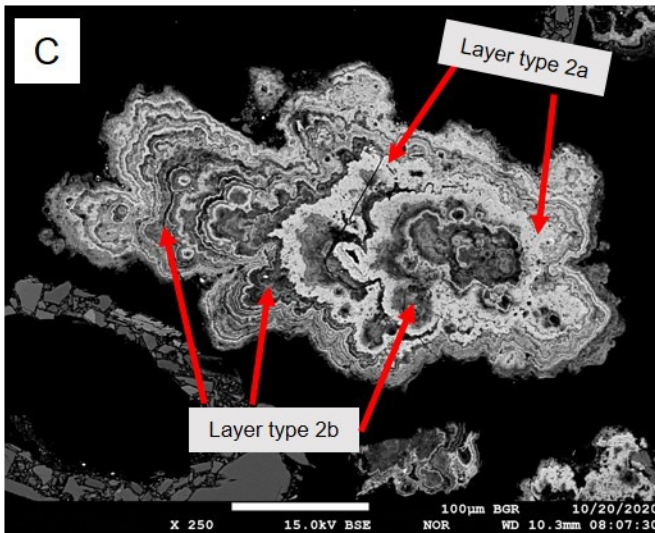
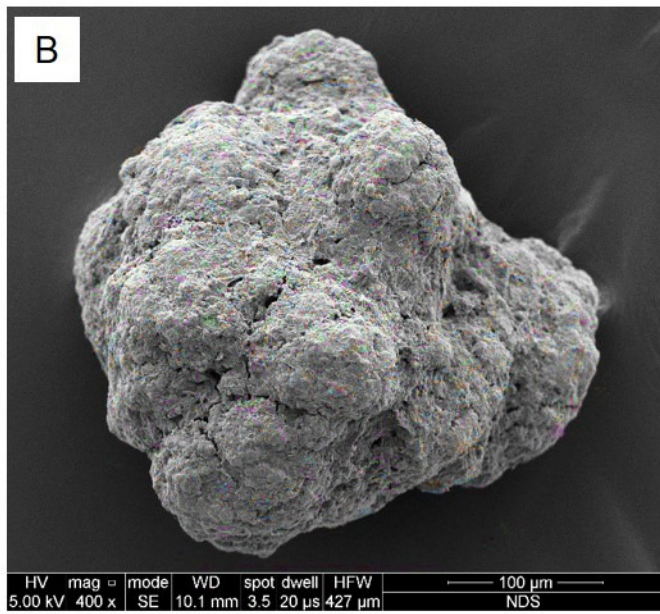
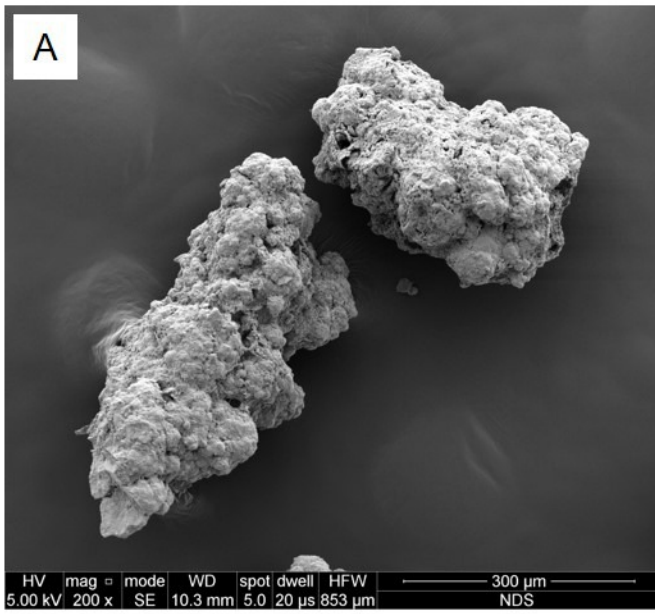
1393
1394 **Appendixes 1 – 2:** XRD patterns of Mn-micronodule samples after drying at 30°C (black patterns) and after heating
1395 at 105°C for 24h (grey patterns). [a.u.] = arbitrary units; Fsp = feldspar; Qz = quartz.

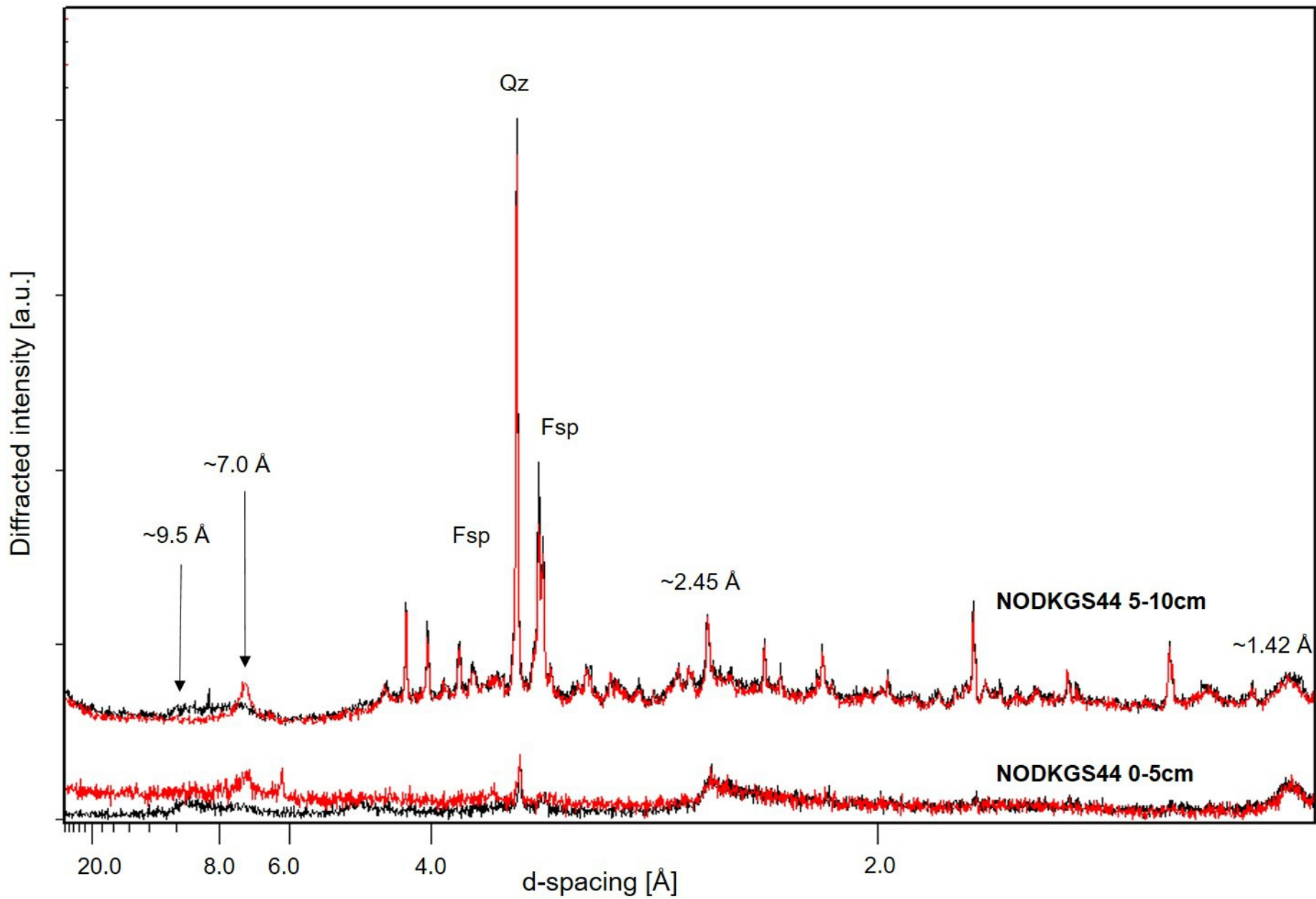
1396
1397 **Appendix 3:** XRD patterns of Mn-micronodule samples after drying at 30°C. [a.u.] = arbitrary units; Fsp = feldspar;
1398 Qz = quartz.

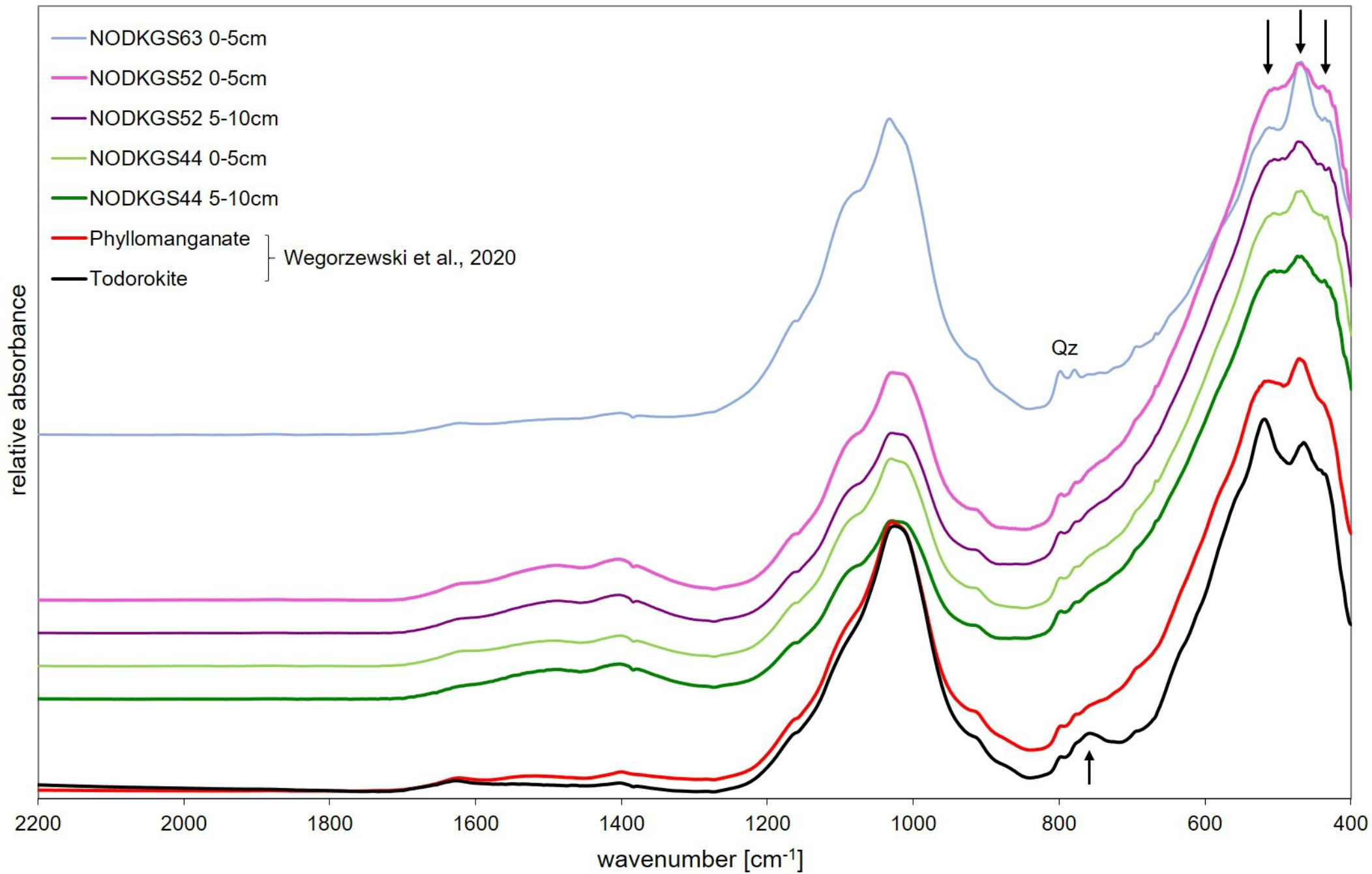
1399
1400 **Appendix 4:** IR spectra of five Mn-micronodule samples compared with the IR spectra of a phyllomangante-rich
1401 Mn-nodule and a todorokite-rich Mn-nodule from Wegorzewski et al. (2020) as well as with the IR spectra of two
1402 Mn-nodule standards (Nod-P-1 and Nod-A-1). The black arrows mark the IR bands that are characteristic for Mn-
1403 oxides: phyllomanganate (400 – 515 cm^{-1}) and todorokite ($\sim 760\text{cm}^{-1}$). Quartz (Qz) and other minor impurities (1200
1404 – 900 cm^{-1}) were detected.



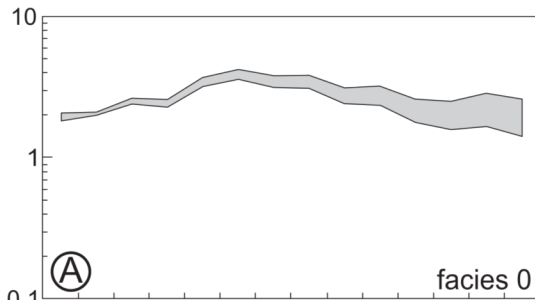




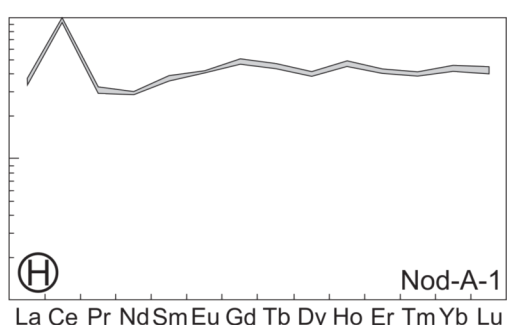
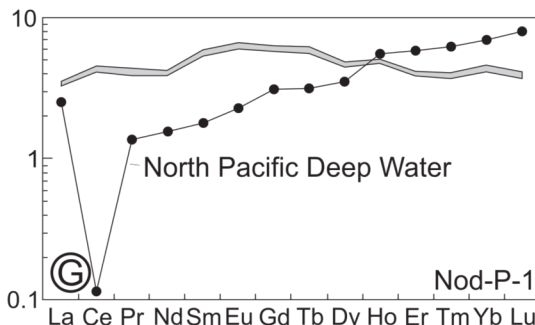
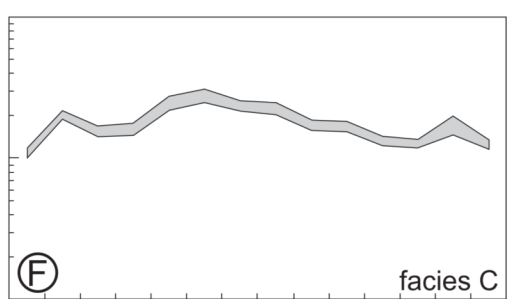
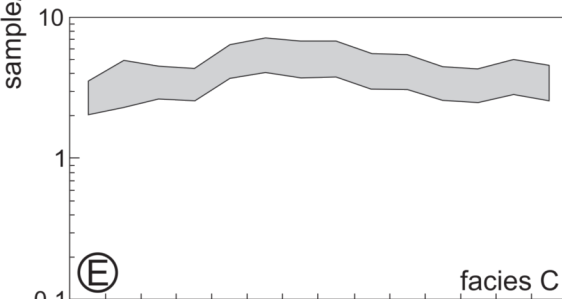
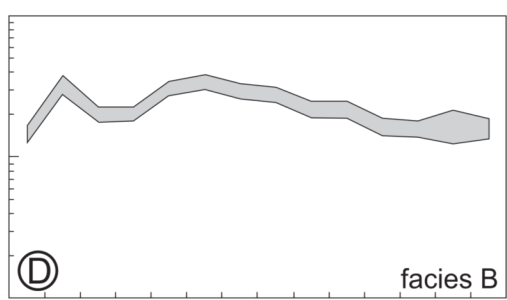
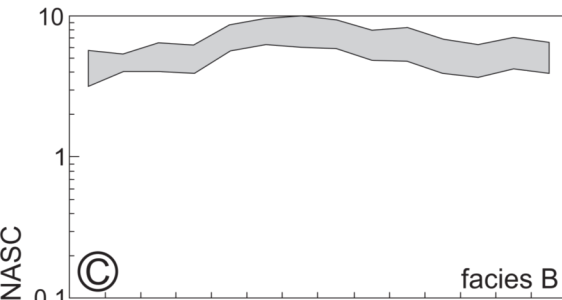
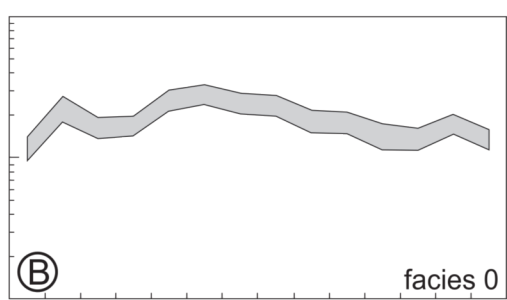


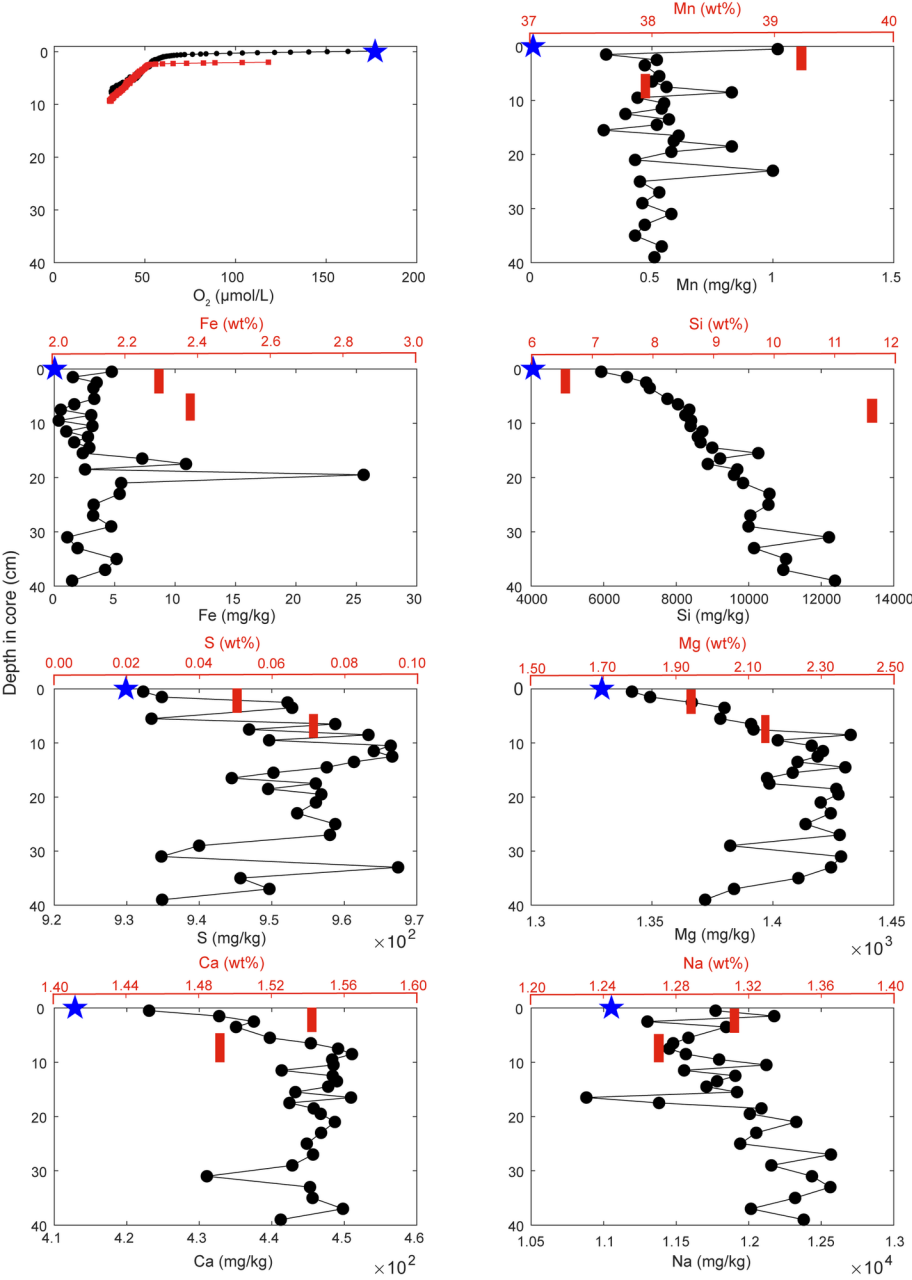


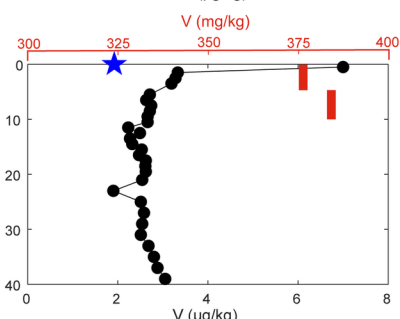
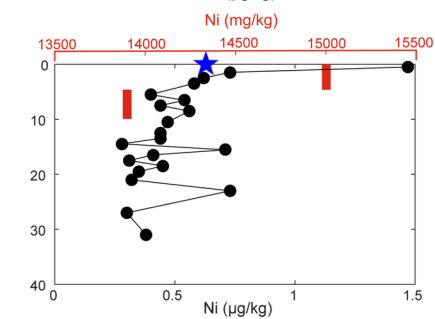
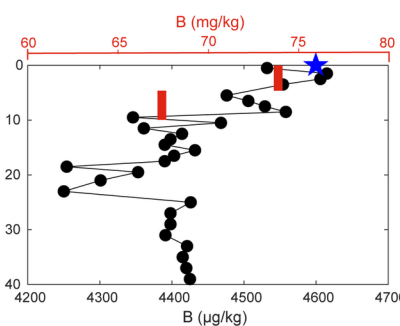
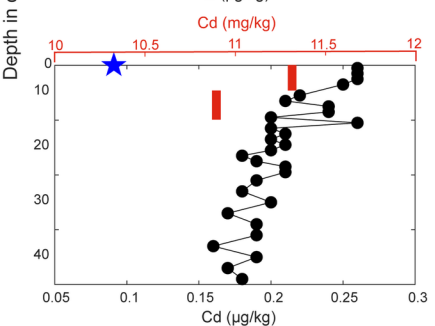
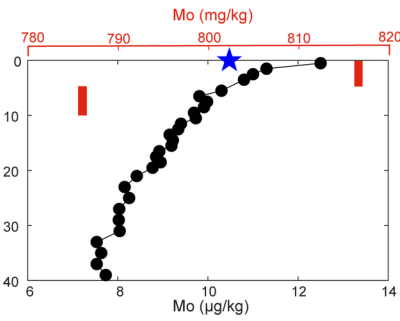
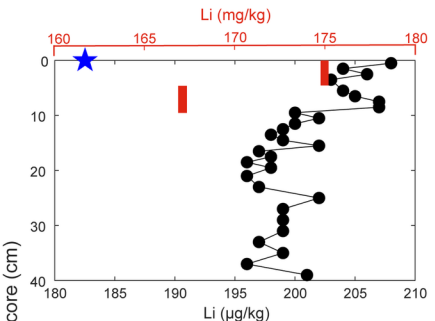
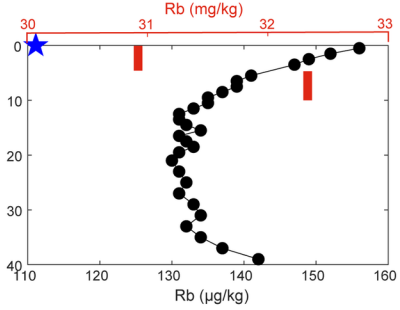
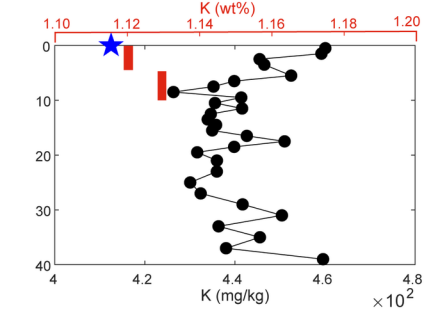
Mn-nodules

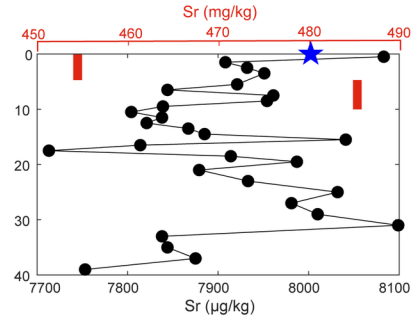
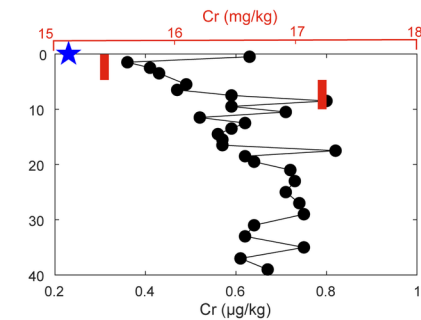
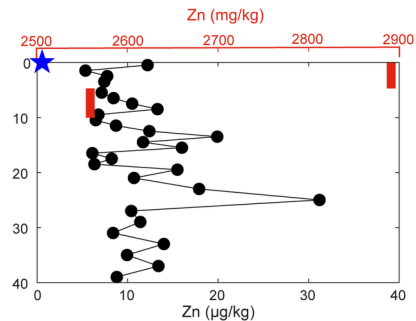
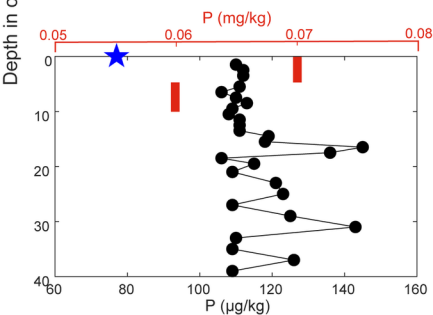
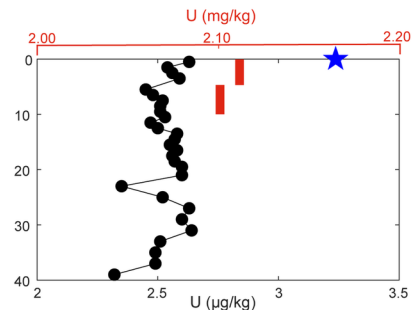
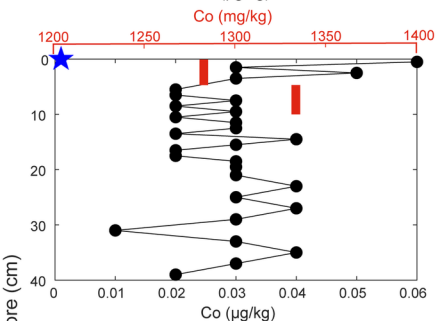
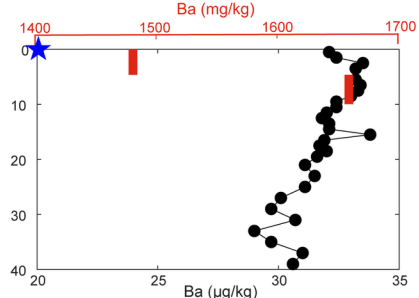
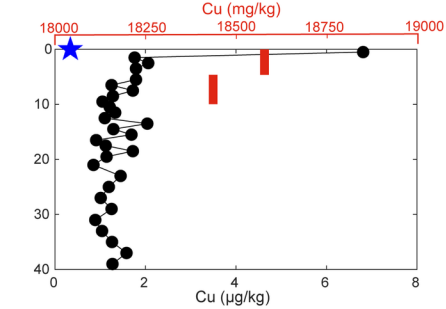


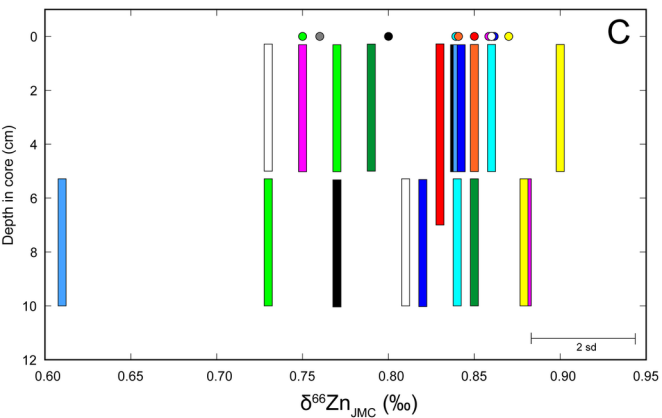
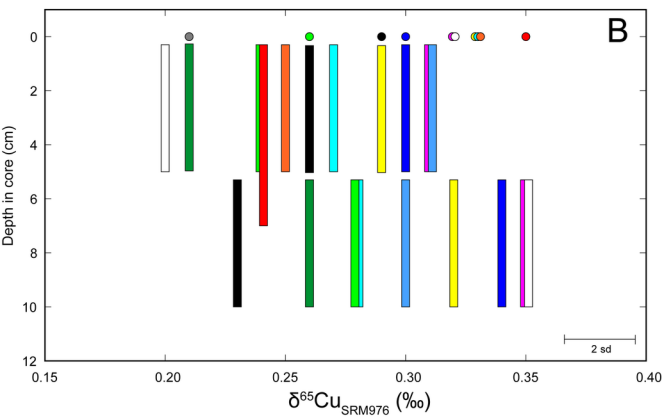
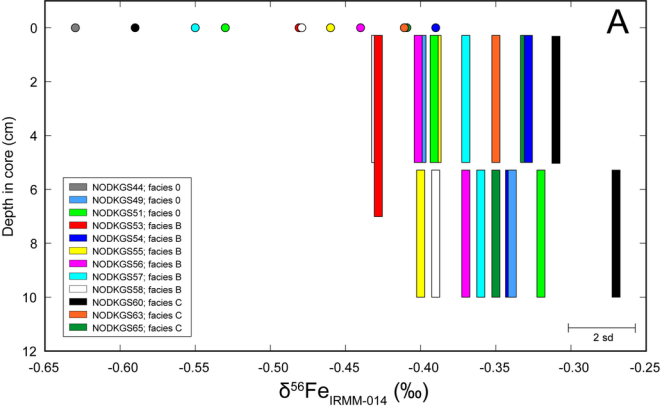
Mn-micronodules

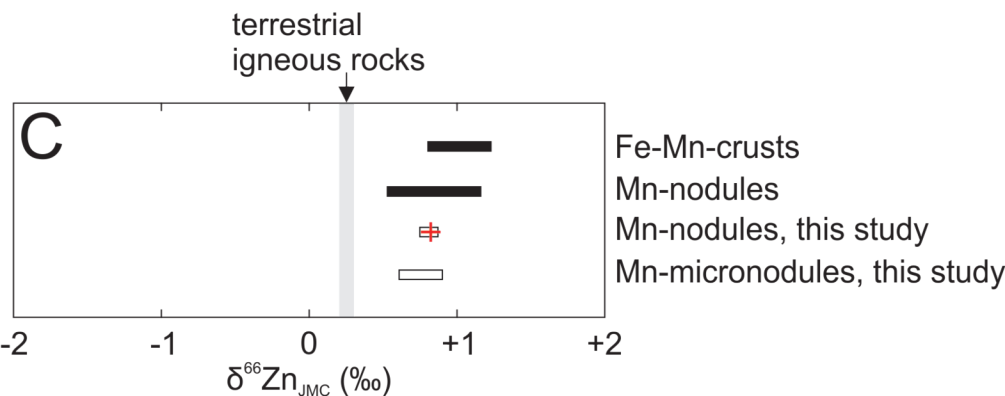
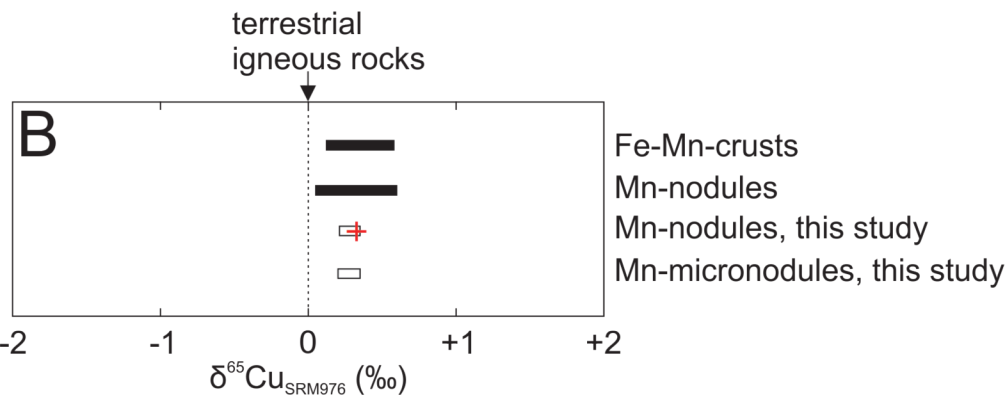
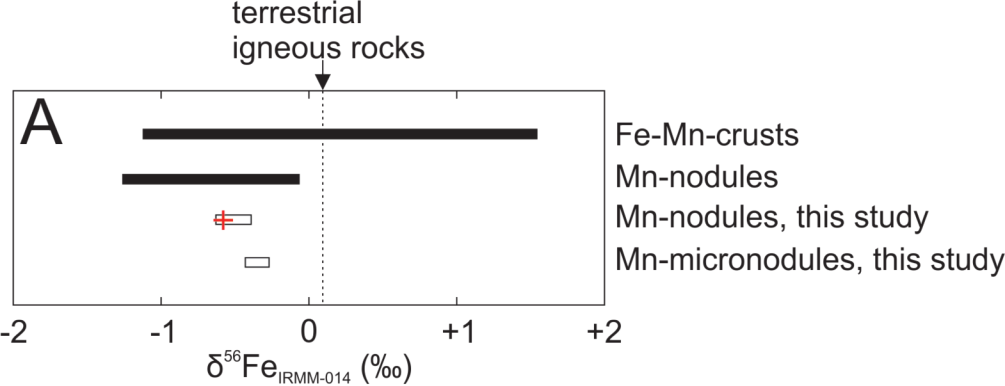












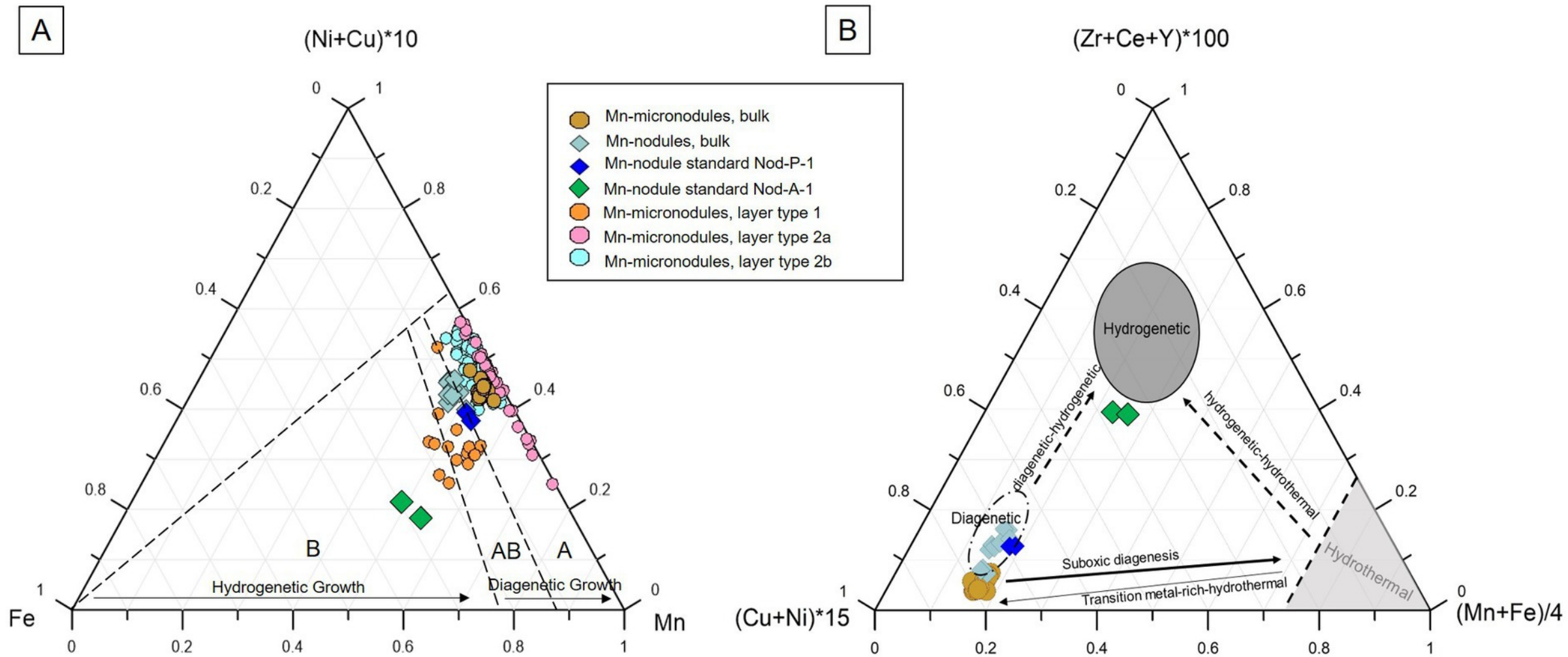


Table 1

Investigated box cores.

Box core #	Latitude (N)	Longitude (W)	Depth (m)	Mn-nodule facies	Nodule density coverage (kg/m ²)	Remarks
NODKGS44	14°03.99′	130°05.64′	5033	0	0	deepest
NODKGS48	14°03.11′	130°05.16′	5017	0	0	deepest
NODKGS49	14°04.00′	130°05.24′	5032	0	0	deepest
NODKGS50	14°03.36′	130°04.80′	5035	0	0	deepest
NODKGS51	14°03.41′	130°05.48′	5010	0	0	deepest
NODKGS52	14°02.99′	130°05.24′	5027	0	0	deepest
NODKGS53	14°02.34′	130°08.29′	4957	B	22.4	shallowest
NODKGS54	14°02.82′	130°08.10′	4905	B	18.4	shallowest
NODKGS55	14°03.05′	130°08.00′	4910	B	16.0	shallowest
NODKGS56	14°03.18′	130°08.64′	4838	B	18.6	shallowest
NODKGS57	14°03.24′	130°07.80′	4938	B	16.7	shallowest
NODKGS58	14°03.24′	130°08.16′	4900	B	12.3	shallowest
NODKGS60	14°03.67′	130°06.25′	5000	C	9.8	middle depth
NODKGS63	14°04.28′	130°07.06′	4978	C	18.4	middle depth
NODKGS65	14°03.71′	130°06.80′	4969	C	18.3	middle depth

Table 2

Mineralogy (XRD, IR) of the studied Mn-micronodules and Mn-nodules.

Sample ID	Description	Mn-nodule facies	Mineralogy
NODKGS44 0-5cm ^a	Mn-micronodules	0	10 Å and 7 Å phylломanganates, vernadite, quartz, feldspar
NODKGS44 5-10cm ^a	Mn-micronodules	0	10 Å and 7 Å phylломanganates, vernadite, quartz, feldspar
NODKGS48 0-5cm ^a	Mn-micronodules	0	10 Å and 7 Å phylломanganates, vernadite, quartz, feldspar
NODKGS48 5-10cm ^a	Mn-micronodules	0	10 Å and 7 Å phylломanganates, vernadite, quartz, feldspar
NODKGS49 0-5cm	Mn-micronodules	0	10 Å and 7 Å phylломanganates, vernadite, quartz
NODKGS49 5-10cm	Mn-micronodules	0	10 Å and 7 Å phylломanganates, vernadite, quartz
NODKGS51 0-5cm	Mn-micronodules	0	10 Å and 7 Å phylломanganates, vernadite, quartz
NODKGS51 5-10cm	Mn-micronodules	0	10 Å and 7 Å phylломanganates, vernadite, quartz
NODKGS52 0-5cm ^a	Mn-micronodules	0	10 Å and 7 Å phylломanganates, vernadite, quartz, feldspar
NODKGS52 5-10cm ^a	Mn-micronodules	0	10 Å and 7 Å phylломanganates, vernadite, quartz, feldspar
NODKGS53	Mn-nodule	B	10 Å and 7 Å phylломanganates, vernadite, quartz, feldspar
NODKGS53 0-7 cm	Mn-micronodules	B	10 Å and 7 Å phylломanganates, vernadite, quartz
NODKGS54 0-5cm ^a	Mn-micronodules	B	10 Å and 7 Å phylломanganates, vernadite, quartz
NODKGS54 5-10cm	Mn-micronodules	B	10 Å and 7 Å phylломanganates, vernadite, quartz
NODKGS55 0-5cm	Mn-micronodules	B	10 Å and 7 Å phylломanganates, vernadite, quartz
NODKGS55 5-10cm	Mn-micronodules	B	10 Å and 7 Å phylломanganates, vernadite, quartz
NODKGS56 0-5cm	Mn-micronodules	B	10 Å and 7 Å phylломanganates, vernadite, quartz
NODKGS56 5-10cm ^a	Mn-micronodules	B	10 Å and 7 Å phylломanganates, vernadite, quartz
NODKGS57 0-5cm ^a	Mn-micronodules	B	10 Å and 7 Å phylломanganates, vernadite, quartz, feldspar
NODKGS57 5-10cm	Mn-micronodules	B	10 Å and 7 Å phylломanganates, vernadite, quartz
NODKGS58 0-5cm	Mn-micronodules	B	10 Å and 7 Å phylломanganates, vernadite, quartz, feldspar
NODKGS58 5-10cm	Mn-micronodules	B	10 Å and 7 Å phylломanganates, vernadite, quartz, feldspar
NODKGS60 0-5cm ^a	Mn-micronodules	C	10 Å and 7 Å phylломanganates, vernadite, quartz
NODKGS60 5-10cm	Mn-micronodules	C	10 Å and 7 Å phylломanganates, vernadite, quartz
NODKGS63	Mn-nodule	C	10 Å and 7 Å phylломanganates, vernadite, quartz, feldspar
NODKGS63 0-5cm ^a	Mn-micronodules	C	10 Å and 7 Å phylломanganates, vernadite, quartz
NODKGS65 0-5cm	Mn-micronodules	C	10 Å and 7 Å phylломanganates, vernadite, quartz
NODKGS65 5-10cm	Mn-micronodules	C	10 Å and 7 Å phylломanganates, vernadite, quartz

^a samples analysed by both XRD and IR

Table 3

Chemical composition (ICP-MS) of the studied Mn-micronodules and Mn-nodules.

Sample ID	Description	Mn-nodule facies	Mn (wt.%)	Fe	Mn/Fe	Si	Al	Ca	Mg	Na	K	Ti	P	S	Li (mg/kg)	Be	B
NODKGS48 0-5cm	Mn-micronodules	0	41.0	2.29	17.9	19.6	1.90	1.68	2.30	1.16	1.15	0.20	0.07	0.07	104	0.97	103
NODKGS48 5-10cm	Mn-micronodules	0	37.8	2.15	17.6	15.1	1.73	1.48	2.10	1.19	1.03	0.18	0.07	0.05	46.4	0.88	66.7
NODKGS44	Mn-nodule	0	27.4	4.64	5.90	-	0.87	1.30	0.70	2.13	0.86	0.18	0.12	0.11	181	1.60	93.9
NODKGS49 0-5cm	Mn-micronodules	0	44.5	2.47	18.0	9.85	1.95	1.86	2.37	1.08	1.11	0.22	0.07	0.04	95.3	1.08	65.0
NODKGS49 5-10cm	Mn-micronodules	0	36.8	2.08	17.7	49.1	1.69	1.62	1.92	0.93	0.97	0.19	0.06	0.05	43.4	0.83	55.3
NODKGS50 0-5cm	Mn-micronodules	0	31.4	1.77	17.7	11.6	1.49	1.27	1.73	0.80	0.85	0.16	0.06	0.04	80.1	0.99	71.2
NODKGS50 5-10cm	Mn-micronodules	0	44.6	2.36	18.9	4.26	1.92	1.83	2.40	1.24	1.16	0.23	0.08	0.06	87.0	0.83	76.8
NODKGS51	Mn-nodule	0	25.9	4.78	5.41	-	2.58	1.54	1.67	2.32	0.84	0.19	0.12	0.13	155	1.79	90.3
NODKGS51 0-5cm	Mn-micronodules	0	43.1	2.38	18.1	6.69	2.01	1.71	2.30	1.20	1.14	0.23	0.07	0.07	70.1	1.03	106
NODKGS51 5-10cm	Mn-micronodules	0	41.5	2.55	16.3	23.2	2.00	1.60	2.13	1.14	1.15	0.22	0.08	0.05	80.1	1.08	85.9
NODKGS52 0-5cm	Mn-micronodules	0	39.4	2.17	18.2	29.2	1.78	1.57	2.00	1.15	1.10	0.20	0.07	0.04	67.9	0.85	63.5
NODKGS52 5-10cm	Mn-micronodules	0	35.3	2.11	16.7	13.1	1.67	1.38	2.00	1.05	1.16	0.19	0.06	0.04	70.7	0.94	71.9
NODKGS53	Mn-nodule	B	29.3	5.77	5.07	-	2.49	1.58	1.96	2.53	0.99	0.32	0.14	0.11	133	2.31	94.6
NODKGS53 0-7 cm	Mn-micronodules	B	33.2	2.89	11.5	13.5	2.08	1.46	1.79	1.32	1.13	0.27	0.07	0.08	112	1.13	86.1
NODKGS54	Mn-nodule	B	29.3	5.99	4.89	-	2.59	1.58	2.06	2.70	0.96	0.35	0.15	0.12	183	2.28	101
NODKGS54 0-5cm	Mn-micronodules	B	37.0	3.27	11.3	9.86	2.08	1.55	1.95	1.36	0.97	0.30	0.07	0.07	54.6	1.19	107
NODKGS54 5-10cm	Mn-micronodules	B	31.8	2.79	11.4	63.0	1.96	1.25	1.86	0.90	0.95	0.23	0.06	0.05	87.0	1.22	89.8
NODKGS55	Mn-nodule	B	28.4	6.74	4.21	-	2.71	1.68	2.02	2.38	0.98	0.39	0.21	0.13	121	2.58	107
NODKGS55 0-5cm	Mn-micronodules	B	37.0	3.21	11.5	6.60	2.08	1.51	2.06	1.23	1.12	0.29	0.07	0.10	76.8	1.26	102
NODKGS55 5-10cm	Mn-micronodules	B	35.4	3.30	10.7	3.03	2.17	1.45	2.06	1.08	1.03	0.28	0.07	0.06	89.5	1.26	104
NODKGS56	Mn-nodule	B	30.9	5.87	5.26	-	2.42	1.62	2.08	2.68	0.98	0.35	0.15	0.12	132	2.35	106
NODKGS56 0-5cm	Mn-micronodules	B	36.6	3.68	9.95	7.33	2.45	1.58	2.08	1.23	1.06	0.33	0.08	0.06	77.9	1.29	89.7
NODKGS56 5-10cm	Mn-micronodules	B	36.3	3.69	9.82	1.17	2.30	1.48	2.23	0.97	1.05	0.36	0.08	0.05	72.7	1.31	65.0
NODKGS57	Mn-nodule	B	27.6	6.20	4.44	-	2.36	3.06	1.86	2.40	0.84	0.36	0.77	0.14	109	2.52	104
NODKGS57 0-5cm	Mn-micronodules	B	35.2	2.85	12.3	14.2	2.02	1.49	1.89	1.12	0.96	0.26	0.07	0.06	62.7	1.04	61.2
NODKGS57 5-10cm	Mn-micronodules	B	42.5	3.42	12.4	3.44	2.52	1.74	2.37	1.38	1.24	0.31	0.08	0.07	127	1.18	109
NODKGS58	Mn-nodule	B	26.6	5.48	4.85	-	2.11	1.45	1.77	2.23	0.85	0.31	0.14	0.11	119	2.06	98.9
NODKGS58 0-5cm	Mn-micronodules	B	38.2	3.59	10.6	9.37	2.29	1.63	2.15	1.27	1.14	0.31	0.08	0.07	74.4	1.37	101
NODKGS58 5-10cm	Mn-micronodules	B	39.7	3.72	10.7	16.8	2.50	1.65	2.32	1.10	1.09	0.32	0.08	0.06	74.9	1.40	81.2
NODKGS60	Mn-nodule	C	26.7	4.50	5.94	-	2.15	1.46	1.59	2.62	0.90	0.19	0.12	0.10	165	1.55	84.7
NODKGS60 0-5cm	Mn-micronodules	C	38.8	1.97	19.7	3.18	1.85	1.45	2.04	1.24	1.13	0.19	0.06	0.03	208	0.95	58.7
NODKGS60 5-10cm	Mn-micronodules	C	40.8	2.04	20.0	22.6	2.02	1.52	2.09	1.33	1.35	0.19	0.06	0.05	252	0.85	54.7
NODKGS63	Mn-nodule	C	31.4	5.35	5.88	-	2.19	1.50	1.99	2.60	1.04	0.32	0.14	0.11	240	2.10	99.7
NODKGS63 0-5cm	Mn-micronodules	C	37.2	2.47	15.1	6.97	2.16	1.42	2.02	1.50	1.06	0.22	0.07	0.07	163	1.04	64.4
NODKGS65 0-5cm	Mn-micronodules	C	39.3	2.26	17.4	6.80	2.08	1.54	1.95	1.31	1.12	0.21	0.07	0.05	175	0.89	74.4
NODKGS65 5-10cm	Mn-micronodules	C	37.9	2.36	16.1	11.6	2.30	1.49	2.15	1.27	1.13	0.21	0.06	0.07	167	0.98	67.3
Average																	
Mn-nodule		0	26.6	4.71	5.65	-	1.73	1.42	1.19	2.23	0.85	0.19	0.12	0.12	168	1.69	92.1
Mn-micronodules		0	39.5	2.23	17.7	18.2	1.81	1.60	2.12	1.09	1.08	0.20	0.07	0.05	74	0.95	76.5
Mn-nodule		B	28.7	6.01	4.77	-	2.45	1.83	1.96	2.49	0.93	0.35	0.26	0.12	133	2.35	101.9
Mn-micronodules		B	36.6	3.31	11.1	13.5	2.22	1.53	2.07	1.18	1.07	0.30	0.07	0.07	83	1.24	90.6
Mn-nodule		C	29.1	4.92	5.91	-	2.17	1.48	1.79	2.61	0.97	0.26	0.13	0.10	203	1.82	92.2
Mn-micronodules		C	38.8	2.22	17.5	10.2	2.09	1.48	2.05	1.33	1.16	0.20	0.06	0.05	193	0.94	63.9
Mn-nodule		average	28.2	5.33	5.28	-	2.24	1.64	1.73	2.53	0.93	0.27	0.19	0.11	159	2.02	95.8
Mn-micronodules		average	38.2	2.69	14.2	14.7	2.04	1.55	2.09	1.17	1.09	0.24	0.07	0.06	101	1.07	80.0
Nod-P-1, split #4-25 (average)	Mn-nodule, standard		34.1	5.91	5.76	2.24	2.47	2.27	2.04	1.71	1.01	0.26	0.15	0.07	149	2.41	104
Nod-P-1, split 9-3 (average)	Mn-nodule, standard		33.7	5.65	5.98	10.0	2.24	2.16	1.88	1.60	0.93	0.26	0.14	0.06	144	2.28	103
Nod-P-1 (reference) ^a	Mn-nodule, standard		29.6	5.89	5.03	5.85	2.46	2.24	2.03	1.71	1.00	0.27	0.21	0.10	140	2.30	95.0
Nod-A-1, split #16-7 (average)	Mn-nodule, standard		16.4	9.94	1.65	1.17	1.96	10.8	2.71	0.78	0.43	0.26	0.36	0.23	73.1	5.85	117
Nod-A-1, split 62-16 (average)	Mn-nodule, standard		19.3	9.90	1.95	5.42	1.89	10.2	2.51	0.75	0.43	0.27	0.35	0.23	71.8	5.10	103
Nod-A-1 (reference) ^a	Mn-nodule, standard		18.3	11.2	1.63	1.74	2.08	11.4	2.83	0.87	0.49	0.30	0.59	0.34	76.1	5.60	120

^a data from Axelsson et al. (2002)

Table 3 (continued)

Sample ID	Description	Mn-nodule facies	Sc (mg/kg)	V	Cr	Co	Ni	Cu	Zn	Se	As	Rb	Sr	Y	Zr	Nb	Mo
NODKGS48 0-5cm	Mn-micronodules	0	<7	467	12.8	1488	15373	21422	3136	-	53.7	25.9	523	29.4	70.6	10.5	942
NODKGS48 5-10cm	Mn-micronodules	0	<7	393	12.4	1390	13422	19447	2937	-	49.6	24.4	562	29.3	73.6	11.0	826
NODKGS44	Mn-nodule	0	<7	451	11.9	2193	10678	13786	1861	1.92	63.3	19.3	471	29.3	176	12.3	755
NODKGS49 0-5cm	Mn-micronodules	0	8.54	478	14.3	1705	15224	21964	3134	-	53.9	28.6	652	34.7	82.1	11.5	1017
NODKGS49 5-10cm	Mn-micronodules	0	<7	385	11.4	1450	13357	18412	3534	-	49.2	23.6	589	28.7	70.1	9.78	822
NODKGS50 0-5cm	Mn-micronodules	0	<7	345	11.4	1213	11052	16393	2853	-	43.1	21.0	418	23.7	61.0	8.02	702
NODKGS50 5-10cm	Mn-micronodules	0	<7	505	16.4	1678	15063	24627	3356	-	53.8	28.7	624	31.7	77.7	11.6	1016
NODKGS51	Mn-nodule	0	<7	433	13.6	2075	11002	14555	1708	2.46	63.9	24.4	501	58.8	206	14.9	690
NODKGS51 0-5cm	Mn-micronodules	0	<7	459	14.2	1632	15179	21589	3309	-	55.6	27.7	545	31.8	87.2	12.7	934
NODKGS51 5-10cm	Mn-micronodules	0	<7	424	15.6	1568	14668	21043	3413	-	51.8	27.8	552	29.8	80.8	12.0	939
NODKGS52 0-5cm	Mn-micronodules	0	<7	417	16.6	1479	13576	18787	2710	-	49.4	25.6	585	30.0	75.1	10.9	895
NODKGS52 5-10cm	Mn-micronodules	0	<7	381	12.1	1389	13100	18934	2743	-	48.6	26.3	535	28.9	74.9	10.4	882
NODKGS53	Mn-nodule	B	10.4	531	9.77	2544	14764	14802	1958	4.38	83.1	21.8	625	91.2	317	23.1	819
NODKGS53 0-7 cm	Mn-micronodules	B	7.37	400	14.9	1997	12907	14448	2276	-	57.9	28.9	452	33.0	100	13.8	705
NODKGS54	Mn-nodule	B	11.6	510	17.2	2191	14368	14874	2125	4.92	82.1	22.8	624	94.3	326	23.2	799
NODKGS54 0-5cm	Mn-micronodules	B	<7	424	15.4	2223	15182	16049	2572	-	65.7	28.0	507	35.6	111	13.8	709
NODKGS54 5-10cm	Mn-micronodules	B	<7	361	14.1	1829	12522	13123	2151	-	55.0	29.6	449	29.9	89.2	12.5	679
NODKGS55	Mn-nodule	B	11.3	535	10.8	2706	13634	11179	1830	5.16	94.4	23.0	673	102	387	28.7	709
NODKGS55 0-5cm	Mn-micronodules	B	<7	425	14.4	2166	14975	21668	2509	-	69.2	30.5	553	35.7	112	14.5	741
NODKGS55 5-10cm	Mn-micronodules	B	<7	410	19.0	2042	14693	14996	2461	-	62.4	31.8	528	35.3	108	14.6	764
NODKGS56	Mn-nodule	B	11.0	541	9.29	2449	13933	15103	1970	4.83	81.7	21.3	645	98.0	328	24.5	720
NODKGS56 0-5cm	Mn-micronodules	B	7.14	446	15.8	2394	14558	15092	2603	-	68.9	31.3	573	39.4	132	16.8	670
NODKGS56 5-10cm	Mn-micronodules	B	7.02	456	16.6	2280	13606	15551	2261	-	68.5	31.5	579	37.1	119	15.9	730
NODKGS57	Mn-nodule	B	13.3	514	10.0	2633	14036	11425	1846	6.43	82.9	21.1	694	197	355	26.3	706
NODKGS57 0-5cm	Mn-micronodules	B	7.45	398	13.7	1967	14131	15399	2244	-	59.6	26.2	476	32.3	95.4	13.1	681
NODKGS57 5-10cm	Mn-micronodules	B	7.75	491	18.5	2343	16639	17766	2665	-	65.4	35.0	565	36.3	111	15.1	893
NODKGS58	Mn-nodule	B	8.25	485	9.98	2457	12602	11311	1722	4.05	78.4	20.3	573	83.0	299	22.3	698
NODKGS58 0-5cm	Mn-micronodules	B	7.22	431	16.6	2349	15010	16424	2507	-	72.1	32.1	582	42.0	128	17.0	727
NODKGS58 5-10cm	Mn-micronodules	B	7.69	463	17.2	2497	15481	16658	2624	-	68.9	33.1	629	38.0	118	16.8	774
NODKGS60	Mn-nodule	C	<7	446	10.8	2014	11002	15492	1745	2.83	61.9	22.3	465	57.9	188	13.8	717
NODKGS60 0-5cm	Mn-micronodules	C	<7	349	15.2	1161	12930	18764	2510	-	45.5	27.9	460	28.5	72.7	11.5	892
NODKGS60 5-10cm	Mn-micronodules	C	<7	358	15.0	1061	12513	18137	2617	-	39.2	30.5	468	26.1	63.2	9.32	904
NODKGS63	Mn-nodule	C	10.2	509	9.88	2226	13066	11366	2060	4.81	80.5	21.0	576	91.1	308	20.9	746
NODKGS63 0-5cm	Mn-micronodules	C	<7	388	16.4	1505	13758	17520	2617	-	52.8	31.0	477	30.0	81.2	10.7	757
NODKGS65 0-5cm	Mn-micronodules	C	<7	378	15.4	1282	15040	18562	2887	-	48.2	30.9	454	29.3	74.8	10.2	817
NODKGS65 5-10cm	Mn-micronodules	C	10.0	385	17.2	1333	13883	18400	2567	-	44.5	32.3	485	29.0	75.4	10.4	787
Average																	
Mn-nodule		0	<7	442	12.7	2134	10840	14170	1784	2.2	63.6	21.9	486	44.0	190.8	13.6	723
Mn-micronodules		0	<7	425	13.7	1499	14001	20262	3113	-	50.9	25.9	559	29.8	75.3	10.8	898
Mn-nodule		B	11.0	519	11.2	2497	13889	13116	1908	5.0	83.8	21.7	639	110.9	335.1	24.7	742
Mn-micronodules		B	7.4	428	16.0	2190	14518	16107	2443	-	64.9	30.7	536	35.9	111.2	14.9	734
Mn-nodule		C	10.2	477	10.4	2120	12034	13429	1903	3.8	71.2	21.7	520	74.5	248.1	17.3	731
Mn-micronodules		C	10.0	372	15.8	1268	13625	18276	2640	-	46.0	30.5	469	28.6	73.4	10.4	831
Mn-nodule		average	10.9	488	11.4	2288	12553	13680	1864	3.9	74.2	22.1	566	83.4	268	19.3	740
Mn-micronodules		average	7.79	416	15.1	1747	14148	18122	2738	-	55.9	28.8	532	32.1	90	12.5	816
Nod-P-1, split #4-25 (average)	Mn-nodule, standard		<7	483	13.2	2276	13801	12044	2126	-	119	26.6	681	96.5	286	22.3	702
Nod-P-1, split 9-3 (average)	Mn-nodule, standard		11.1	484	13.8	2205	12862	10835	1922	-	101	25.5	661	89.4	268	22.3	705
Nod-P-1 (reference)	Mn-nodule, standard		9.70	510	13.3	2290	13500	11200	2020	-	88.5	23.7	670	90	280	21.3	675
Nod-A-1, split #16-7 (average)	Mn-nodule, standard		<7	578	18.0	2988	6122	1034	812	-	363	10.2	1525	115	299	42.2	358
Nod-A-1, split 62-16 (average)	Mn-nodule, standard		11.7	580	18.0	2898	5630	950	701	-	329	9.9	1451	113	298	45.7	391
Nod-A-1 (reference)	Mn-nodule, standard		12.4	660	20.9	3180	6450	1130	800	-	310	10.6	1630	120	310	43.1	390

Table 3 (continued)

Sample ID	Description	Mn-nodule facies	Cd (mg/kg)	Sn	Sb	Te	Ba	Hf	Ta	W	Tl	Pb	Bi	Th	U	Au	Pt
NODKGS48 0-5cm	Mn-micronodules	0	13.3	0.74	61.2	1.21	1567	1.12	0.22	77.8	67.1	419	4.23	7.70	2.63	<0.030	0.052
NODKGS48 5-10cm	Mn-micronodules	0	12.0	0.74	54.5	1.12	1521	1.09	0.18	57.7	53.5	378	4.22	7.58	2.39	<0.030	0.046
NODKGS44	Mn-nodule	0	18.0	0.24	46.1	1.97	1912	2.37	0.27	34.5	121	299	2.68	7.41	3.23	-	0.058
NODKGS49 0-5cm	Mn-micronodules	0	13.9	0.82	64.1	1.40	1746	1.27	0.19	78.6	77.1	471	4.81	9.34	2.93	<0.030	0.055
NODKGS49 5-10cm	Mn-micronodules	0	11.3	0.72	53.1	1.13	1449	1.04	0.19	57.3	54.3	381	4.03	7.48	2.35	<0.030	0.038
NODKGS50 0-5cm	Mn-micronodules	0	10.6	0.69	46.8	0.79	1271	0.91	0.18	55.0	45.1	328	3.52	6.46	2.11	<0.030	0.038
NODKGS50 5-10cm	Mn-micronodules	0	15.0	0.82	62.3	1.22	1719	1.24	0.24	87.9	69.4	427	4.61	8.65	2.81	<0.030	0.049
NODKGS51	Mn-nodule	0	15.9	0.28	40.3	2.45	2064	2.87	0.36	38.1	112	349	2.76	11.9	3.21	-	0.069
NODKGS51 0-5cm	Mn-micronodules	0	12.6	0.89	62.2	1.46	1802	1.25	0.26	67.5	66.4	463	4.80	9.20	2.64	<0.030	0.062
NODKGS51 5-10cm	Mn-micronodules	0	12.5	1.69	62.8	1.38	1802	1.19	0.25	70.3	60.2	455	4.88	8.79	2.58	<0.030	0.050
NODKGS52 0-5cm	Mn-micronodules	0	12.3	0.77	54.7	1.04	1581	1.13	0.22	64.0	63.0	394	4.02	7.81	2.48	<0.030	0.049
NODKGS52 5-10cm	Mn-micronodules	0	12.0	0.79	53.9	1.08	1527	1.12	0.20	70.6	55.7	405	4.40	7.85	2.43	<0.030	0.057
NODKGS53	Mn-nodule	B	19.5	0.36	48.9	3.58	2619	4.59	0.30	69.2	238	453	6.27	24.2	3.93	-	0.121
NODKGS53 0-7 cm	Mn-micronodules	B	10.9	0.98	43.9	1.36	1579	1.63	0.28	53.9	74.4	423	5.62	12.2	2.23	<0.030	0.047
NODKGS54	Mn-nodule	B	18.5	0.40	48.7	3.38	2220	4.76	0.33	61.0	260	481	7.56	28.9	4.20	-	0.122
NODKGS54 0-5cm	Mn-micronodules	B	11.1	1.04	46.2	1.59	1639	1.71	0.24	54.4	84.1	469	6.60	13.9	2.53	<0.030	0.079
NODKGS54 5-10cm	Mn-micronodules	B	9.91	0.96	43.7	1.33	1652	1.48	0.26	57.5	67.7	423	5.82	12.2	2.19	<0.030	0.064
NODKGS55	Mn-nodule	B	16.1	0.43	39.5	4.31	2517	5.60	0.36	75.4	199	559	8.07	28.6	4.39	-	0.147
NODKGS55 0-5cm	Mn-micronodules	B	11.9	1.12	51.6	1.66	1639	1.84	0.30	54.2	90.2	484	6.78	14.9	2.66	<0.030	0.063
NODKGS55 5-10cm	Mn-micronodules	B	11.6	1.10	47.0	1.64	1779	1.79	0.29	60.7	81.4	489	7.03	14.8	2.51	<0.030	0.073
NODKGS56	Mn-nodule	B	18.7	0.37	43.8	3.65	2382	4.80	0.32	66.9	281	497	7.19	23.9	4.07	-	0.122
NODKGS56 0-5cm	Mn-micronodules	B	11.4	1.24	45.4	1.75	1999	2.13	0.34	66.3	91.6	536	7.99	16.4	2.86	<0.030	0.095
NODKGS56 5-10cm	Mn-micronodules	B	10.6	1.10	44.3	1.93	2063	1.93	0.28	80.4	69.0	517	8.16	15.8	2.73	<0.030	0.095
NODKGS57	Mn-nodule	B	16.4	0.38	41.9	3.90	2346	5.21	0.35	69.5	217	515	7.59	24.9	4.73	-	0.133
NODKGS57 0-5cm	Mn-micronodules	B	10.2	0.91	43.8	1.41	1403	1.50	0.26	50.2	78.6	402	5.44	12.0	2.24	<0.030	0.050
NODKGS57 5-10cm	Mn-micronodules	B	12.7	1.18	56.5	1.63	1974	1.85	0.34	63.5	86.8	515	6.87	14.6	2.71	<0.030	0.071
NODKGS58	Mn-nodule	B	16.7	0.34	40.3	3.35	2018	4.29	0.29	63.6	190	470	6.49	21.5	3.87	-	0.110
NODKGS58 0-5cm	Mn-micronodules	B	12.1	1.17	45.7	1.57	1852	2.02	0.32	57.2	89.6	519	7.46	15.8	2.83	<0.030	0.073
NODKGS58 5-10cm	Mn-micronodules	B	11.4	1.16	47.2	1.81	1996	1.93	0.31	60.8	73.4	525	7.52	15.8	2.66	<0.030	0.070
NODKGS60	Mn-nodule	C	17.0	0.25	45.8	2.25	1665	2.65	0.25	43.6	152	340	3.21	12.5	3.35	-	0.070
NODKGS60 0-5cm	Mn-micronodules	C	11.0	0.86	59.8	1.04	1486	1.19	0.25	69.9	68.0	354	3.91	7.50	2.06	<0.030	0.041
NODKGS60 5-10cm	Mn-micronodules	C	10.7	0.78	56.6	0.96	1428	1.08	0.22	80.9	62.3	319	3.35	6.64	1.90	<0.030	0.043
NODKGS63	Mn-nodule	C	19.8	0.37	47.7	3.15	1732	4.46	0.31	68.3	220	418	6.73	27.8	4.01	-	0.105
NODKGS63 0-5cm	Mn-micronodules	C	11.0	0.92	51.1	1.04	1656	1.31	0.24	54.7	81.3	377	4.30	8.62	2.29	<0.030	0.056
NODKGS65 0-5cm	Mn-micronodules	C	11.3	0.90	58.0	1.02	1485	1.20	0.23	55.6	74.6	349	3.97	7.77	2.11	<0.030	0.055
NODKGS65 5-10cm	Mn-micronodules	C	10.9	0.88	55.1	1.02	1656	1.24	0.22	61.7	64.3	344	3.77	7.69	2.10	<0.030	0.049
Average																	
Mn-nodule		0	16.9	0.26	43.2	2.21	1988	2.62	0.32	36.3	116	324	2.72	9.64	3.22	-	0.06
Mn-micronodules		0	12.6	0.87	57.6	1.18	1599	1.14	0.21	68.7	61.2	412	4.35	8.09	2.53	<0.030	0.05
Mn-nodule		B	17.6	0.38	43.8	3.70	2350	4.88	0.32	67.6	231	496	7.19	25.33	4.20	-	0.13
Mn-micronodules		B	11.3	1.09	46.8	1.61	1780	1.80	0.29	59.9	80.6	482	6.84	14.40	2.56	<0.030	0.07
Mn-nodule		C	18.4	0.31	46.7	2.70	1698	3.55	0.28	56.0	186	379	4.97	20.18	3.68	-	0.09
Mn-micronodules		C	11.0	0.87	56.1	1.02	1542	1.20	0.23	64.6	70.1	349	3.86	7.65	2.09	<0.030	0.05
Mn-nodule		average	17.9	0.32	45.0	2.94	2076	3.83	0.30	56	188	416	5.24	19.4	3.83	-	0.10
Mn-micronodules		average	11.7	0.96	52.7	1.33	1664	1.43	0.25	64.2	71.1	429	5.31	10.67	2.46	<0.030	0.06
Nod-P-1, split #4-25 (average)	Mn-nodule, standard		23.1	2.28	54.6	5.18	2587	4.25	0.40	59.7	238	507	6.14	17.0	4.24	<0.030	0.115
Nod-P-1, split 9-3 (average)	Mn-nodule, standard		20.4	2.31	48.6	4.42	3264	3.96	0.38	62.0	225	465	5.14	15.6	4.04	<0.030	0.107
Nod-P-1 (reference)	Mn-nodule, standard		22.6	1.90	49.4	4.80	2690	4.20	0.33	57.8	210	475	5.80	16.7	4.00	<0.009	0.120
Nod-A-1, split #16-7 (average)	Mn-nodule, standard		8.07	2.93	34.1	33.6	1411	6.00	0.73	80.7	109	888	11.5	23.1	7.14	0.030	0.505
Nod-A-1, split 62-16 (average)	Mn-nodule, standard		7.58	2.94	30.7	27.7	1510	5.96	0.80	88.5	119	811	9.73	22.6	6.76	0.036	0.495
Nod-A-1 (reference)	Mn-nodule, standard		7.5	3	33.8	30.9	1530	5.80	0.76	87	120	860	10.2	25.1	7	<0.009	0.520

Table 5

Electron microprobe data for Mn-micronodules from sample NODKGS63 0-5 cm.

Layer type	Layer description		Mn (wt.%)	Fe	Mn/Fe	Co	Ni	Cu	Ni+Cu	Si	Al	Ca	Mg	Ti	Na	K	P	S	V (mg/kg)	Mo	Ba
1 (hydrogenetic)	low	average (n ^a = 13)	22.2	5.78	4.15	0.22	0.71	0.68	1.44	4.08	1.60	1.58	1.62	0.68	0.46	0.47	0.15	0.25	490	656	1047
	reflectivity,	std.dev.	3.61	1.35	0.99	0.05	0.15	0.22	0.22	0.97	0.48	0.30	0.18	0.21	0.23	0.18	0.03	0.13	164	231	473
	high	median	22.9	5.52	4.19	0.22	0.72	0.60	1.36	3.85	1.58	1.57	1.63	0.75	0.44	0.50	0.15	0.24	414	587	888
	porosity	min	14.6	2.80	2.56	0.14	0.37	0.39	1.11	2.86	1.01	0.84	1.27	0.33	0.14	0.22	0.08	0.05	269	411	521
		max	27.0	8.31	5.96	0.30	0.91	1.20	1.88	6.33	2.78	2.17	1.98	1.03	1.04	0.92	0.19	0.52	823	1196	2073
2a (suboxic-diagenetic)	dense	average (n = 26)	39.9	0.56	104	0.02	1.24	2.18	3.42	2.47	1.01	1.34	2.09	0.05	1.21	1.49	0.08	0.08	282	1141	400
	growth	std.dev.	2.05	0.27	127	0.02	0.70	0.57	1.06	1.90	0.66	0.13	0.44	0.04	0.40	0.21	0.03	0.08	158	192	137
	structures	median	39.9	0.62	62.9	0.02	0.98	2.38	3.39	2.18	0.88	1.33	2.19	0.05	1.25	1.52	0.08	0.06	322	1094	377
	with high	min	34.6	0.00	33.7	0.00	0.41	1.03	1.44	0.04	0.10	1.09	0.38	0.00	0.17	1.03	0.02	0.00	<DL ^b	903	<DL
	reflectivity	max	44.1	1.18	699	0.07	2.88	3.00	5.45	10.4	3.74	1.62	2.59	0.13	2.19	1.77	0.14	0.51	498	1704	731
2b (suboxic-diagenetic)	porous	average (n = 73)	24.5	1.34	30.9	0.11	1.33	1.25	3.11	3.87	1.51	0.95	1.74	0.20	0.71	0.89	0.07	0.15	359	881	620
	growth	std.dev.	7.03	0.71	24.8	0.10	0.48	0.41	0.61	2.23	0.74	0.29	0.38	0.11	0.27	0.36	0.02	0.13	126	298	284
	structures	median	23.6	1.25	19.8	0.09	1.19	1.31	3.05	3.80	1.49	0.95	1.82	0.20	0.67	0.89	0.06	0.09	357	845	579
	with low	min	12.0	0.08	8.25	0.00	0.52	0.46	1.93	0.14	0.10	0.53	0.92	0.03	0.17	0.25	0.02	0.00	<DL	327	<DL
	reflectivity	max	39.5	3.15	95.5	0.50	2.40	2.20	4.17	10.4	3.74	2.38	2.50	0.54	2.19	1.71	0.12	0.51	749	1877	1652

^a n = number of analyses^b <DL = below detection limits

Table 6
Chemical composition (ICP-MS) of the pore waters from the sediment core NODKGS65.

Sample ID ^a	Na (g/kg)	K	Ca	Mg	S	Si (mg/kg)	B	Sr	Fe (µg/kg)	Mn	Al	P	Li	Rb	Ba	Mo	V	Zn	Cu	Ni	Co
Detection limits ^c	0.0040	0.0003	0.00002	0.00005	0.0001	0.007	0.01	0.0008	0.22	0.06	1.19	0.62	0.46	0.37	0.06	0.09	0.01	1.74	0.09	0.27	0.01
NODKGS65 (0-1)	11.8	0.46	0.42	1.34	0.93	5.93	4.53	8.08	4.76	1.02	7.44	-	208	156	32.1	12.5	7.00	12.2	6.81	1.47	0.06
NODKGS65 (1-2)	12.2	0.46	0.43	1.35	0.93	6.64	4.61	7.91	1.54	0.31	2.79	110	204	152	32.4	11.3	3.33	5.34	1.76	0.73	0.03
NODKGS65 (2-3)	11.3	0.45	0.44	1.37	0.95	7.17	4.61	7.93	3.51	0.52	4.20	112	206	149	33.5	11.0	3.28	7.74	2.06	0.62	0.05
NODKGS65 (3-4)	11.8	0.45	0.44	1.38	0.95	7.27	4.55	7.95	3.24	0.47	4.49	112	203	147	33.2	10.8	3.19	7.42	1.79	0.58	0.03
NODKGS65 (5-6)	11.6	0.45	0.44	1.38	0.93	7.76	4.48	7.92	3.31	0.53	1.95	111	204	141	33.2	10.3	2.71	7.13	1.79	0.40	0.02
NODKGS65 (6-7)	11.5	0.44	0.45	1.39	0.96	8.05	4.51	7.84	1.66	0.50	3.79	106	205	139	33.4	9.81	2.63	8.44	1.25	0.54	0.02
NODKGS65 (7-8)	11.5	0.44	0.45	1.39	0.95	8.36	4.53	7.96	0.54	0.56	4.14	110	207	139	33.3	9.98	2.74	10.5	1.72	0.44	0.03
NODKGS65 (8-9)	11.6	0.43	0.45	1.43	0.96	8.25	4.56	7.95	3.06	0.83	-	113	207	137	33.0	9.91	2.71	13.3	1.28	0.56	0.02
NODKGS65 (9-10)	11.8	0.44	0.45	1.40	0.95	8.41	4.35	7.84	0.37	0.44	1.84	109	200	135	32.4	9.69	2.66	6.77	1.05	<DL ^d	0.03
NODKGS65 (10-11)	12.1	0.44	0.45	1.42	0.97	8.40	4.47	7.80	3.16	0.55	-	108	202	135	32.4	9.73	2.66	6.48	1.21	0.47	0.02
NODKGS65 (11-12)	11.6	0.44	0.44	1.42	0.96	8.72	4.36	7.84	1.00	0.54	-	111	200	133	32.0	9.40	2.23	8.71	1.33	<DL	0.03
NODKGS65 (12-13)	11.9	0.43	0.45	1.42	0.97	8.60	4.41	7.82	2.79	0.39	-	111	199	131	31.8	9.34	2.49	12.4	1.10	0.44	0.03
NODKGS65 (13-14)	11.8	0.43	0.45	1.41	0.96	8.67	4.40	7.87	1.65	0.57	2.55	111	198	131	32.1	9.15	2.27	19.9	2.04	0.44	0.02
NODKGS65 (14-15)	11.7	0.44	0.45	1.43	0.96	8.99	4.39	7.89	2.90	0.52	12.2	119	199	132	32.1	9.22	2.32	11.7	1.29	0.28	0.04
NODKGS65 (15-16)	11.9	0.43	0.44	1.41	0.95	10.3	4.43	8.04	2.36	0.30	2.46	118	202	134	33.8	9.19	2.53	16.0	1.69	0.71	0.03
NODKGS65 (16-17)	10.9	0.44	0.45	1.40	0.94	9.21	4.40	7.81	7.28	0.61	4.61	145	197	131	31.9	8.92	2.47	6.10	0.91	0.41	0.02
NODKGS65 (17-18)	11.4	0.45	0.44	1.40	0.96	8.87	4.39	7.71	10.9	0.59	3.02	136	198	132	31.7	8.85	2.62	8.24	1.12	0.31	0.02
NODKGS65 (18-19)	12.1	0.44	0.45	1.43	0.95	9.68	4.25	7.91	2.55	0.83	<DL	106	196	133	32.0	8.95	2.61	6.33	1.72	0.45	0.03
NODKGS65 (19-20)	12.0	0.43	0.45	1.43	0.96	9.59	4.35	7.99	25.6	0.58	1.92	115	198	131	31.6	8.77	2.62	15.5	1.14	0.35	0.03
NODKGS65 (20-22)	12.3	0.44	0.45	1.42	0.96	9.84	4.30	7.88	5.54	0.43	-	109	196	130	31.1	8.42	2.54	10.7	0.85	0.32	0.03
NODKGS65 (22-24)	12.1	0.44	0.45	1.42	0.95	10.6	4.25	7.93	5.41	1.00	2.16	121	197	131	31.5	8.15	1.90	17.9	1.45	0.73	0.04
NODKGS65 (24-26)	11.9	0.43	0.44	1.41	0.96	10.5	4.43	8.03	3.26	0.45	-	123	202	132	31.1	8.25	2.51	31.2	1.19	<DL	0.03
NODKGS65 (26-28)	12.6	0.43	0.45	1.43	0.96	10.0	4.40	7.98	3.22	0.53	-	109	199	131	30.1	8.03	2.58	10.4	1.01	0.30	0.04
NODKGS65 (28-30)	12.2	0.44	0.44	1.38	0.94	9.99	4.40	8.01	4.71	0.46	-	125	199	133	29.7	8.02	2.54	11.4	1.25	<DL	0.03
NODKGS65 (30-32)	12.4	0.45	0.43	1.43	0.93	12.2	4.39	8.10	1.08	0.58	8.51	143	199	134	30.7	8.04	2.51	8.39	0.89	0.38	0.01
NODKGS65 (32-34)	12.6	0.44	0.45	1.42	0.97	10.1	4.42	7.84	1.93	0.47	-	110	197	132	29.0	7.53	2.68	14.0	1.04	<DL	0.03
NODKGS65 (34-36)	12.3	0.45	0.45	1.41	0.95	11.0	4.42	7.84	5.16	0.43	-	109	199	134	29.7	7.63	2.80	9.93	1.26	<DL	0.04
NODKGS65 (36-38)	12.0	0.44	0.45	1.38	0.95	11.0	4.42	7.88	4.21	0.54	-	126	196	137	31.0	7.53	2.88	13.4	1.58	<DL	0.03
NODKGS65 (38-40)	12.4	0.46	0.44	1.37	0.93	12.4	4.42	7.75	1.48	0.51	-	109	201	142	30.6	7.73	3.05	8.80	1.27	<DL	0.02
SW-XR-2 (average)	10.3	0.38	0.40	1.25	0.86	3.83	3.86	7.46	284	187	77.0	136	174	112	60.1	19.8	97.6	19.4	114	151	57.2
SW-XR-2 (reference)	10.4	0.38	0.40	1.26	0.86	3.85	3.89	7.46	285	188	77.3	136	175	112	60.0	19.8	97.8	19.4	114	151	57.3
NASS-5 (average)	9.47	0.35	0.35	1.10	0.76	-	3.55	6.58	<DL	-	<DL	20.5	161	100	5.42	9.19	1.23	<DL	0.34	<DL	<DL
NASS-5 (reference)	-	-	0.37	1.18	0.81	0.07	3.67	6.95	1.40	2.54	1.23	17.3	169	106	4.95	9.53	1.28	0.70	0.37	0.32	0.09
IAPSO (average)	12.4	0.45	0.45	1.42	0.98	1.70	4.75	8.50	1.97	0.29	47.8	54.1	208	129	98.2	12.1	1.55	108	2.65	5.97	0.13
IAPSO (reference)	10.2	0.39	0.41	1.27	0.90	-	-	7.40	-	-	-	-	182	-	-	11.0	-	-	-	-	-

^a numbers in parentheses = depth in core in cm

^b $Ce/Ce^* = 2Ce_{SN} / (La_{SN} + Nd_{SN})$

^c long-term averages obtained over multiple sessions of pore waters analyses. For each session the detection limits were obtained after measuring repeated blank solutions intercalated with pore water samples (1 blank for 5 samples).

^d below detection limits

Table 7

Fe-Cu-Zn-isotope composition (MC-ICP-MS) of the studied Mn-micronodules and Mn-nodules.

Sample ID	Description	Mn-nodule facies	$\delta^{56/54}\text{Fe}_{\text{IRMM-14}}$ (‰)	2sd	$\delta^{57/54}\text{Fe}_{\text{IRMM-14}}$	2sd	$\delta^{57/56}\text{Fe}_{\text{IRMM-14}}$	$\delta^{65/63}\text{Cu}_{\text{SRM976}}$	2sd	$\delta^{66/64}\text{Zn}_{\text{JMC}}$	2sd	$\delta^{66/64}\text{Zn}_{\text{SRM3168a}}$	2sd	$\delta^{68/66}\text{Zn}_{\text{SRM3168a}}$	2sd
NODKGS44	Mn-nodule	0	-0.63	0.04	-0.92	0.09	-0.29	0.21	0.03	0.76	0.06	1.66	0.06	1.65	0.11
NODKGS49 0-5cm	Mn-micronodules	0	-0.40	0.04	-0.60	0.09	-0.19	0.31	0.03	0.84	0.06	1.74	0.06	1.72	0.11
NODKGS49 5-10cm	Mn-micronodules	0	-0.34	0.04	-0.49	0.09	-0.15	0.30	0.03	0.61	0.06	1.51	0.06	1.49	0.11
NODKGS51	Mn-nodule	0	-0.53	0.04	-0.77	0.09	-0.23	0.26	0.03	0.75	0.06	1.65	0.06	1.59	0.11
NODKGS51 0-5cm	Mn-micronodules	0	-0.39	0.04	-0.54	0.09	-0.15	0.24	0.03	0.77	0.06	1.67	0.06	1.65	0.11
NODKGS51 5-10cm	Mn-micronodules	0	-0.32	0.04	-0.42	0.09	-0.10	0.28	0.03	0.73	0.06	1.63	0.06	1.54	0.11
NODKGS53	Mn-nodule	B	-0.48	0.04	-0.71	0.09	-0.22	0.35	0.03	0.85	0.06	1.75	0.06	1.70	0.11
NODKGS53 0-7 cm	Mn-micronodules	B	-0.43	0.04	-0.65	0.09	-0.22	0.24	0.03	0.83	0.06	1.73	0.06	1.72	0.11
NODKGS54	Mn-nodule	B	-0.39	0.04	-0.62	0.09	-0.23	0.30	0.03	0.86	0.06	1.76	0.06	1.75	0.11
NODKGS54 0-5cm	Mn-micronodules	B	-0.33	0.04	-0.48	0.09	-0.15	0.30	0.03	0.84	0.06	1.74	0.06	1.67	0.11
NODKGS54 5-10cm	Mn-micronodules	B	-0.34	0.04	-0.49	0.09	-0.16	0.34	0.03	0.82	0.06	1.72	0.06	1.68	0.11
NODKGS55	Mn-nodule	B	-0.46	0.04	-0.67	0.09	-0.21	0.33	0.03	0.87	0.06	1.77	0.06	1.71	0.11
NODKGS55 0-5cm	Mn-micronodules	B	-0.39	0.04	-0.55	0.09	-0.16	0.29	0.03	0.90	0.06	1.80	0.06	1.72	0.11
NODKGS55 5-10cm	Mn-micronodules	B	-0.40	0.04	-0.59	0.09	-0.19	0.32	0.03	0.88	0.06	1.78	0.06	1.69	0.11
NODKGS56	Mn-nodule	B	-0.44	0.04	-0.70	0.09	-0.26	0.32	0.03	0.86	0.06	1.76	0.06	1.72	0.11
NODKGS56 0-5cm	Mn-micronodules	B	-0.40	0.04	-0.55	0.09	-0.15	0.31	0.03	0.75	0.06	1.65	0.06	1.65	0.11
NODKGS56 5-10cm	Mn-micronodules	B	-0.37	0.04	-0.53	0.09	-0.17	0.35	0.03	0.88	0.06	1.78	0.06	1.72	0.11
NODKGS57	Mn-nodule	B	-0.55	0.04	-0.75	0.09	-0.21	0.33	0.03	0.84	0.06	1.74	0.06	1.69	0.11
NODKGS57 0-5cm	Mn-micronodules	B	-0.37	0.04	-0.50	0.09	-0.13	0.27	0.03	0.86	0.06	1.76	0.06	1.72	0.04
NODKGS57 5-10cm	Mn-micronodules	B	-0.36	0.04	-0.52	0.09	-0.16	0.28	0.03	0.84	0.06	1.74	0.06	1.72	0.04
NODKGS58	Mn-nodule	B	-0.48	0.04	-0.67	0.09	-0.19	0.32	0.03	0.86	0.06	1.76	0.06	1.71	0.11
NODKGS58 0-5cm	Mn-micronodules	B	-0.43	0.04	-0.59	0.09	-0.16	0.20	0.03	0.73	0.06	1.63	0.06	1.99	0.11
NODKGS58 5-10cm	Mn-micronodules	B	-0.39	0.04	-0.58	0.09	-0.19	0.35	0.03	0.81	0.06	1.71	0.06	1.47	0.11
NODKGS60	Mn-nodule	C	-0.59	0.04	-0.89	0.09	-0.30	0.29	0.03	0.80	0.06	1.70	0.06	1.67	0.11
NODKGS60 0-5cm	Mn-micronodules	C	-0.31	0.04	-0.43	0.09	-0.13	0.26	0.03	0.84	0.06	1.74	0.06	1.67	0.11
NODKGS60 5-10cm	Mn-micronodules	C	-0.27	0.04	-0.37	0.09	-0.10	0.23	0.03	0.77	0.06	1.67	0.06	1.66	0.11
NODKGS63	Mn-nodule	C	-0.41	0.06	-0.50	0.09	-0.09	0.33	0.03	0.84	0.06	1.74	0.06	1.68	0.11
NODKGS63 0-5cm	Mn-micronodules	C	-0.35	0.04	-0.52	0.09	-0.17	0.25	0.03	0.85	0.06	1.75	0.06	1.68	0.11
NODKGS65 0-5cm	Mn-micronodules	C	-0.33	0.04	-0.42	0.09	-0.09	0.21	0.03	0.79	0.06	1.69	0.06	1.65	0.11
NODKGS65 5-10cm	Mn-micronodules	C	-0.35	0.06	-0.51	0.09	-0.17	0.26	0.03	0.85	0.06	1.75	0.06	1.68	0.11
Nod-P-1, split 9-3	Mn-nodule, standard		-0.55	0.04	-0.78	0.09	-0.23	0.30	0.03	0.82	0.06	1.72	0.06	1.69	0.04
Nod-P-1, split 9-3	Mn-nodule, standard		-0.59	0.04	-0.83	0.09	-0.24	0.38	0.03	0.81	0.06	1.71	0.06	1.71	0.11
Nod-P-1, split 9-3	Mn-nodule, standard		-0.59	0.04	-0.83	0.09	-0.24	0.37	0.03	0.83	0.06	1.73	0.06	1.67	0.11
Nod-P-1, split #4-25	Mn-nodule, standard		-0.57	0.06	-0.86	0.09	-0.30	0.31	0.03	0.80	0.06	1.70	0.06	1.67	0.11
Nod-P-1, split #4-25	Mn-nodule, standard		-0.61	0.04	-0.88	0.09	-0.28	0.31	0.03	0.83	0.06	1.73	0.06	1.68	0.11

Table 8

Average chemical composition of Mn-micronodules and Mn-nodules of the ocean.

Location Reference	Mn-micronodules	Mn-nodules	Mn-nodule standard	Nod-P-1	Mn-nodule standard	Nod-A-1	Mn-micronodules	Mn-micronodules	Mn-micronodules	Mn-micronodules
	CCZ this study	CCZ this study	CCZ this study		Atlantic Ocean this study		CCZ Dubinin and Sval'nov, 2003	CCZ Dubinin et al., 2008	Central Pacific Basin Ito et al., 2005	Equatorial North Pacific Dubinin and Sval'nov, 2000a
Mn (wt.%)	38.2	28.2	28.2		29.6		18.3	24.1	29.9	28.3
Fe	2.69	5.33	5.33		5.89		11.2	3.17	4.35	2.62
Si	14.7	-	-		5.85		1.74	-	-	-
Al	2.04	2.24	2.24		2.46		2.08	1.72	1.56	3.74
Ca	1.55	1.64	1.64		2.24		11.4	-	-	1.65
Mg	2.09	1.73	1.73		2.03		2.83	-	-	2.90
Na	1.17	2.53	2.53		1.71		0.87	-	-	0.63
K	1.09	0.93	0.93		1		0.49	-	-	3.48
Ti	0.24	0.27	0.27		0.27		0.3	0.47	0.47	0.21
P	0.07	0.19	0.19		0.21		0.59	0.10	0.09	0.07
S	0.06	0.11	0.11		0.1		0.34	-	-	-
Li (mg/kg)	101	159	159		140		76.1	-	-	48.7
Be	1.07	2.02	2.02		2.3		5.6	-	-	2.20
B	80	95.8	95.8		95		120	-	-	-
Sc	7.79	10.9	10.9		9.7		12.4	-	-	5.31
V	416	488	488		510		660	-	-	104
Cr	15.1	11.4	11.4		13.3		20.9	-	-	34.7
Co	1747	2288	2288		2290		3180	1625	2871	1620
Ni	14148	12553	12553		13500		6450	13163	19212	38800
Cu	18122	13680	13680		11200		1130	14963	8191	9250
Zn	2738	1864	1864		2020		800	-	-	1410
Se	-	3.9	3.9		-		-	-	-	-
As	55.9	74.2	74.2		88.5		310	-	-	41.1
Rb	28.8	22.1	22.1		23.7		10.6	-	-	27.3
Sr	532	566	566		670		1630	-	-	270
Y	32.1	83.4	83.4		90		120	-	-	37.1
Zr	90	268	268		280		310	-	-	63.7
Nb	12.5	19.3	19.3		21.3		43.1	-	-	7.02
Mo	816	740	740		675		390	528	826	125
Cd	11.7	17.9	17.9		22.6		7.5	-	-	4.08
Sn	0.96	0.32	0.32		1.9		3	-	-	0.41
Sb	52.7	45	45		49.4		33.8	-	-	5.56
Te	1.33	2.94	2.94		4.8		30.9	-	-	1.91
Ba	1664	2076	2076		2690		1530	-	-	408
Hf	1.43	3.83	3.83		4.2		5.8	-	-	1.80
Ta	0.25	0.3	0.3		0.33		0.76	-	-	0.49
W	64.2	56	56		57.8		87	68.3	106	12.4
Tl	71.1	188	188		210		120	-	-	46.1
Pb	429	416	416		475		860	-	-	79.3
Bi	5.31	5.24	5.24		5.8		10.2	-	-	3.36
Th	10.67	19.4	19.4		16.7		25.1	11.5	5.61	4.25
U	2.46	3.83	3.83		4		7	-	-	2.04
Au	<0.030	-	-		<0.009		<0.009	-	-	-
Pt	0.06	0.1	0.1		0.12		0.52	-	-	-
La	41.2	99	99		105		115	39.1	38.0	27.7
Ce	196	262	262		305		720	197	517	194
Pr	14.2	30.6	30.6		31		25	13.8	8.55	7.69
Nd	60.8	124	124		130		98	58.5	35.0	28.4
Sm	16	30.7	30.7		31		21.9	15.0	7.93	6.55
Eu	3.89	7.44	7.44		7.6		5.2	3.50	2.04	2.41
Gd	14	29.6	29.6		30.4		25.4	13.5	8.34	7.55
Tb	2.2	4.79	4.79		4.9		4	1.97	1.47	1.24
Dy	11.5	26.6	26.6		27.1		23.8	10.7	8.88	6.60
Ho	2.03	4.77	4.77		5		5	1.88	1.85	1.38
Er	5.21	12.8	12.8		13.6		14.4	4.88	5.47	4.23
Tm	0.73	1.79	1.79		1.9		2	0.71	0.84	0.67
Yb	5.15	12.6	12.6		12.9		13.9	4.61	5.70	3.40
Lu	0.7	1.78	1.78		1.8		2.1	0.67	0.91	0.65

Table 8 (continued).

	Mn-micronodules	Mn-micronodules	Mn-micronodules	Mn-micronodules	Mn-micronodules	Mn-micronodules	Mn-micronodules	Mn-micronodules	Mn-micronodules
Location	Equatorial North Pacific	Equatorial South Pacific	Guatemala Basin	Peru Basin	Peru Basin	East Pacific Rise	East Pacific Rise	Southwest Pacific Basin	Southwest Pacific Basin
Reference	Stoffers et al., 1984	Stoffers et al., 1984	Dubinina and Sval'nov, 1995	Dubinina and Sval'nov, 2000a	Stoffers et al., 1984	Stoffers et al., 1984	Dekov et al. 2003	Dubinina and Sval'nov, 2000b	Dubinina and Sval'nov, 2000b
Mn (wt.%)	23.9	27.1	30.9	33.9	26.7	8.57	7.61	16.4	16.4
Fe	5.10	9.60	1.84	2.79	6.09	16.5	13.0	14.8	14.8
Si	-	-	-	-	-	-	0.46	-	-
Al	-	-	0.51	0.80	-	-	0.38	3.07	3.07
Ca	-	-	-	-	-	-	2.67	3.05	3.05
Mg	-	-	-	-	-	-	0.62	-	-
Na	-	-	-	-	-	-	0.45	-	-
K	-	-	-	-	-	-	0.12	-	-
Ti	-	-	-	-	-	-	0.15	0.52	0.52
P	-	-	0.06	0.12	-	-	0.84	0.77	0.77
S	-	-	-	-	-	-	-	-	-
Li (mg/kg)	-	-	-	-	-	-	7.61	-	-
Be	-	-	-	-	-	-	1.14	-	-
B	-	-	-	-	-	-	110	-	-
Sc	-	-	-	-	-	-	2.97	-	-
V	-	-	-	-	-	-	453	-	-
Cr	-	-	-	-	-	-	13.0	-	-
Co	1700	800	265	160	800	200	212	3371	3371
Ni	7300	6350	4286	13800	7800	800	706	4843	4843
Cu	9900	6800	2871	10300	6900	900	799	1529	1529
Zn	1500	1500	-	-	2000	900	387	-	-
Se	-	-	-	-	-	-	0.90	-	-
As	-	-	-	-	-	-	-	-	-
Rb	-	-	-	-	-	-	1.65	-	-
Sr	-	-	-	-	-	-	1172	-	-
Y	-	-	-	-	-	-	69.7	-	-
Zr	-	-	-	-	-	-	66.1	-	-
Nb	-	-	-	-	-	-	2.72	-	-
Mo	-	-	-	-	-	-	73.2	439	439
Cd	-	-	-	-	-	-	5.78	-	-
Sn	-	-	-	-	-	-	7.31	-	-
Sb	-	-	-	-	-	-	3.93	-	-
Te	-	-	-	-	-	-	1.44	-	-
Ba	4800	1950	-	-	4433	900	846	-	-
Hf	-	-	-	-	-	-	0.85	-	-
Ta	-	-	-	-	-	-	0.04	-	-
W	-	-	-	-	-	-	6.16	45.5	45.5
Tl	-	-	-	-	-	-	20.2	-	-
Pb	-	-	-	-	267	100	99.8	-	-
Bi	-	-	-	-	-	-	0.46	-	-
Th	-	-	-	-	-	-	0.78	9.01	9.01
U	-	-	-	-	-	-	5.05	-	-
Au	-	-	-	-	-	-	-	-	-
Pt	-	-	-	-	-	-	-	-	-
La	-	-	22.2	28.8	-	-	69.8	115	115
Ce	-	-	50.8	102	-	-	38.4	478	478
Pr	-	-	5.38	7.05	-	-	11.0	29.1	29.1
Nd	-	-	22.9	33.3	-	-	46.6	124	124
Sm	-	-	5.00	7.57	-	-	9.28	28.1	28.1
Eu	-	-	1.18	1.78	-	-	2.63	6.69	6.69
Gd	-	-	5.08	8.13	-	-	11.9	30.2	30.2
Tb	-	-	0.82	1.20	-	-	1.78	4.40	4.40
Dy	-	-	5.02	7.81	-	-	11.4	27.5	27.5
Ho	-	-	1.12	1.60	-	-	2.47	5.82	5.82
Er	-	-	3.39	4.35	-	-	7.21	16.5	16.5
Tm	-	-	0.49	0.66	-	-	1.05	2.15	2.15
Yb	-	-	3.22	4.13	-	-	6.59	14.1	14.1
Lu	-	-	0.51	0.64	-	-	1.08	2.12	2.12

Table 8 (continued).

	Mn-micronodules	Mn-micronodules	Mn-micronodules	Mn-micronodules	Mn-micronodules	Mn-nodules	Mn-nodules
Location	Southwest Pacific Basin	western North Pacific Ocean	Angola Basin	Mid-Atlantic Ridge	Central Indian Basin	CCZ	Peru Basin
Reference	Stoffers et al., 1984	Yasukawa et al., 2020	Dubinina et al., 2013	Dekov et al. 2003	Pattan et al., 1994	Hein and Koschinsky, 2014	Hein and Koschinsky, 2014
Mn (wt.%)	17.9	20.3	18.6	8.82	26.7	28.1	34.2
Fe	9.92	4.67	8.15	25.9	4.00	5.92	6.12
Si	-	-	-	0.59	-	-	4.82
Al	-	3.74	2.87	0.84	2.96	2.31	1.5
Ca	-	2.06	-	1.80	1.74	1.72	1.82
Mg	-	1.93	-	1.16	1.95	1.88	1.71
Na	-	1.08	-	0.83	0.91	1.98	2.65
K	-	1.32	-	0.33	0.98	1.01	0.81
Ti	-	0.33	-	0.07	0.38	0.28	0.16
P	-	0.42	0.28	-	0.17	0.22	0.15
S	-	-	-	-	-	-	-
Li (mg/kg)	-	-	62.7	12.8	-	129	311
Be	-	-	2.13	1.30	-	-	1.4
B	-	-	-	57.3	-	-	-
Sc	-	16.7	-	3.20	-	11	7.58
V	-	233	288	183	126	429	431
Cr	-	26.1	-	33.3	-	-	16
Co	1667	1697	2327	420	927	2011	475
Ni	6767	14653	7393	549	8525	13159	13008
Cu	3133	3884	2376	3963	7275	10631	5988
Zn	1067	1058	1126	1224	1049	1385	1845
Se	-	-	-	-	-	-	0.5
As	-	48.6	85.7	-	-	-	65
Rb	-	36.4	31.3	4.33	-	23.6	12.2
Sr	-	374	514	561	455	633	687
Y	-	168	75.8	29.5	71.0	92	69
Zr	-	109	-	44.8	-	286	325
Nb	-	10.4	-	1.00	-	18.9	13.2
Mo	-	338	223	76.7	249	587	547
Cd	-	-	18.7	2.18	-	-	18.8
Sn	-	-	-	0.45	-	-	0.9
Sb	-	-	-	3.38	-	-	61
Te	-	-	-	-	-	3.5	1.7
Ba	1533	710	974	1507	1637	3752	3158
Hf	-	1.54	-	0.78	-	4.28	4.74
Ta	-	0.29	-	0.03	-	0.31	0.23
W	-	-	34.6	1.98	-	61	75
Tl	-	-	39.1	22.8	-	-	129
Pb	500	176	595	173	469	311	121
Bi	-	-	9.27	0.45	-	-	3.25
Th	-	5.36	36.1	10.9	-	14	6.9
U	-	2.52	4.18	10.2	-	3.96	4.39
Au	-	-	-	-	-	-	-
Pt	-	-	-	-	-	-	0.04
La	-	95.9	77.3	49.3	72.7	108	68
Ce	-	212	826	204	384	255	110
Pr	-	25.5	20.4	13.7	-	32	14.1
Nd	-	116	75.9	53.9	86.8	135	63
Sm	-	26.1	17.7	11.9	27.5	32.7	14
Eu	-	6.40	4.11	3.18	6.93	7.83	3.87
Gd	-	29.0	17.9	11.7	25.2	31	15.6
Tb	-	4.43	2.74	1.78	-	4.78	2.52
Dy	-	27.6	15.9	9.53	18.9	27.5	15.8
Ho	-	5.54	3.14	1.67	3.68	5.12	3.42
Er	-	16.0	8.37	4.44	10.6	14.1	9.8
Tm	-	2.24	1.16	0.62	-	2.02	1.49
Yb	-	14.1	7.17	3.73	10.3	13.1	10.3
Lu	-	2.10	1.20	0.58	3.65	1.95	1.61

Table 8 (continued).

Mn-nodules	
Location	Indian Ocean
Reference	Hein and Koschinsky, 2014
Mn (wt.%)	24.4
Fe	7.10
Si	9.2
Al	2.8
Ca	1.63
Mg	1.9
Na	1.8
K	1.1
Ti	0.4
P	0.17
S	-
Li (mg/kg)	97
Be	-
B	-
Sc	-
V	-
Cr	-
Co	1100
Ni	11000
Cu	10400
Zn	1200
Se	-
As	-
Rb	-
Sr	679
Y	102
Zr	-
Nb	-
Mo	570
Cd	-
Sn	-
Sb	-
Te	-
Ba	1570
Hf	-
Ta	-
W	-
Tl	-
Pb	712
Bi	-
Th	-
U	-
Au	0.003
Pt	0.075
La	128
Ce	452
Pr	33
Nd	144
Sm	32.1
Eu	7.78
Gd	31
Tb	5
Dy	26.2
Ho	4.87
Er	12.4
Tm	2
Yb	11.6
Lu	1.92